A new variable-temperature scanning tunneling microscope and temperature-dependent spin-polarized scanning tunneling spectroscopy on the Cr(001) surface

Dissertation
zur Erlangung des Doktorgrades
des Fachbereichs Physik
der Universität Hamburg

vorgelegt von
Torben Hänke
aus Hamburg

Hamburg
2005

Gutachter der Dissertation:
Prof. Dr. R. Wiesendanger
Prof. Dr. R. L. Johnson

Gutachter der Disputation:
Prof. Dr. R. Wiesendanger

Datum der Disputation:
05.09.2005

Vorsitzender des Prüfungsausschusses:
Priv.-Doz. Dr. D. Grundler

Vorsitzender des Promotionsausschusses:
Prof. Dr. G. Huber

Dekan des Fachbereichs Physik:
Prof. Dr. G. Huber

Abstract

Scanning tunneling microscopy (STM) is a powerful tool to study the interplay between structural, electronic, and magnetic properties with high spatial and energy resolution. In this thesis the Cr(001) surface was investigated with regard to its temperature-dependent magnetic structure.

A new STM was designed that provides the ability to operate with high stability at a temperature between 20-300 K. The entire microscope, including both tip and sample, is cooled to provide high spectroscopic resolution at low temperatures. Furthermore, the STM is equipped with an *in situ* tip exchange mechanism to introduce magnetically coated tips into the STM.

With the new designed STM the spin-density wave (SDW) of Cr(001) has been investigated at temperatures between 20-300 K by means of spin-polarized scanning tunneling microscopy (SP-STM). Although neutron scattering data measured on the same crystal clearly show a spin-flip transition from a transverse (T)-SDW to a longitudinal (L)-SDW at the expected spin-flip temperature $T_{\mathrm{SF}} = 123\,\mathrm{K}$, no change was found on the Cr(001) surface with SP-STM. Throughout the entire temperature range the Cr(001) surface maintains a topological antiferromagnetic order with an in-plane magnetization that reverses between adjacent atomically flat terraces separated by monatomic step edges. The experimental results are interpreted by a suppression of a spin-flip transition in the near-surface region probably driven by the surface anisotropy. The continuous connection of the surface T-SDW to the bulk L-SDW is accomplished by the formation of a 90° domain wall just below the surface. In the last part of the thesis the temperature-dependent surface electronic structure of Cr(001) is investigated by means of scanning tunneling spectroscopy (STS) in the temperature range between 22 K and 350 K. Consistent with earlier observations a sharp peak is found in the tunneling spectra close to the Fermi level E_{F}. While the binding energy remains unchanged the peak broadens with increasing temperature. The experimental data are fitted within the framework of two physical models, i.e., in terms of a single-particle band theory and an orbital Kondo effect. Both models lead to a reasonable agreement between the fit and the experimental data at low temperatures. Using the Kondo model a Kondo temperature T_{K} of 123 K is obtained. If interpreted in terms of a single-particle band theory the fit results in an electron-phonon mass-enhancement factor λ which is 5-10 times larger than the Cr bulk value.

Inhaltsangabe

Rastertunnelmikroskopie (RTM) ist eine hervorragende Methode, das Wechselspiel zwischen strukturellen, elektronischen und magnetischen Eigenschaften mit einer hohen lateralen Empfindlichkeit bei gleichzeitig hoher Energieauflösung zu untersuchen. In dieser Arbeit wird die Cr(001)-Oberfläche in Hinblick auf ihre temperaturabhängige magnetische Struktur untersucht.

Hierfür wurde ein RTM für variable Temperaturen im Bereich von 20-300 K aufgebaut. Das Design des Instruments sieht die Kühlung sowohl der Spitze als auch der Probe vor, um bei tiefen Temperaturen von einer hohen Energieauflösung zu profitieren. Desweiteren ist das RTM mit einem *in situ* Spitzenwechselmechanismus ausgestattet, um magnetisch beschichtete Spitzen in das Mikroskop zu transferieren.

Mit diesem neuen Mikroskop wurde die Spindichtewelle (SDW) an der Cr(001)-Oberfäche bei Temperaturen von 20-300 K mittels spinpolarisierter Rastertunnelmikroskopie (SP-RTM) untersucht. Obwohl Neutronenstreuexperimente einen "spin-flip"-Phasenübergang von einer transversalen (T)-SDW hin zu einer longitudinalen (L)-SDW bei der erwarteten "spin-flip"-Temperatur von $T_{\mathrm{SF}} = 123$ K im Volumen zeigen, wurde keine Veränderung an der Cr(001)-Oberfläche mittels SP-RTM gefunden. Im gesamten Temperaturbereich behält die Cr(001)-Oberfläche die magnetische Struktur des topologischen Antiferromagnetismus. Die unterdrückung des "spin-flip"-Übergangs in der Oberflächenregion wird durch die Oberflächenanisotropie hervorgerufen, wobei der kontinuierliche Übergang von der T-SDW an der Oberfläche zur L-SDW im Volumen mittels Ausbildung einer 90°-Domänenwand unterhalb der Oberfläche erreicht wird. Im letzten Teil der Arbeit wird die temperaturabhängige elektronische Struktur der Cr(001)-Oberfläche mittels Rastertunnelspektroskopie (RTS) untersucht. In Übereinstimmung mit publizierten Ergebnissen beobachte ich eine scharfe Resonanz im Spektrum der differentiellen Leitfähigkeit nahe dem Ferminiveau E_{F}. Während die Bindungsenergie dieses Zustandes nahezu unverändert bleibt, verbreitert sich die Resonanz mit zunehmender Temperatur. Die experimentellen Daten werden im Rahmen zweier theoretischer Modelle, nämlich der Einteilchen-Bandstruktur-Theorie und des orbitalen Kondo-Modells diskutiert. Beide Modelle führen zu einer guten Übereinstimmung mit den experimentellen Daten bei tiefen Temperaturen. Unter Verwendung der Kondo-Modells läßt sich eine Kondotemperatur T_{K} von 123 K ermitteln. Im Rahmen der Einteilchen-Bandstruktur-Theorie ergibt sich ein "electron-phonon mass-enhancement Faktor" λ, der um 5-10 Mal höher ist als der Wert, der experimentell für das Cr-Volumen ermittelt wurde.

Contents

Chapter 1

Introduction

Since the discovery of magnetite and the invention of the compass needle around 200 AD in China the magnetic interaction is a permanent companion in everyday life, although the physical basis of ferromagnetism could only be explained by the quantum-theory 2000 years later. Nowadays many applications exist, starting with magnetic pin boards to magnetic storage devices. While only a short time ago it was the field of research for small specialized groups, today ferromagnetism is investigated by many research groups and is the basis of applications even in biophysics[1, 2].

Magnetism in reduced dimensions is a fascinating topic with a lot of barely understood phenomena [3, 4]. For the understanding of magnetic properties in general it is indispensable to study the basic properties in nanometer scale systems, where changes in structure or size have large effects on the magnetic properties. The advances in ultra-high vacuum (UHV) technology and molecular beam epitaxy (MBE) techniques during the past decades made it possible to study magnetism under the condition of reduced dimensionality, such as in ultrathin films, clusters, in nanowires or even single atoms on surfaces. Magnetic materials of two, one or zero dimensionality exhibit a large number of surprising properties. These are of interest for fundamental research. Although considerable experimental and theoretical progress has been achieved in the last few years the subject matter is still in the area of basic research. In recent years the driving force in this field, however, came from applied physics and technology. The demand for ever higher data storage and processing capacity intensified the worldwide request for nanotechniques that promise to be able to tailor magnetic materials exhibiting well defined properties. The discovery of the giant magnetoresistance effect (GMR) in Fe-Cr-Fe layers [5, 6] a decade ago has initiated a vast amount of research activities, and it also has an enormous impact on the technology related to magnetic data storage. It is a unique situation that, despite the fact that many questions still have to be solved, the technological application already have reached the mass market, the perhaps most prominent example being IBM's hard disk read head which is based on the GMR effect.

Currently, the data storage industry reports an increase in areal data storage of 60% annually. While, for future systems, the spin information of a single atom is conceived the ultimate physical unit to magnetically store a bit of information, the next serious obstacle to be approached technologically soon is the superparamagnetic limit. The lower limit for the magnetic grain size (which is equivalent to a switching unit) has recently been estimated to 600 nm^2 in volume, or ∼10 nm lateral extent [7]. The study of laterally structured nanomagnetic systems of only one or zero dimensions was hampered in the past by a lack of adequate magnetic imaging techniques being able to provide a resolution comparable with size of entities that can be produced in a controlled way. At this point spin-polarized scanning tunneling microscopy (SP-STM) comes into play as a powerful tool to study magnetism down to the atomic scale. This method is magnetically sensitive and has a high spatial resolution which allows not only the investigation of magnetic properties but also the direct correlation to electronic structure measurements and topographic studies.

In this thesis the method of spin-polarized scanning tunneling microscopy was used to study the temperature-dependent electronic and magnetic properties of the Cr(001) surface. At room temperature Wiesendanger *et al.* [8] have proven that the surface magnetic structure of the Cr(001) surface is characterized by the model of the topological antiferromagnetism. Although several other magnetic imaging techniques exist to investigate surface magnetism like spin-polarized (SP) field emission, Lorentz microscopy, scanning electron microscopy with polarization analysis (SEMPA), X-ray magnetic circular dichroism (XMCD), and photoelectron emission microscopy (PEEM) and magnetic force microscopy (MFM) the method of SP-STM was up to the present the only technique allowing the study of antiferromagnetically ordered surfaces. Although the lateral resolution for example of SEMPA or PEEM offer high resolution on the order of 10 nm, the spatial averaging of all these techniques hinders the imaging of antiferromagnetically ordered surfaces.

The present work is organized as follows: Chapter 2 gives an introduction to the theory of scanning tunneling microscopy and -spectroscopy including a section dealing with spin-polarized tunneling. The following Chapter 3 describes a newly designed variable-temperature STM that has been developed and built up in the first phase of the thesis. In Chapter 4 the UHV system is introduced. This includes all the sample preparation techniques used in this thesis like Ar^+-ion etching and MBE deposition. The important topic of preparing magnetic sensitive tips is also discussed. Chapter 5 represents the central part of the thesis. Here the results of the temperature-dependent study of the Cr(001) surface are presented. This chapter has three parts: Chromium, the sample system investigated, is introduced in the first part. The next section describes the temperature-dependent magnetic structure of the Cr(001) surface and finally the temperature-dependent scanning tunneling spectroscopy obtained on the Cr(001) surface is discussed.

Chapter 2

Scanning tunneling microscopy

Within the twenty years since the invention of the scanning tunneling microscope (STM) [9] scanning tunneling microscopy has developed into a powerful tool to study the surfaces of conducting samples. The most obvious strength of this method is the correlation of structural, electronic and magnetic properties with high spatial and energy resolution.

This chapter describes the general physics involved to understand the phenomenon of the tunnel process. First the mode of operation of a STM and the experimental realization of data acquisition are presented in Sec. 2.1. A more detailed treatment of these topics can be found in the literature [10]. After an introduction to tunnel theory in one dimension (Sec. 2.2) a more detailed picture of the tunnel process using perturbation theory follows (Sec. 2.3). Finally scanning tunneling spectroscopy (STS) is presented in Sec. 2.4 followed by its expansion to the magnetic sensitive spin-polarized scanning tunneling microscopy (SP-STM).

2.1 STM — the general principles

To investigate sample properties by scanning tunneling microscopy a sharp metallic tip is used as a local probe. The top segment of the tip can be positioned with sub-Ångström accuracy in three dimensions via a piezoelectric actuator. The tip faces a conducting surface, the sample, held at a different bias voltage U_{bias} in the range of a few milli-volts up to some volts. If the distance between the top most atoms of the tip and the sample surface is reduced to a few Å, so that the quantum mechanical wave functions exhibit a certain overlap, electrons can traverse from the occupied states of one electrode to the unoccupied states of the other electrode and a small but measurable tunnel current I_{t} in the range pico-ampere to nano-ampere flows. This tunnel current has a strong dependence on the width

s of the vacuum barrier (cf. Sec. 2.3):

$$I_\mathrm{t} \propto \exp(-A\sqrt{\bar{\phi}}\; s). \tag{2.1}$$

Here is $A \approx 1\text{Å}^{-1}(\text{eV})^{-1/2}$ and $\bar{\phi}$ the average local barrier height between the two electrodes which depends on the work functions of the electrode materials. In case of a metallic surface $\bar{\phi}$ is on the order of some eV. From Eq. 2.1 two main characteristics of the STM can be deduced. An increase of the barrier width by 1 Å will lead to a decrease of the tunnel current by approximately one order of magnitude and hence the STM is highly sensitive to the variation of the distance between tip and sample. Furthermore, the tunnel current is laterally confined; in the ideal case the main current is carried by a single atom at the tip apex only. Fig. 2.1 shows a scheme of a typical setup of an STM where the tip is mounted to a piezoelectric actuator in form of a tube scanner.

The most popular mode of operation in scanning tunneling microscopy is the constant-current mode. To image a surface a given area is split into a lateral raster (x, y) and the tip is scanned line by line over the surface. Simultaneously the vertical z-displacement is regulated via the piezoelectric actuator by a feedback loop in the way that the tunnel current I_t is compared with a preset current. If deviations occur the feedback loop adjusts the vertical z-displacement to keep the

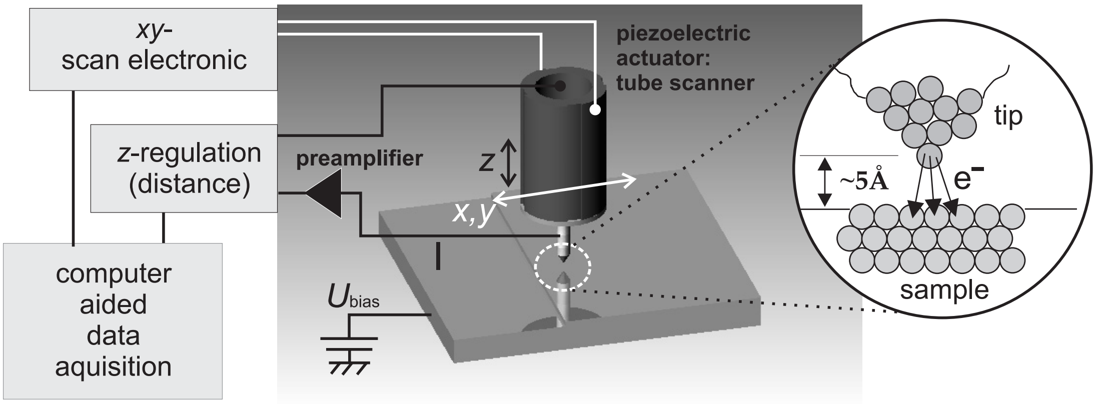

Figure 2.1: Sketch of the operating mode of the STM. A sharp metallic tip is mounted on top of a piezoelectric actuator. The topmost atoms of the tip have a distance of only a few Å from the sample. By applying a bias voltage U_bias between tip and sample a small and strongly distance dependent current flows. The tip is scanned via the piezoelectric actuator line by line above a certain area of the sample. Hereby, the tunnel current serves as feedback control parameter for the positioning of the tip and the tip follows the contour of the surface at a constant distance.

tunnel current I_t constant. The variations of the voltage which is applied to the piezoelectric actuator by the feedback loop are recorded for each point. Because of the well known characteristics of piezoelectric devices the voltage can be converted into distances changes leading to a three dimensional image $z(x, y)$ of the scanned area.

As a good approximation the trace $z(x, y)$ can be regarded as an image of the surface topography. This is especially correct if the measured area exhibits monatomic steps, high islands or other striking features. By this reason the constant-current mode is often referred to as topographic mode.

For lateral variations on the order of 1 Å contour lines in the STM image cannot easily be interpreted as height-profiles of the surface topography. Moreover $z(x, y)$ represents a contour of constant local density of states (LDOS) in the region of the Fermi level of the sample surface [11]. This context is discussed in the next chapter.

Furthermore, the STM opens up the possibility to investigate the electronic structure of a sample with high lateral resolution by performing full $\mathrm{d}I/\mathrm{d}U$ spectroscopy at different positions of the sample. Ideally this is done at every measurement point of an image area to obtain a three-dimensional parameter space of x, y-position and energy-dependent dI/dU signal. This allows a direct correlation of topographic $z(x, y)$ and spectroscopic properties $\mathrm{d}I/\mathrm{d}U(x, y, U)$ of the sample. If interest is focused only on one particular energy a very time-saving alternative to full $\mathrm{d}I/\mathrm{d}U$ spectroscopy is the acquisition of $\mathrm{d}I/\mathrm{d}U$ maps. While $\mathrm{d}I/\mathrm{d}U$ spectra are acquired with an open feedback loop at the given stabilization parameters, for the measurement of $\mathrm{d}I/\mathrm{d}U$ maps the feedback loop is not switched off at any time but simultaneously to the topographic measurement a lock-in technique derives the $\mathrm{d}I/\mathrm{d}U$ signal at the corresponding voltage. Due to the reduction of measurement parameters, i.e. no energy resolution, the spatial resolution can be enhanced to perform measurements in even shorter time without the loss of correlation between topography $z(x, y)$ and differential tunnel conductance $\mathrm{d}I/\mathrm{d}U(x, y)$.

2.2 The tunnel effect in one dimension

In classical mechanics a particle of energy E can overcome a potential barrier of V_0 only if $E > V_0$, otherwise it is reflected as sketched in Fig. 2.2(a). When considering microscopic length scales small objects like electrons have to be treated in terms of quantum mechanics. Then the probability of an electron to traverse a potential barrier is non-zero even if $E < V_0$. This is sketched in Fig. 2.2(b) for an electron of energy E and mass m, and a potential barrier of height V_0 and

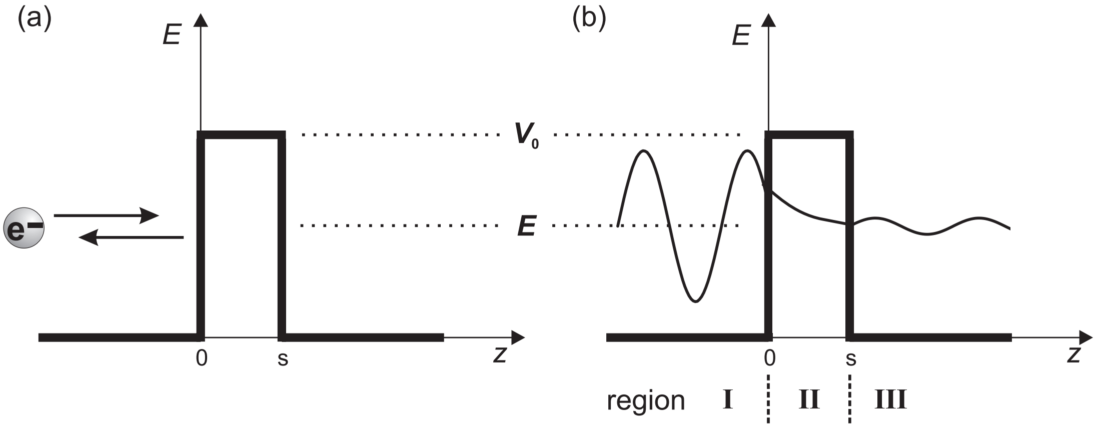

Figure 2.2: Tunnel effect in one dimension. (a) in classical mechanics an electron (e-) of energy E is reflected by a potential barrier V_0 if $E < V_0$; (b) in quantum physics the probability of the electron wave to traverse the potential barrier is non-zero.

width s. Three different regions can be distinguished:

region I:	$z < 0$,	$V(z) = 0$,	in front of the barrier,
region II:	$0 < z < s$,	$V(z) = V_0$,	inside the barrier,
region III:	$s < z$,	$V(z) = 0$,	behind the barrier.

In each region the electron can be described by the solution of the time-independent Schrödinger equation:

$$\left(-\frac{\hbar^2}{2m}\frac{\mathrm{d}^2}{\mathrm{d}z^2} + V(z)\right)\ \psi(z) \ = \ E\,\psi(z), \tag{2.2}$$

where ψ is the electron wave function and $\hbar$ is Planck's constant divided by 2π. The solution for the wave functions of a particle with the mass m and energy $E < V_0$ in the three different regions is given by:

$$\begin{aligned}\psi_1 &= e^{ikz} + Ae^{-ikz}\\ \psi_2 &= Be^{-\kappa z} + Ce^{\kappa z}\\ \psi_3 &= De^{ikz}\,,\end{aligned} \tag{2.3}$$

with $k^2 = 2mE/\hbar^2$ and $\kappa^2 = 2m(V_0 - E)/\hbar^2$. The wave function has oscillatory behavior outside the barrier corresponding to an incident, reflected and transmitted wave. Inside the barrier the wave function shows an exponential decay. To derive the overall wave function, the different wave functions $\psi(z)$ and their derivatives $\mathrm{d}\psi(z)/\mathrm{d}z$ are matched at the discontinuity points of the potential $z = 0$ and $z = s$ and enables to estimate the relation between the constants A, B, C and D. Now the transmission coefficient T is defined as the transmitted current density j_t related to the incident current density j_i [10]:

$$T = \frac{j_\mathrm{t}}{j_\mathrm{i}} = |D|^2 = \frac{1}{1 + (k^2+\kappa^2)^2/(4k^2\kappa^2)\sinh(\kappa s)}\,. \tag{2.4}$$

In the limit of a strongly attenuating barrier (decay constant $\kappa s >> 1$) the exact solution of Eq. 2.4 can be approximated by:

$$T \approx \frac{16k^2\kappa^2}{(k^2+\kappa^2)^2} \cdot e^{-2\kappa s}\,. \tag{2.5}$$

This approximation shows the exponential dependence of the transmission coefficient (and thus the tunnel current) on the barrier width s. Furthermore, the transmission T is proportional to the square root of the effective barrier height which is given by $\sqrt{\phi_\mathrm{eff}} = \sqrt{V_0 - E}$. The simple one dimensional model explains the phenomenon of electron tunneling well, and explains the high sensitivity of the STM to variations of the distance between tip and sample.

However, this simple model treating the electrons as non-interacting, free particles has two disadvantages. First of all the experimental observation of tunneling into surface states that are confined in the surface plane ($k_z = 0$) cannot be described. A second limitation is that there is no dependence of the tunnel current on the density of states of the surface ρ_s. In the next section a complementary approach based on time-dependent perturbation theory will be introduced giving a more realistic description of the tunnel process in STM.

2.3 Perturbation theory in STM

The first approach to describe the tunnel process within time-dependent perturbation therory was given by Bardeen [12] in 1961 for a planar metal-oxide-metal tunnel junction. Here both electrodes are described as weak interacting systems and the tunnel current can be calculated by using "*Fermi's Golden Rule*". Tersoff and Hamann found for the tunnel current the following relation [11, 13]:

$$I = \frac{2\pi e}{\hbar} \cdot \sum_{\mu,\nu} f(E_\mu)\left[1 - f(E_\nu + eU)\right] \cdot |M_{\mu\nu}|^2 \cdot \delta(E_\mu - E_\nu)\,. \tag{2.6}$$

Here $f(E)$ is the Fermi-Dirac distribution, U the applied bias voltage, $M_{\mu\nu}$ the matrix element of the transition between the state ψ_ν of the surface and ψ_μ of the

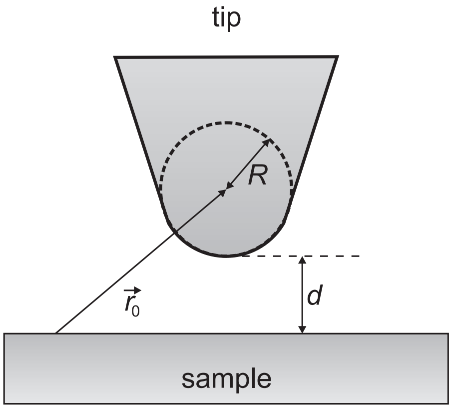

Figure 2.3: Geometry of the STM tip in the Tersoff-Hamann model. The tip has an arbitrary shape but a spherical geometry close to the surface with a radius R and distance d from the foremost end of the tip to the sample surface (adapted from Ref. [13]).

tip and E_μ the energy of the unperturbed state ψ_μ. The delta-function expresses that only elastic tunneling is taken into account which corresponds to the conservation of energy. In the limit of low temperatures the Fermi-Dirac distribution can be approximated by a step function and Eq. 2.6 can be simplified for small voltages ($\sim$ 10 meV for metals) to:

$$I = \frac{2\pi}{\hbar} e^2 U \cdot \sum_{\mu,\nu} |M_{\mu\nu}|^2 \cdot \delta(E_\nu - E_\mathrm{F}) \cdot \delta(E_\mu - E_\mathrm{F}) \,, \tag{2.7}$$

where E_F represents the Fermi level. Now the main difficulty is the calculation of the matrix elements that reflect the tunnel probability introduced in Eq. 2.4. A first approximation can be achieved by using localized tip states at $\vec{r}_0$ and Eq. 2.7 becomes:

$$I \propto \sum_\nu |\psi_\nu(\vec{r}_0)|^2 \cdot \delta(E_\nu - E_\mathrm{F}) = \rho_\mathrm{s}(\vec{r}_0, E_\mathrm{F}) \,. \tag{2.8}$$

The tunnel current is proportional to the local density of states (LDOS) at the Fermi level of the surface (sample) at the location $\vec{r}_0$ of the tip. A more general solution of Eq. 2.7 is based on the calculation of the tunnel matrix elements $M_{\mu\nu}$. As shown by Bardeen [12] the matrix elements are given by:

$$M_{\mu\nu} = \frac{\hbar^2}{2m} \cdot \int \mathrm{d}\vec{S} \cdot \left(\psi_\mu^* \vec{\nabla} \psi_\nu - \psi_\nu \vec{\nabla} \psi_\mu^* \right) . \tag{2.9}$$

The integration is performed over an arbitrary area within the vacuum barrier. An exact solution of Eq. 2.9 requires the knowledge of the energies of the wave functions and consequently the knowledge of the atomic structure of tip and sample. Since the tip geometry is in general unknown Tersoff and Hamann introduced the following simplified model of an STM tip. The tip has an arbitrary shape but the foremost end has a spherical symmetry. The curvature of the tip is given by R and the tip is facing the sample at a distance d. A schematic representation of the tip and sample geometry is shown in Fig. 2.3. By taking only s-like electronic states ($l = 0$) for the tip into account and assuming both tip and sample have identical work functions ϕ the tunnel current is given by:

$$I = 32\pi^3\hbar^{-1}e^2U\phi^2 \cdot \rho_\mathrm{t}(E_\mathrm{F}) \cdot R^2\kappa^{-4}e^{2\kappa R} \cdot \sum_\nu |\psi_\nu(\vec{r}_0)|^2 \cdot \delta(E_\nu - E_\mathrm{F})\,, \tag{2.10}$$

where $\kappa = \sqrt{2m\phi}/\hbar$ is the minimal decay constant and $\vec{r}_0$ the center of the tip curvature. The sum in Eq. 2.10 represents the LDOS at the Fermi level of the sample at the location $\vec{r}_0$ of the tip,

$$\sum_\nu |\psi_\nu(\vec{r}_0)|^2 \cdot \delta(E_\nu - E_\mathrm{F}) = \rho_\mathrm{s}(\vec{r}_0, E_\mathrm{F})\,, \tag{2.11}$$

where the exponential dependence of the tunnel current on the distance d is according to Eq. 2.5 given by the decay of the wave functions into the vacuum:

$$|\psi_\nu(\vec{r}_0)|^2 \propto e^{-2\kappa(R+d)}\,. \tag{2.12}$$

Together with Eq. 2.10 it follows:

$$I \propto U \cdot e^{-2\kappa d}\,. \tag{2.13}$$

In the framework of the discussed approximations (which are: small interaction between tip and sample, s-like tip states. small bias voltage $U \ll \phi$, $T = 0$ K, elastic tunneling and identical work functions $\phi_\mathrm{s} = \phi_\mathrm{t}$) the interpretation of topographic STM data is the following: The area $z(x,y)|_{I=\mathrm{const}}$ is according to Eq. 2.10 a trace of constant LDOS at the Fermi level of the surface at the location of the tip:

$$I = \mathrm{const.} \quad \rightarrow \quad \rho_\mathrm{s}(\vec{r}_0, E_\mathrm{F}) = \mathrm{const.}\,. \tag{2.14}$$

For chemically homogeneous surfaces the LDOS follows the topography to a good approximation and the constant current images can be interpreted as the topography of the surface. For chemically inhomogeneous samples the topographic interpretation reaches its limitations. Due to adsorbates, intermixing or the variation of the thickness of thin films the LDOS of the surface is modified and in general the constant current image no longer represents the topography of the surface. For example the LDOS is reduced by oxygen adsorbates on Fe(001) so that these adsorbates are imaged as dips although they are on top of the surface.

A further disadvantage of this simple model of the tip arises from atomically resolved images which can be achieved on various surfaces. The expected corrugation Δz of surfaces with the fundamental periodicity a can be expressed by [13, 14]:

$$\Delta z \approx \frac{2}{\kappa} \cdot \exp\left[-2\left(\sqrt{\kappa^2 + \frac{\pi^2}{a^2}} - \kappa\right) z\right] , \quad z = d + R . \tag{2.15}$$

On reconstructed surfaces such as Au(110) experimental results [13] are in good agreement with the Tersoff-Hamann model using reasonable parameters for the tip. Qualitatively a disagreement occurs on closed packed surfaces (for example Al(111) [15], Au(111) [16]) by an experimental corrugation of $\Delta z|_{\text{exp}} \approx 0.1 - 0.4$ Å. This inconsistency was solved by Chen [17] by a modification of the Tersoff-Hamann model allowing also other than s-like tip states. Since in STM mainly tungsten, platinum or iridium tips are used where d-like bands contributes about 85% to the LDOS at the Fermi level he introduced $l \neq 0$ tip states. On the basis of the so-called derivative rule [14] and the assumption of d_{z^2}-like tip states a better agreement with the experiment could be found.

2.4 Scanning tunneling spectroscopy (STS)

Beside the ability to image the sample surfaces as contours of constant LDOS in the topography mode the STM provides the possibility to gain spectroscopic information of the surface. The main advantage of scanning tunneling spectroscopy (STS) over spatially averaging techniques like photoemission (PE) or inverse photoemission (IPE) is the high energy resolution at low temperatures (a few meV or even less) in combination with the high spatial resolution. The latter is of importance if impurities or surface defects disturb the local electronic structure.

In STS the LDOS of the sample has a direct relation to the differential tunnel conductance $\mathrm{d}I/\mathrm{d}U(U)$ which is directly accessible via lock-in technique in the experiment. To record a full spectroscopy curve the tip is first stabilized at every point (x, y) of the image at U_{stab} and I_{stab} . After opening the feedback-loop, the bias voltage is linearly ramped from the stabilization value U_{stab} to a final value while a small modulation voltage of a few mV is added to U. Simultaneously, the $\mathrm{d}I/\mathrm{d}U(U, x, y)$ signal is measured.

In the previous section the tunnel process was described by the Tersoff-Hamann model in the limit of small bias voltages U between the two electrodes. For larger bias voltages U a relative shift of the Fermi levels of tip and sample has to be taken into account. By converting the sum of Eq. 2.10 into an integral over quasi continuous states one gets for $T = 0$ K a more general relation for the tunnel current I:

$$I \propto \int_0^{eU} \rho_\mathrm{s}(\vec{r}_0, E_\mathrm{F} + \epsilon) \cdot \rho_\mathrm{t}(E_\mathrm{F} - eU + \epsilon) \mathrm{d}\epsilon \,. \tag{2.16}$$

Here U conventionally denotes the voltage of the sample electrode relative to the tip electrode. As a consequence the tunnel current is proportional to the convolution of the LDOS of the sample $\rho_\mathrm{s}(\vec{r}_0)$ and the tip LDOS ρ_t in the energy interval $[0, eU]$ in between the Fermi levels of both electrodes. Figure 2.4 shows the system of tip and sample in tunnel contact in equilibrium and with applied sample bias voltage. The occupied states are indicated by the shaded region below the Fermi energy, the sample density of states is sketched by the curve inside the tunnel barrier. The difference between the Fermi energy E_F and the vacuum level E_vac is the work function ϕ (index t for tip and s for sample). In the equilibrium state in Fig. 2.4(a) the Fermi levels are equal and since $\phi_\mathrm{t} > \phi_\mathrm{s}$ the barrier is not rectangular. The net tunnel current is zero. Applying a bias voltage U leads to a shift of the Fermi levels by $|eU|$. At negative sample bias voltage U electrons from the sample in the energy interval from $E_\mathrm{F} - eU$ to E_F can tunnel into unoccupied states of the tip Fig. 2.4(b). For positive U the situation is reversed and electrons tunnel from occupied tip states into unoccupied states of the sample Fig. 2.4(c). As one assumes that the LDOS of the tip ρ_t is constant the derivative of Eq. 2.16 in the limit of small bias voltages is given by:

$$\frac{\mathrm{d}I}{\mathrm{d}U}(U) \propto \rho_\mathrm{s}(\vec{r}_0, E_\mathrm{F} + eU) \,. \tag{2.17}$$

In this approximation the differential tunnel conductance $\mathrm{d}I/\mathrm{d}U(U)$ represents the density of states of the sample at the location $\vec{r}_0$ of the tip at the energy $E_\mathrm{F} + eU$. Since the tunnel barrier depends on the voltage U the treatment of Eq. 2.17 is invalid for higher bias voltages. By introducing a transmission coefficient $T(E, U, s)$, similar to Eq. 2.5, the term $\rho_\mathrm{s}(\vec{r}_0, E)$ can be split into the density of states at the surface $\rho_\mathrm{s}(E) = \rho_\mathrm{s}(E,\, x, y, z = 0)$ and the transmission coefficient $T(E, U, s)$ [18] so that the tunnel current I is given by:

$$I \propto \int_0^{eU} \rho_\mathrm{s}(E_\mathrm{F} + \epsilon) \cdot \rho_\mathrm{t}(E_\mathrm{F} - eU + \epsilon) \cdot T(\epsilon, U, s) \, \mathrm{d}\epsilon \,. \tag{2.18}$$

Now the main difficultly is the choice of adequate transmission coefficients $T(E, U, s)$. In the framework of a semi-classical WKB-approximation the trans-

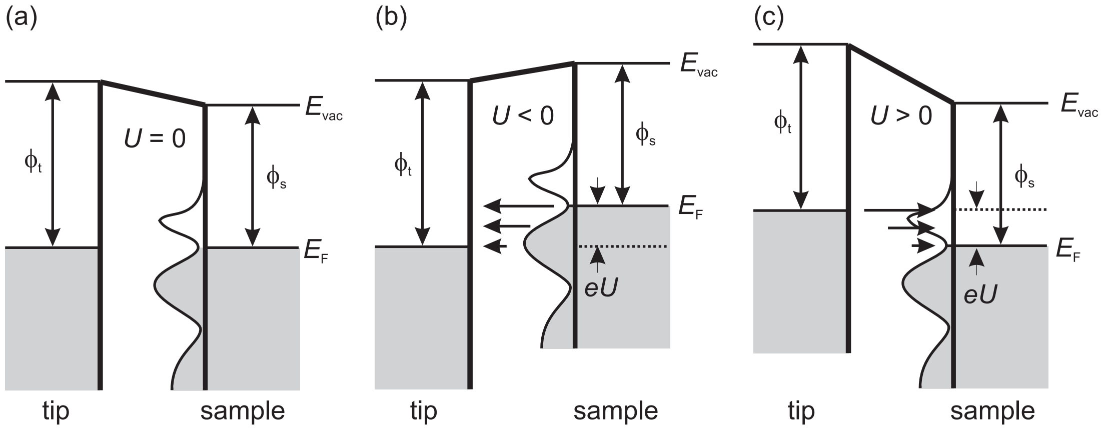

Figure 2.4: System of tip and sample in tunnel contact. (a) equilibrium, tunnel current occurs only until the Fermi levels are equal; (b) negative sample bias, net tunnel current from sample to tip; (c) positive sample bias, net tunnel current from tip to sample. The energy-dependent sample density of states is sketched by the curve inside the barrier.

mission coefficient can be written as [10, 19]:

$$T(E,U,s) \cong \exp[-2\kappa(E,U)s], \quad \kappa(E,U) = \sqrt{\frac{2m}{\hbar^2}\left(\bar{\phi} + \frac{eU}{2} - (E - E_{\|})\right)}\,. \tag{2.19}$$

Here $s = d + R$ is the effective tunnel distance and $\bar{\phi} = (\phi_\mathrm{s} + \phi_\mathrm{t})/2$ the average work function. The decay constant $\kappa(\epsilon, U, k_{\|})$ becomes minimal at a certain energy ϵ for states that have a vanishing wave vector parallel to the surface ($k_{\|} = 0$). Therefore, states at the $\bar{\Gamma}$-point of the surface Brillouin zone are more pronounced in STS. By partial integration and following differentiation of Eq. 2.18 a relation between the differential tunnel conductance $\mathrm{d}I/\mathrm{d}U(U)$ and the LDOS of the sample ρ_s is given by [19]:

$$\begin{aligned}\frac{\mathrm{d}I}{\mathrm{d}U}(U,s) \quad &\propto \quad \rho_\mathrm{s}(E_\mathrm{F}+eU)\cdot\rho_\mathrm{t}(E_\mathrm{F})\cdot T(eU,U,s) \\ &+ \int_0^{eU} \rho_\mathrm{s}(E_\mathrm{F}+\epsilon)\cdot\rho_\mathrm{t}(E_\mathrm{F}+\epsilon-eU)\cdot\frac{\mathrm{d}}{\mathrm{d}U}T(\epsilon,U,s)\,\mathrm{d}\epsilon \\ &+ \int_0^{eU} \rho_\mathrm{s}(E_\mathrm{F}+\epsilon)\cdot T(\epsilon,U,s)\cdot\frac{\mathrm{d}}{\mathrm{d}U}\rho_\mathrm{t}(E_\mathrm{F}+\epsilon-eU)\,\mathrm{d}\epsilon\,.\end{aligned} \tag{2.20}$$

In the first term we have the LDOS $\rho_\mathrm{s}(E_\mathrm{F} + eU)$ of the sample. Assuming a constant or weakly varying LDOS ρ_t of the tip the third term can be neglected.

The second term mainly contributes at high bias voltage due to the increase of the transmission coefficient T at high bias voltages.

Great care has to be taken when analyzing the data obtained in $\mathrm{d}I/\mathrm{d}U$ measurements. First of all the intrinsic value of $\rho_{\mathrm{s}}(E_{\mathrm{F}}+eU)$ cannot be measured directly even for a structureless LDOS of the tip because it is blurred by the voltage-dependent rise of the transmission coefficient T. In literature several possibilities for normalization of the $\mathrm{d}I/\mathrm{d}U$ curves are discussed. Feenstra *et al.* [20] used the normalization of the differential conductance by the total conductance: $\frac{\mathrm{d}I}{\mathrm{d}U}/\frac{I(U)}{U}$. In this method the dependence of the transmission coefficient T on the the distance s of tip and sample and on the bias voltage U is almost extracted. A disadvantage is that the positions of maxima of the $\mathrm{d}I/\mathrm{d}U$ curve are not well reproduced in certain cases [21] and one looses spectroscopic information close to the Fermi level ($U = 0$ V) as $\mathrm{d}I/\mathrm{d}U \approx I/U$ (ohmic behavior) and the normalized spectra always have the value 1. A second method was discussed by Ukraintsev [19]. Here a function $F(U, \alpha_{\mathrm{i}})$ with free parameters α_{i} is used to model the transmission coefficient T. The function $F(U, \alpha_{\mathrm{i}})$ is fitted to the experimental $\mathrm{d}I/\mathrm{d}U$ curves and after that the $\mathrm{d}I/\mathrm{d}U$ curves are normalized by $\frac{\mathrm{d}I}{\mathrm{d}U}/F(U)$. This method requires the knowledge of the function $F(U)$ which is in most cases not given. Furthermore, the stabilization parameters for spectroscopy can have an impact on the measured $\mathrm{d}I/\mathrm{d}U$ data. Especially when comparing spectra taken on areas with different electronic structure or work function one has to bear in mind that the topographic effect can have an influence on the measurement which may lead to incorrect interpretations (see Sec.2.1).

In summary the quantitative analysis of $\mathrm{d}I/\mathrm{d}U$ data can be quite complex and a various number of influences on spectroscopy curves has to be taken into account.

2.5 Energy resolution of STS at finite temperatures

In the previous section the high lateral resolution of scanning tunneling spectroscopy was discussed without treating the energy resolution of STS. At finite T it is limited by the thermal broadening of the Fermi distribution $f(E)$. A simple example may serve as an approximation:

The starting point is a hypothetic LDOS of the the sample $\rho_{\mathrm{s}}(E)$ with an unoccupied δ-peak just above the Fermi level E_{F}. The tip has a constant LDOS $\rho_{\mathrm{t}}(E) = \rho_{\mathrm{t}}$ and the occupation of the states is given by the Fermi-Dirac distribu-

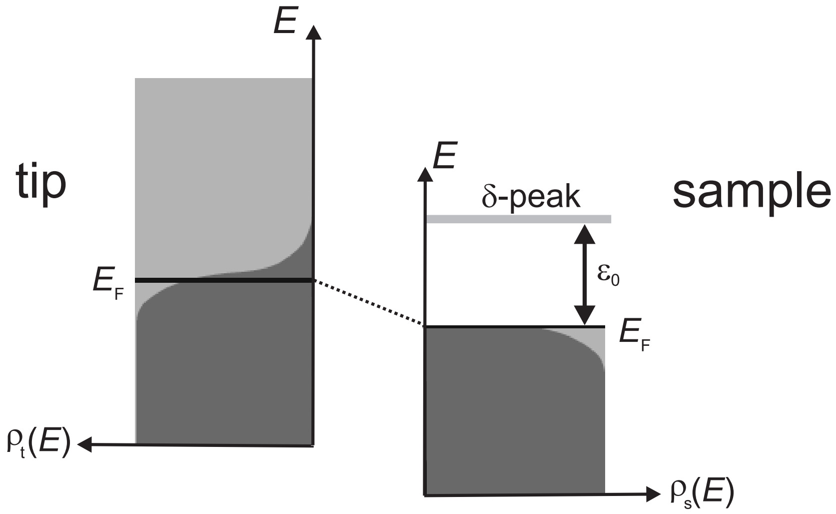

Figure 2.5: Energy scheme of a tunnel junction at a finite temperature. The sample has a δ-peak in the LDOS above the Fermi level. The tip LDOS is featureless. Occupied states are drawn in dark gray.

tion. In Fig. 2.5 a schematic representation of the tunnel junction is shown. The Bardeen formalism gives for the net current:

$$I = \frac{2\pi e}{\hbar} \int\limits_{-\infty}^{\infty} [f(\epsilon + eU) - f(\epsilon)] \cdot |M_{\mu\nu}|^2 \cdot \rho_{\mathrm{t}}(\epsilon + eU) \cdot \rho_{\mathrm{s}}(\epsilon) \mathrm{d}\epsilon \,. \tag{2.21}$$

Here U is the difference of the potentials of tip and sample, $\epsilon = E - E_{\mathrm{F}}$ the relative energy of the electrode with respect to the Fermi level and $f(\epsilon) = [\exp(\epsilon(k_{\mathrm{B}}T) + 1]^{-}1$ the Fermi-Dirac distribution. While looking at a small energy window the tunnel matrix elements $M_{\mu\nu}$ are constant. The derivative of Eq. 2.21 with respect to U is a representation of the differential tunnel conductance measured in STS:

$$\frac{\mathrm{d}I}{\mathrm{d}U}(U) \propto |M_{\mu\nu}|^2 \cdot \rho_{\mathrm{t}} \int\limits_{-\infty}^{\infty} \left[\frac{(1/k_{\mathrm{B}}T) \exp[(\epsilon + eU)/k_{\mathrm{B}}T]}{\exp[(\epsilon + eU)/k_{\mathrm{B}}T] + 1)^2} \right] \cdot \rho_{\mathrm{s}}(\epsilon) \mathrm{d}\epsilon \,. \tag{2.22}$$

Now one is interested in the dI/dU signal around the δ-peak of the LDOS of the sample. For a sample LDOS of $\rho_{\mathrm{s}}(\epsilon) = A\delta(\epsilon - \epsilon_0)$ one obtains for the differential tunnel conductance the following relation:

$$\frac{\mathrm{d}I}{\mathrm{d}U}(U) \propto \frac{1}{k_{\mathrm{B}}T} \cdot \frac{1}{\cosh^2(\frac{\epsilon_0 + eU}{2k_{\mathrm{B}}T})} \,. \tag{2.23}$$

The differential tunnel conductance has a pronounced maximum at $-eU = \epsilon_0$ and the dI/dU signal can be approximated by a Gaussian line shape with full width at half maximum (FWHM) of $2\sigma = 3k_\mathrm{B}T/e$. It means that two neighboring δ-peaks of the sample LDOS with a separation ΔE_0 are measured in the $\mathrm{d}I/\mathrm{d}U$ signal as two separated maxima if the following condition is fulfilled: $\delta E_0 > 3k_\mathrm{B}T_0$, where T_0 is the temperature of the tip. Hence the best possible energy resolution at a finite temperature can be defined as:

$$\Delta E = 3k_\mathrm{B}T\,. \tag{2.24}$$

A high energy resolution can only be achieved at low temperatures and an estimation leads to $\Delta E \approx 1$ meV for $T = 4$ K.

The actual energy resolution in the spectroscopy mode is not only limited by the thermal broadening but also by the amplitude of the modulation voltage U_mod which is added to the bias voltage U_bias to measure the $\mathrm{d}I/\mathrm{d}U$ by lock-in technique. The overall energy resolution can be expressed by [22]:

$$\Delta E = \sqrt{\Delta E_\mathrm{therm}{}^2 + \Delta E_\mathrm{mod}{}^2} = \sqrt{(3k_\mathrm{B}T)^2 + (2.5 \cdot eU_\mathrm{mod})^2}\,. \tag{2.25}$$

At room temperature the thermal broadening is the dominant contribution limiting the energy resolution but at low temperatures the amplitude of U_mod becomes more important.

2.6 Spin-polarized STM/STS

In the previous sections the conceptional description of STM and STS was done by neglecting the spin of the tunneling electrons. In my work, however, not only the structural and electronic characteristics of a sample system are of interest but also the magnetic properties. Therefore, the experiment has to be prepared in the way that it is sensitive to the spin of the tunneling electrons. Since the generally used tungsten or platinum/iridium tips only allow spin-averaged measurements a modification of the tips is necessary. Different approaches to achieve this goal exist, such as the use of optically pumped GaAs-tips [23], super-conducting tips with a Zeeman split density of states [24] or ferromagnetic (for example Fe, Ni, Co) or antiferromagnetic tips (for example Cr [25]). In this work ferromagnetic Fe-coated tungsten tips were used.

For a fundamental understanding of the principle of spin-polarized STS a tunnel junction of two ferromagnetic electrodes is considered. In the Stoner-model of itinerant band ferromagnetism the subbands with opposite spin-orientation are shifted due to exchange interaction. The energetically reduced majority bands (↑) and the energetically enhanced minority bands (↓) are filled with a different number of electrons at the Fermi level resulting in a net magnetization in the direction

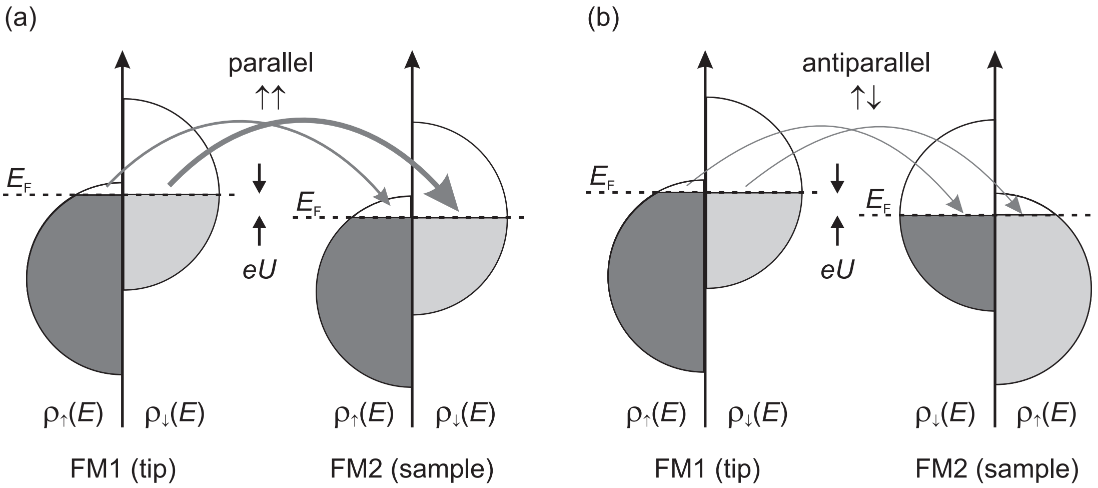

Figure 2.6: Principle of spin-polarized tunneling between two ferromagnetic electrodes with a parallel orientation of the magnetization in (a) and an antiparallel orientation in (b). For elastic tunneling and conservation of the spin the tunnel current is in case (a) larger than in case (b).

of the majority spins. It is useful to define the energy dependent spin-polarization given by:

$$P(E) \equiv \frac{\rho_\uparrow(E) - \rho_\downarrow(E)}{\rho_\uparrow(E) + \rho_\downarrow(E)} . \tag{2.26}$$

Here $\rho_\uparrow(E)$ is the majority DOS and $\rho_\downarrow(E)$ the minority DOS. The most important characteristic of electron tunneling between spin-polarized electrodes is spin conservation. Bearing this in mind the simple sketch in Fig. 2.6 clarifies the basic principle of spin-polarized tunneling on the basis of a spin-split density of states. For parallel magnetization (Fig. 2.6(a)) the majority electrons of electrode FM1 tunnel solely into unoccupied majority states of electrode FM2 and minority electrons solely into unoccupied minority states. For an antiparallel magnetization the situation is reversed (Fig. 2.6(a)) and the net current is smaller. This effect is called the spin-valve effect or TMR (tunnel magneto resistance)-effect. The first experimental proof of spin-polarized tunneling was achieved by Tedrow and Meservey in 1971 using planar superconductor-oxide-ferromagnet tunnel junctions (Al-Al_2O_3-Ni) [26] and by Julliere in 1975 using Fe-Ge-Co tunnel junctions [27].

In real systems, however, the magnetizations are not always aligned collinear but under a certain angle θ. Slonczewski has expanded the method of Sec. 2.2 for ferromagnetic electrodes in the limit of free electrons and small bias voltages and found for the tunnel conductance σ [28]:

$$\sigma = \sigma_0[1 + P_1(E)P_2(E)\cos\theta]\,. \tag{2.27}$$

Here $P_1(E)$ and $P_2(E)$ denote the effective spin-polarizations of the interfaces and σ_0 the average conductance. The cosine dependence was shown by Miyazaki and Tezuka [29] for planar Fe-Al_2O_3-Fe tunnel junctions. For the special cases of parallel and antiparallel alignment the conductance is given by:

$$\begin{aligned}\sigma_{\uparrow\uparrow} &= \sigma_0[1 + P_1(E)\cdot P_2(E)]\\ \sigma_{\downarrow\downarrow} &= \sigma_0[1 - P_1(E)\cdot P_2(E)]\,,\end{aligned} \tag{2.28}$$

and the effective polarization of the tunnel junction which can be measured in the experiment is defined as:

$$P \equiv P_1(E)\cdot P_2(E) = \frac{\sigma_{\uparrow\uparrow} - \sigma_{\downarrow\downarrow}}{\sigma_{\uparrow\uparrow} + \sigma_{\downarrow\downarrow}}\,. \tag{2.29}$$

The above described theory of spin-polarized tunneling can be directly applied to STM but now the spin-polarized transition occurs between tip and sample. A theoretical basis was given by Wortmann *et al.* as an expansion to the Tersoff-Hamann model [30, 31]. In this model the tip exhibits a constant density of states $\rho_{\mathrm{t}}^{\uparrow}$, $\rho_{\mathrm{t}}^{\downarrow}$ for both spin orientations. However, the absolute value of $\rho_{\mathrm{t}}^{\uparrow}$ and $\rho_{\mathrm{t}}^{\downarrow}$ is different leading to a non-vanishing spin-polarization and a magnetization of the tip. Moreover the tip states are s-like with the same decay constants into the vacuum of $\kappa = \kappa_{\uparrow} = \kappa_{\downarrow}$. Neglecting spin-flip processes the tunnel current in the limit of small bias voltages is given by:

$$I(\vec{r}_0, U, \theta(\vec{r}_0)) \propto \rho_{\mathrm{t}}\cdot\tilde{\rho}_{\mathrm{s}}(\vec{r}_0, E_{\mathrm{F}} + eU) + m_{\mathrm{t}}\tilde{m}_{\mathrm{s}}(\vec{r}_0, E_{\mathrm{F}} + eU)\,. \tag{2.30}$$

Here $\rho_{\mathrm{t}} = \rho_{\mathrm{t}}^{\uparrow} + \rho_{\mathrm{t}}^{\downarrow}$ is the total tip DOS, $\tilde{\rho}_{\mathrm{s}}(\vec{r}_0, U) = \int_0^{eU} \rho_{\mathrm{s}}^{\uparrow}(\vec{r}_0, E_{\mathrm{F}} + \epsilon) + \rho_{\mathrm{s}}^{\downarrow}(...)\,\mathrm{d}\epsilon$ the energy-integrated LDOS of the sample at the location $\vec{r}_0$ of the tip, $m_{\mathrm{t}} = \rho_{\mathrm{t}}^{\uparrow} - \rho_{\mathrm{t}}^{\downarrow}$ the spin-density of the tip, $\tilde{m}_{\mathrm{s}}(\vec{r}_0, U) = \int_0^{eU} \rho_{\mathrm{s}}^{\uparrow}(\vec{r}_0, E_{\mathrm{F}} + \epsilon) - \rho_{\mathrm{s}}^{\downarrow}(...)\,\mathrm{d}\epsilon$ the energy-integrated spin-density of the sample and $\theta(\vec{r}_0) = \theta(\vec{M}_{\mathrm{t}}, \vec{M}_{\mathrm{s}}(\vec{r}_0))$ the angle between the local magnetization of the sample $\vec{M}_{\mathrm{s}}(x, y, z = 0)$ and the tip magnetization $\vec{M}_{\mathrm{t}}$. The first summand of Eq. 2.30 describes the non-polarized contribution I_0 to the tunnel current and the second summand the spin-polarized contribution I_{p}. Analogous to Eq. 2.27 the tunnel current can be written as:

$$I(\vec{r}_0, U, \theta(\vec{r}_0)) \propto \rho_{\mathrm{t}}\cdot\tilde{\rho}_{\mathrm{s}}(\vec{r}_0, U)\Big(1 + P_{\mathrm{t}}\tilde{P}_{\mathrm{s}}(\vec{r}_0, U)\cos\theta(x_0, y_0)\Big)\,, \tag{2.31}$$

where $\tilde{P}_{\mathrm{s}}(\vec{r}_0, U) \equiv \tilde{m}_{\mathrm{s}}(\vec{r}_0, U)/\tilde{\rho}_{\mathrm{s}}(\vec{r}_0, U)$ is the local energy-integrated polarization of the sample. Figure 2.7 demonstrates the angular dependence of I_{p} for two

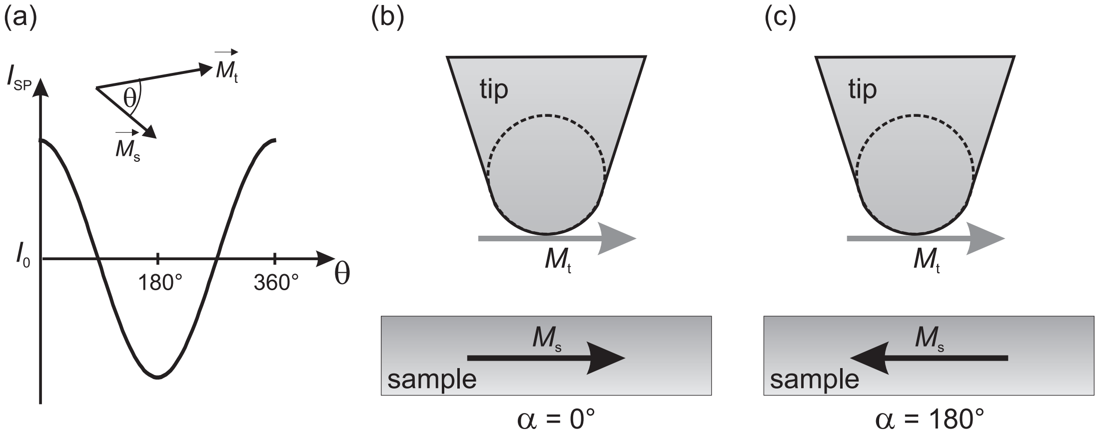

Figure 2.7: Spin-polarized tunneling. (a) angular dependence of the spin-polarized current $I_{\rm sp}$; sketch of a (b) parallel and (c) antiparallel alignment of the spin-polarized electrodes.

spin-polarized electrodes displayed as the sample surface and the STM tip. For an electronically homogeneous surface $\rho_{\rm t}$, $\tilde{\rho}_{\rm s}(\vec{r}_0, U)$ and $P_{\rm s}$ are independent of the location $\vec{r}$ on the surface. Therefore, any lateral variation of topographic height in a constant current image is caused by the $\cos\theta$-term in Eq. 2.31 which—with a fixed magnetization direction of the tip—only depends on the local orientation of the sample magnetization $\vec{M}_{\rm s}(\vec{r})$. Hence, the STM image reflects the local electron spin density of the sample surface. Assuming that the decay constant κ of the sample states is independent of the spin orientation the maximal displacement Δz can be described by:

$$\Delta z|_{\rm max} = \frac{1}{2\kappa} \ln\left(\frac{1 + P_{\rm t}\cdot\tilde{P}_{\rm s}(U)}{1 - P_{\rm t}\cdot\tilde{P}_{\rm s}(U)}\right), \quad \text{with } \kappa = \sqrt{2m\bar{\phi}}/\hbar\,. \tag{2.32}$$

For realistic parameters of $\phi = 4$ eV and $P_{\rm t}\cdot\tilde{P}_{\rm s} \approx 0.2$, $\Delta z|_{\rm max}$ is of the order of 0.2 Å. It is difficult to separate the height variation determined by Eq. 2.32 from the topography of the sample. This can be achieved only on atomically flat surface areas or if the magnetic and structural properties of the sample are well known [8, 32].

The spectroscopic mode of operation opens up the possibility to separate the magnetic information from the topography [33]. For imaging the magnetic structure of the sample the differential tunnel conductance is measured spatially resolved via dI/dU maps or by full spectroscopy curves. Within the spin-polarized tunneling model the differential tunnel conductance is given by:

$$\frac{\mathrm{d}I}{\mathrm{d}U}_{\mathrm{sp}}(\vec{r}_0, U, \theta(\vec{r}_0)) \propto \rho_{\mathrm{t}} \cdot \tilde{\rho}_{\mathrm{s}}(\vec{r}_0, E_{\mathrm{F}}+eU) + m_{\mathrm{t}} \cdot m_{\mathrm{s}}(\vec{r}_0, E_{\mathrm{F}}+eU) \cos\theta(\vec{r}_0) \quad \text{or,} \tag{2.33}$$

$$\frac{\mathrm{d}I}{\mathrm{d}U}_{\mathrm{sp}}(\vec{r}_0, U, \theta(\vec{r}_0)) \propto \frac{\mathrm{d}I}{\mathrm{d}U}_{\mathrm{sa}}(\vec{r}_0, U) + \Big(1 + P_{\mathrm{t}} \cdot \tilde{P}_{\mathrm{s}}(\vec{r}_0, E_{\mathrm{F}}+eU) \cos\theta(x_0, y_0)\Big) . \tag{2.34}$$

The differential tunnel conductance $\mathrm{d}I/\mathrm{d}U_{\mathrm{sp}}$ in a spin-polarized measurement is also separated into an unpolarized (spin-averaged) part $\mathrm{d}I/\mathrm{d}U_{\mathrm{sa}}$ and a spin-polarized part. The sensitivity of the spectroscopic mode is higher than the constant current mode because the magnetic contrast is directly correlated to the spin-polarized part of the differential tunnel conductance and not obtained from the logarithmic dependency of the tunnel current on the tip-sample separation. In particular it is possible to choose a bias voltage with a high product of $P_{\mathrm{t}} \cdot \tilde{P}_{\mathrm{s}}(\vec{r}_0, E_{\mathrm{F}} + eU)$.

On electronically homogenous surfaces the spin-averaged part $\mathrm{d}I/\mathrm{d}U_{\mathrm{sa}}$ and $\tilde{P}_{\mathrm{s}}(\vec{r}_0, E_{\mathrm{F}} + eU)$ are laterally constant and therefore any variation of the $\mathrm{d}I/\mathrm{d}U_{\mathrm{sp}}$ signal for a constant tip-sample separation reflects a variation of the sample magnetization and the differential tunnel conductance can be written as:

$$\frac{\mathrm{d}I}{\mathrm{d}U}_{\mathrm{sp}}(U, x, y) \propto C(1 + P_{\mathrm{sp}} \cos\theta(x, y)) \quad \text{with } P_{\mathrm{sp}} = P_{\mathrm{t}} \cdot P_{\mathrm{s}}(E_{\mathrm{F}} + eU). \tag{2.35}$$

Chapter 3

A variable-temperature STM (VT-STM) for 20-300 K

3.1 Introduction

This part of my thesis describes the variable-temperature scanning tunneling microscope that has been constructed in the first phase of the work. The STM was designed to meets three operational conditions: ultra-high vacuum (UHV), low temperatures and optional magnetic fields. For the purpose of our interest in investigations of surface magnetism of systems with reduced dimensionality such as thin films the instrument has been supplied with some unique features, like an easy tip exchange mechanism and the ability for operation at variable temperatures (20-300 K).

The motivation for designing the new instrument was interest in temperature dependent magnetic phenomena such as magnetic reorientation transitions [34, 35] or superparamagnetic behavior [36] of thin film systems. Ferromagnetic materials exhibit spontaneous magnetization below the Curie temperature T_C. The orientation of the magnetization without an external field is determined by the magnetic anisotropy, that describes the energy density which is necessary to force the magnetization out of the energetically favorable orientation. The anisotropy has different contributions, namely the crystal-, magneto-elastic-, interface-, shape-, and surface anisotropy. The latter three are dominant in thin films and determine the ferromagnetism in two-dimensional systems. A detailed description of the different contributions to the magnetic anisotropy can be found in [37]. The Curie temperature describes the transition between paramagnetic behavior ($T > T_\mathrm{C}$) and ferromagnetic behavior ($T < T_\mathrm{C}$) and a typical value for bulk Fe is $T_\mathrm{C} = 1043$ K. For thin films the Curie temperature decreases with decreasing film thickness.

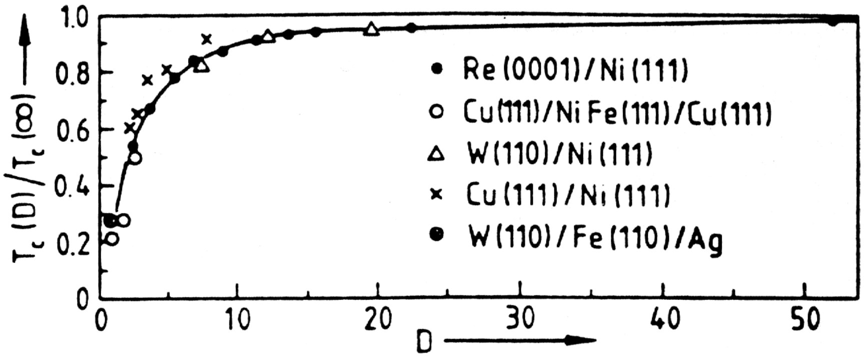

Figure 3.1: Dependence of T_C on the film thickness D (ML) for different magnetic systems taken from [34]. Solid line describes the fit with the finite scaling model.

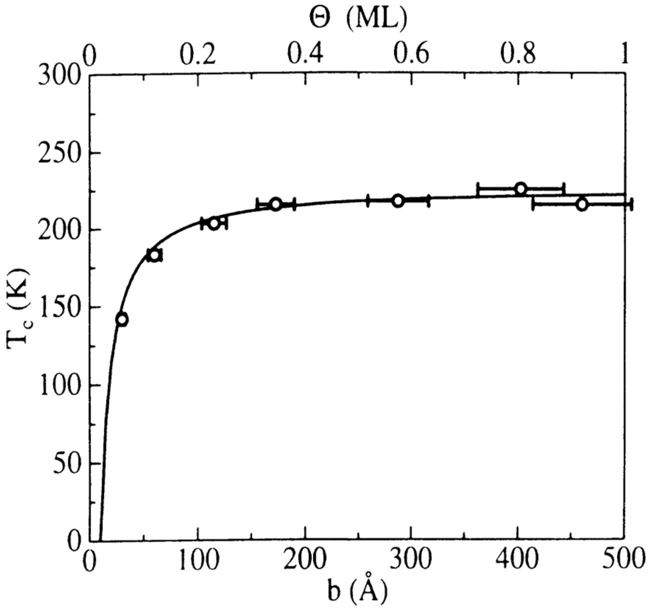

Figure 3.2: Dependence of T_C on the coverage Θ (top scale) and the stripe width b (bottom scale) for Fe/W(110) in the sub monolayer range taken from [37]. The solid line describes the fit with the finite scaling model.

Fig. 3.1 and 3.2 show experimental data of the variation on the Curie temperature with film thickness. The data points can be fitted with the finite size scaling model, which describes the theory of critical phase transitions [37]:

$$\frac{T_C(\infty) - T_C(\gamma)}{T_C(\infty)} = (\frac{\gamma}{\gamma_0})^{-\frac{1}{\nu}} . \tag{3.1}$$

Here $T_C(\infty)$ is the Curie temperature of the bulk system (cf. Fig. 3.1) or the Curie temperature of the closed monolayer (cf. Fig. 3.2). The factor γ denotes the film thickness D and the coverage Θ respectively and ν is the critical exponent[1]. γ_0 describes the value where the ferromagnetic ordering disappears for $T = 0$ K. The model shows good agreement with the measured data. In a simplified point of view the reduction of the Curie temperature with decreasing film thickness can be explained by the smaller number of neighboring spins in the system [37]. Therefore many thin film systems require low sample temperatures.

The Curie temperature does not always show the dependence given by Eq. 3.1 on the coverage. This holds especially for the transition from three-dimensional to two-dimensional systems. In [38] it is shown that the geometrical structure of Fe/W(110) in the sub-monolayer regime has a strong influence on T_C. The Curie temperature for Fe islands has a much lower value than for Fe stripes. Due to morphological changes T_C can even show a discontinuous form as described in [39] for Co/Cu(001). For this system the Co islands start to coalescence at a coverage of 1.8 ML and T_C rises by approximately 100 K. Obviously, Eq. 3.1 describes only a general trend and has to be verified explicitly for each system.

In the following chapters the conceptual design for optimal operation of the instrument will be described where especially the combination of ultrahigh vacuum, low- and variable temperatures and scanning probe microscopy has some difficulties to be taken into account. First, an introduction to variable-temperature STMs and a comparison of existing variable-temperature STM instruments is given. After that the design used in this work will be described. The following chapters describe the components in detail and finally first test measurements are shown to demonstrate the performance of the instrument.

3.2 Comparison of existing VT-STM instruments

Nowadays there are several UHV-STM instruments known that work at base temperatures of 4-15 K and have a high mechanical stability (e. g. [40, 41]). These instruments have a ^{4}He dewar that is thermally connected to the STM. On the other hand even 20 years after the development of the STM by Binnig and Rohrer (1981) only a few instruments that work with a good stability at variable temperatures are described in literature [42–52]. To achieve variable temperatures two different approaches exist. The first approach is to use a ^{4}He bath cryostat.

---

[1] In three dimensions $\nu = \nu_3 = 0.705$, in two dimensions $\nu = \nu_2 = 1$

In this case the temperature is varied starting at the base temperature by using a heater. The disadvantage of this procedure is that above a temperature of about 20 K particles of the residual gas that were adsorbed at the cold surface of the cryostat start to desorb and partly adsorb on the sample leading to contamination of the surface. In a second approach the sample is cooled by a liquid He flow cryostat and the temperature can be adjusted by the amount of He that flows through the cryostat. Here a disadvantage is the continuous flow of liquid He that leads to mechanical vibrations. Therefore, the thermal anchoring is of great importance. On one hand a mechanical decoupling of the cryostat and the STM is desired and on the other hand the thermal contact should be as good as possible.

In the literature one finds two different realizations using a liquid He flow cryostat. One possibility is to cool only the sample so that the mass that has to be cooled can be kept low and a rapid variation of the temperature is possible [42–45, 51]. With a thermally compensated design it is possible to continuously image the surface while changing the temperature [42, 45]. A second realization is by cooling the entire STM [47, 52]. These systems are designed similar to the system with a bath cryostat. The STM is situated inside a radiation shield and operates at a base temperature of about 8-10 K. By cooling both tip and sample high resolution spectroscopy is possible but the variation of the temperature suffers the same problem as in the case of a bath cryostat.

In the following our approach for variable-temperature STM measurements is described.

3.3 Conceptual design of the VT-STM

As mentioned in the previous section the VT-STM is designed to fulfill three main purposes. The STM should be UHV compatible, work at variable temperatures of 20-300 K and has an easy tip exchange mechanism. As shown in Sec. 2.5 the energy resolution of STS is restricted by the temperature of the tip. In order to have the possibility of high energy resolution STS at low temperatures it is necessary to cool the entire microscope including tip and sample.

First, the type of cryostat has to be chosen. As it should be possible to measure at any temperature in the range of 20-300 K the realization with a bath cryostat is not practicable. Instead, we decided to use a liquid helium flow cryostat. The cryostat can either be operated with liquid He or liquid nitrogen and the temperature is varied by adjusting the amount of the refrigerant that flows through the cryostat. The cryostat has an integrated heater to stabilize the temperature the. The cooling concept of the flow cryostat has two stages. The first is the

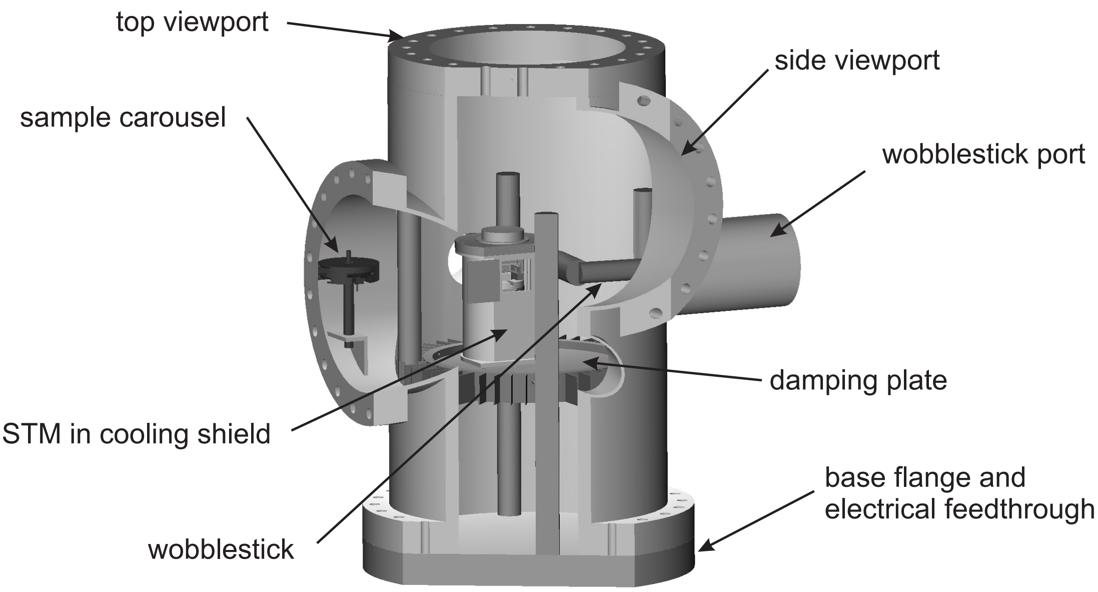

Figure 3.3: Section of the STM-chamber. The STM is situated inside a radiation shield that is placed on top of an eddy current damping stage. The STM-chamber is also shown in Fig. 4.1.

heat exchanger of the cryostat that is directly cooled by the liquid refrigerating medium and has the highest cooling power. The microscope itself is connected to the heat exchanger. The second stage, is the radiation shield of the cryostat, which is cooled by the exhaust. The radiation shield surrounding the microscope has two purposes. First of all the microscope is shielded from thermal radiation of the surrounding chamber. The second is the suspension of the STM is connected to the radiation shield and therefore the microscope is thermally decoupled from the environment that has a temperature of about 300 K.

An important part in the design of a STM is the vibration isolation. We decided to use an eddy current damping stage delivered by the company Omicron [42]. This damping stage is built up of a massive copper plate (300 mm diameter and 30 mm thickness) that is suspended by four metal springs. The STM inside the radiation shield is placed on top of the copper plate. The connection of the STM and the flow cryostat is realized by high flexible copper braids which have a high thermal conductivity. Their flexibility avoids the transmission of vibrations from the cryostat into the microscope. Fig. 3.3 shows a schematic representation of the STM-chamber.

In the following sections the setup of the instrument will be described in more detail. First the microscope is described followed by a description of the flow cryostat and the cooling concept. Finally, first test measurements which confirm the high performance of the STM will be presented.

3.4 The STM-body

The heart of the instrument is the variable-temperature STM with the *in situ* tip exchange mechanism developed by D. Haude [41]. The main objective in the setup of an STM is a stable tunnel contact, that must be well-isolated from mechanical, acoustic or electronic noise sources. A very compact design with a high resonance frequency is desired. The combination with an external damping system with a low resonance frequency results in an effective filter against external mechanical vibrations. The materials used in the microscope have to be selected for UHV compatibility and magnetic properties. The materials should have a low vapor pressure and should not exhibit remanence or high susceptibility. To achieve a good thermal equilibrium the materials should have a high thermal conductivity and the thermal expansion coefficients of the different materials should not vary to much. Since not all requirements can be achieved simultaneously the best possible compromise has to be identified.

The coarse approach mechanism that moves the tip towards the sample is of special importance because it is a part of the tunnel junction and should be mechanically stable. In low temperature STM instruments piezoelectrically driven step motors are often used for the coarse approach and are built up in the "walker" design [53]. This design is very stable and known to work reliably [40, 41]. Although the design is quite compact it allows macroscopic movements of about 20 mm at high driving force. Both features are necessary for the *in situ* tip exchange mechanism. Fig. 3.4(a) shows a photograph of the VT-STM. Vertical and horizontal cross sections are shown in Fig. 3.4(b). The sample is mounted face down in the sample holder and the tip approaches from below to the sample. The STM tip is fixed inside the tube scanner and the tube scanner itself is glued on a macor base inside the sapphire prism of the coarse approach mechanism. By integrating the scanner into the sapphire prism the design of the microscope is very compact but still allows about 20 mm travel. A the GaAs/GaAlAs diode sensor glued into the STM-body is used to measure the temperature.

The STM-body can be separated into two parts with the sample holder in the upper part and the coarse approach mechanism in the lower part of the STM-

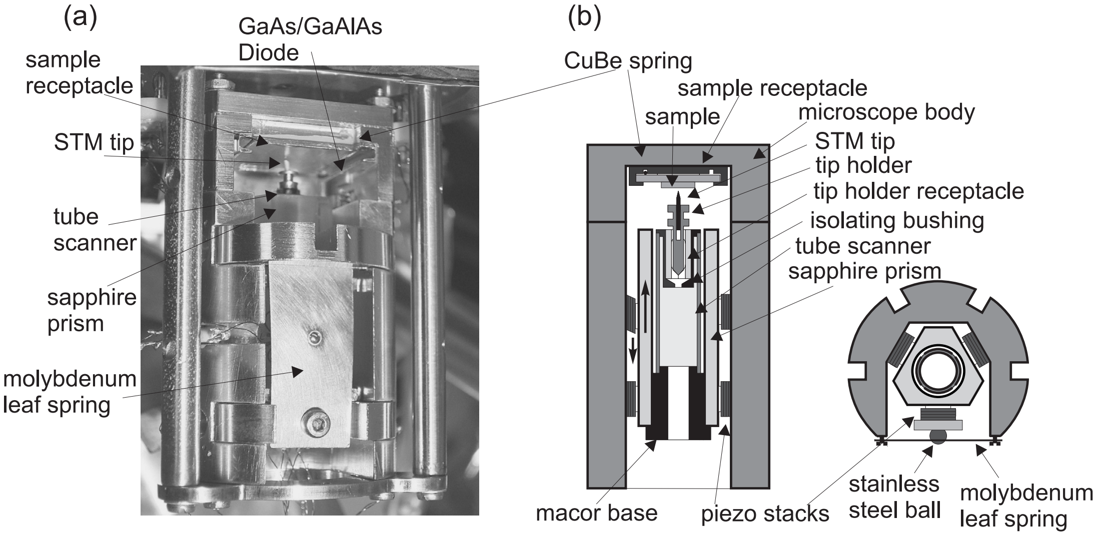

Figure 3.4: (a) Image of the VT-STM. (b) Schematic drawing of the VT-STM in vertical section (on the left) and horizontal section (on the right). The diameter of the microscope is 32 mm and the length 50 mm. The compact design is achieved by the integration of the tube scanner into the sapphire prism and results in a rigid mechanism for the coarse approach.

body. To reach a good thermal equilibrium the body and most other parts of the microscope were fabricated from phosphor bronze instead of the often used ceramic macor. Compared to macor phosphor bronze has a relative good thermal conductivity of $\lambda(4K) \approx 0.02$ W/cmK [54] and a mechanical stiffness comparable to stainless steel. Even small part can be manufactured easily from this material. The STM-body has a diameter of 32 mm and a length of 50 mm and the sample holder used to transfer the sample into the UHV system has a size of 18×15 mm^2. To have good thermal contact all parts of the microscope are polished and gold plated (5 μm).

The gold-plated sample holder has to be electrically isolated from the body of the STM. In order to have good thermal contact it was glued into the head of the microscope using a thin layer of non-conductive epoxy glue that has a high thermal conductivity [55].

A schematic of the coarse approach mechanism is shown in Fig. 3.4(b). At the center of the microscope one finds the moving part, a polished sapphire prism bearing the scanner tube, that is placed in a V-shaped groove. The sapphire prism is rigidly clamped by two sets of three shear piezo stacks [56]. A 5 mm × 5 mm × 1 mm Al_2O_3 pad is glued on top of each shear piezo stack.

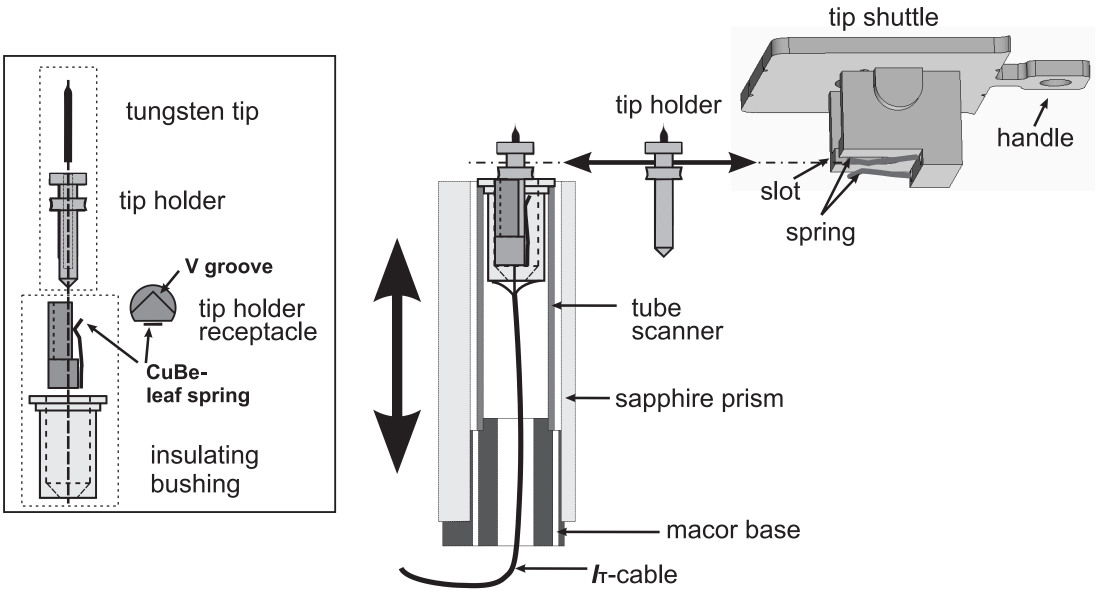

Figure 3.5: Schematic drawing of the tip exchange mechanism.

These pads provide the actual contact areas between the stacks and the sapphire prism surface. Two of the piezo stacks are glued to a phosphor bronze beam which is pressed onto the prism by means of a molybdenum leaf spring and a stainless steel ball. The phosphor bronze beam functions as a balance and ensures an equal distribution of the spring force to all contact areas of the six shear piezo stacks and the prism surface. In contrast to previous designs we do not employ walker stepping but use inertial movement by applying an asymmetric saw-tooth voltage curve to all six stacks simultaneously (stick-slip). On the slow slope of the voltage ramp the prism follows the shear movement (stick) while, due to its inertial mass, it is unable to follow the rapid relaxation of the piezos on the steep slope (slip). This results in one step of the prism per period. The mechanism is driven at $0.5 - 1$ kHz and the step size can be tuned by varying the applied voltage. During coarse approach the tip is moved towards the sample to a distance of less than 0.2 mm by manually controlling the motor with a remote control box. This operation can be easily controlled visually through one of the viewports with an optical microscope. Subsequently, the fine approach is accomplished in automatic mode of the STM control unit. During a measurement the sapphire prism stays firmly clamped to the microscope body.

The scanner used is made from a 1/4” EBL#4 piezo tube [56] with a length of 27.5 mm. This offers a scan range of 4.8 μm at low temperatures (4 K), which is more than the typical domain size of thin films. Due to the temperature-dependence of the piezo-electric-effect the room temperature scan range is about 9 μm. The resulting resonance frequency of the tube scanner of about $f_{\mathrm{res}} = 2.4$ kHz is still sufficient.

When working with magnetically coated tips it is expected to be able to prepare and exchange tips *in situ* in a short time. Thus a tip exchange mechanism is indispensable. Fig. 3.5 shows the assembly schematically. The tip is fixed in a molybdenum tip holder. For inserting a tip into the scanner the tip holder is carried by means of the shuttle which can be placed into the sample receptacle. Here it is positioned so that the tip holder lines up precisely below the retracted scanner. Driving down the linear motor lets the tip holder slip into the V-shaped groove of the tip receptacle which is mounted inside an insulating bush within the upper end of the scanner tube. A small leaf spring clamps the tip holder. Now the transporter can be retracted, leaving holder and tip firmly attached to the scanner tube. Tip and sample exchange is carried out using a wobble stick which allows simple and safe operation. Tip exchange take a few minutes and sample exchange is even faster. A whole tip preparation procedure, including coating, takes less than one our.

3.5 Thermal anchoring of the STM to the liquid He flow cryostat

This section focusses on the thermal coupling of the microscope to the cryostat and the thermal decoupling of the instrument to the environment. As described in Sec. 3.3 the microscope is inside a radiation shield. Fig. 3.6 shows a schematic of the microscope inside the radiation shield. It has a cylindrical shape and is placed on top of the eddy current damping stage. The radiation shield has a shutter at the front to access to the microscope. The STM itself is connected to the top of the radiation shield that is mounted removably to the cylindrical body of the radiation shield. Since the radiation shield has a higher temperature than the STM the thermal contact should be as small as possible. This was achieved by a suspension made of stainless steel. Stainless steel is non-magnetic and stiff material with a rather low thermal conductivity of $\lambda_{st} = 0.15$ W/Kcm at room temperature that falls by about two orders of magnitude at low temperature [54]. The suspension consists up of a lower plate where the STM is mounted and an upper plate that is connected to the top of the radiation shield. The two plates are fixed with each other by three tubes with a diameter of 5 mm and a wall

$T_{\mathrm{cryo}}[K]$	P[W]
4.2	1
10	2
20	3.5

Table 3.1: Cooling power of the heat exchanger of the cryostat [57].

thickness of 0.5 mm. Therefore, heat from the radiation shield is only carried via the three stainless steel tubes to the STM-body. The heat transfer through a solid with a temperature difference of ΔT can be calculated using:

$$P_{\mathrm{i}} = \frac{A_{\mathrm{i}}}{l_{\mathrm{i}}} \cdot \lambda_{\mathrm{i}} \cdot \Delta T \,. \tag{3.2}$$

Here A_{i} is the cross-section and l_{i} the length of the solid and λ_{i} the thermal conductivity. The maximum heat transferred by the stainless steel tubes can be estimated for $\Delta T = 300$ K to 1.9 W. Therefore it is guaranteed that heating power of the cryostat is sufficient at low temperatures [cf. Table 3.1]. Six ruby balls are used to decouple the upper plate of the suspension from the shield The ruby balls are used to separate the plate from the top of the shield and function as point contacts having minimal thermal transmission.

Beneath the mounting of the STM also the wiring has to be done carefully. The wiring was separated into two parts. The first part bridges the distance from the vacuum feedthrough to the cooling shield. For the I- and the U-signal coaxial twisted pair cables made of stainless steel with kapton insulation were used. All other electrical supplies were done by copper cables with a diameter of 0.125 mm and kapton insulation. The second part of the wiring has to bridge the distance from the top of the radiation shield to the STM. Here it is important to use cables with a low thermal conductivity. Kapton insulated manganin wires with a diameter of 0.051 mm were used since they have a low thermal conductivity at room temperature of $\lambda_{\mathrm{mang.}} = 0.22$ W/Kcm and the wires are easy to handle.

The cooling is performed by a continuous flow liquid He cryostat. The thermal anchoring of the STM to the heat exchanger of the cryostat is realized by a highly flexible copper braid. It consists of about 800 silver plated copper wires with a diameter of 0.05 mm. The copper braids are fed through small openings into the radiation shield and are screwed tightly onto the STM-body. The radiation shield is cooled by the exhaust gas of the cryostat via a second copper braid. Fig. 3.7 shows two photographs of the radiation shield inside the vacuum chamber as seen through the viewports.

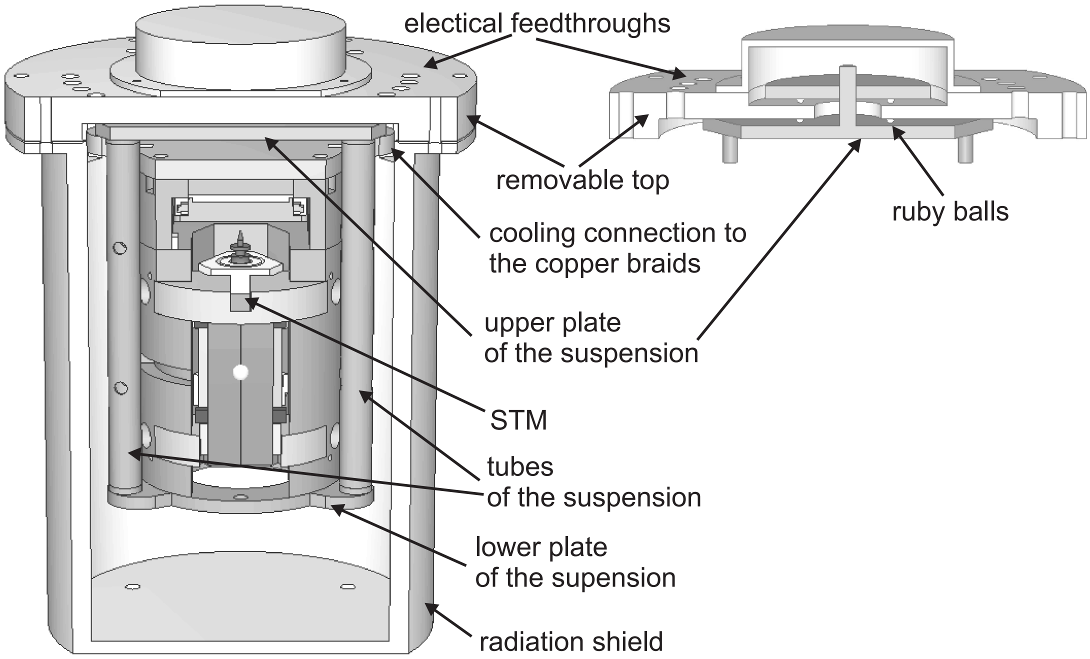

Figure 3.6: Schematic drawing of the STM inside the radiation shield. On the left a section of the radiation shield is shown. The microscope is mounted on top of a stainless steel plate that is connected via three stainless steel tubes to an upper plate. On the right the mounting of the upper plate to the top of the shield is shown. Six ruby balls are pressed in between the plates of the suspension and the top of the shield.

3.6 The liquid He flow cryostat

A commercial liquid He flow cryostat from CryoVac [57] is used in the VT-STM. The liquid He flows through a stainless steel tube into the cryostat and cools the heat exchanger located close to the microscope. After passing the heat exchanger the He gas is pumped by a rotary pump into the He recovery line. A needle valve is used to adjust the He pressure and minimize the He consumption while maintaining a laminar flow produces a stable temperature. Turbulent flow of the helium through the heat exchanger would result in mechanical vibrations, variations of the He pressure and unsteady heat transport. An extra valve allows the needle valve to be bypassed. When connecting a new He dewar it is necessary to flush the He line several times.

The thermal coupling of the heat exchanger to the microscope is achieved with highly flexible copper braids. To have good thermal contact of the copper braid to the heat exchanger the copper braid is soldered to the heat exchanger.

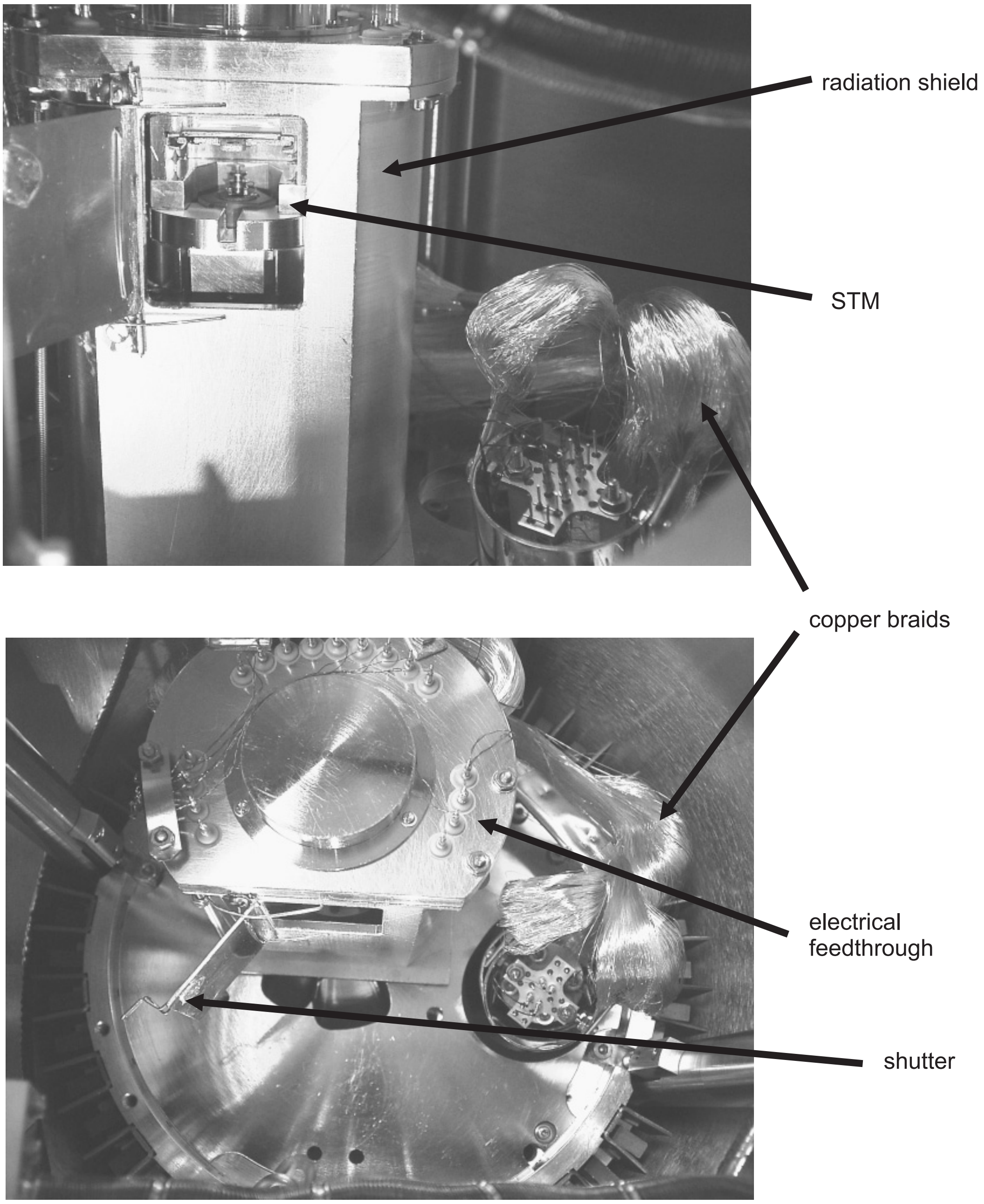

Figure 3.7: View of the radiation shield. In the upper picture the microscope can be seen through the open shutter. The lower image shows a top view of the radiation shield. The radiation shield is placed on top of the damping stage. In both images the heat exchanger and the copper braids are visible on the right.

The temperature of the heat exchanger is measured by a Si-diode. Stable temperature of the cryostat are achieved with an integrated heater regulated by a (PID)-temperature controller. To minimize the He consumption first of all the He flow through the cryostat is adjusted so that the heat exchanger is slightly below the desired temperature. After that the (PID)-controller is switched on which then regulates the temperature automatically and stability of a few hundredth of a Kelvin is achieved.

The STM temperature has a slightly higher temperature than the heat exchanger. An additional temperature sensor (a GaAs/GaAlAs diode) is glued to the body of the microscope to measure the sample temperature. The cooling performance is demonstrated in Fig. 3.9(a). The STM-body cools down with a linear decay of about 150 K/h and reaches the lowest base temperature after 2 hours. Fig. 3.9(a) shows that the final temperature of 6 K at the heat exchanger is

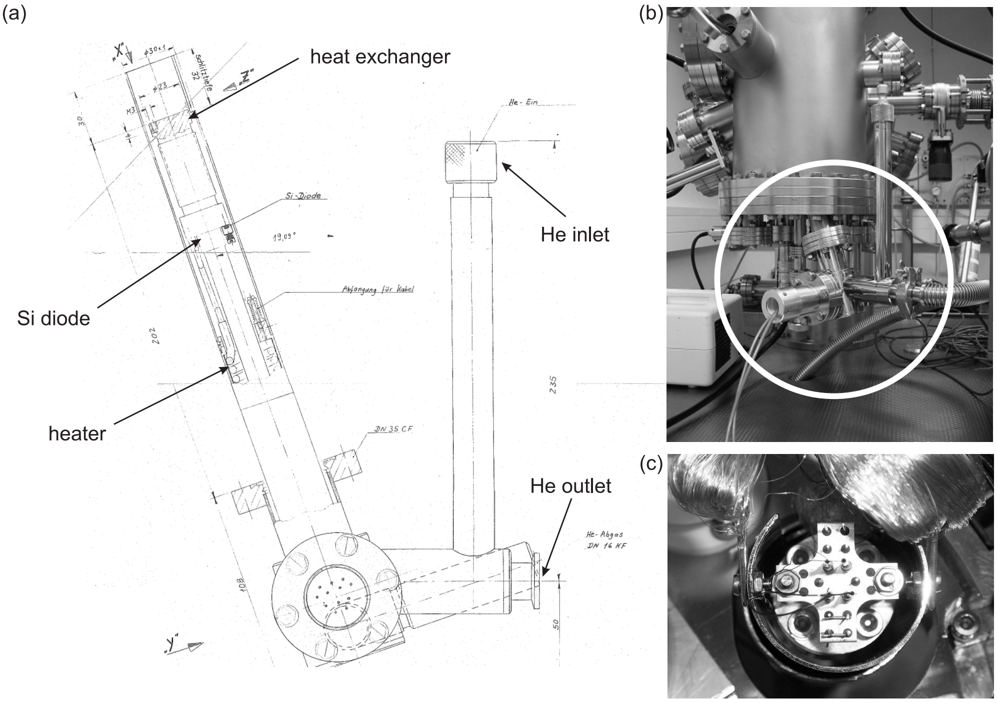

Figure 3.8: (a) Drawing of the liquid He flow cryostat [57]. Liquid He goes through the inlet into the cryostat, cools the heat exchanger and leaves the cryostat through the outlet. A Si diode is used to measure the temperature at the heat exchanger. The integrated heater that is regulated by a (PID)-temperature controller allows the stabilization of a desired temperature at the heat exchanger. (b) The STM vacuum chamber. The cryostat inside the chamber marked by the circle is only shown by its flange at the bottom. (c) View of the heat exchanger in the vacuum chamber.

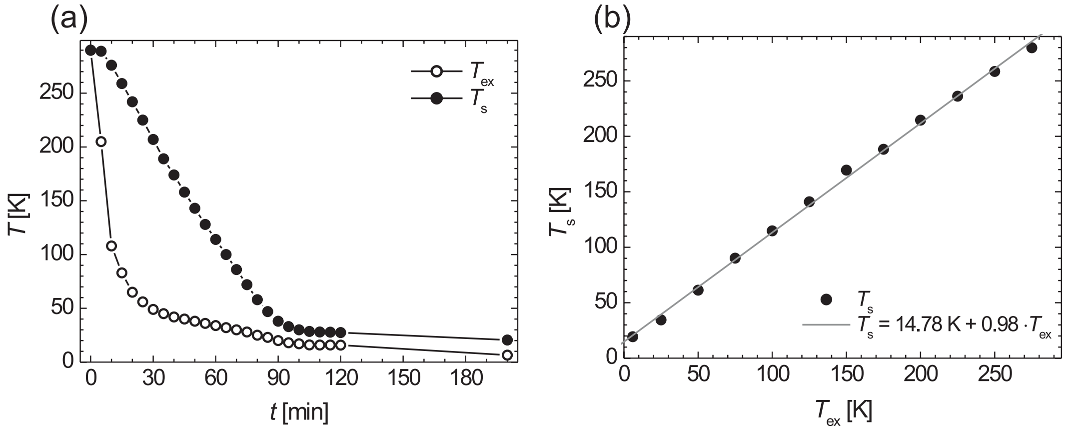

Figure 3.9: Cooling response curves of the cryostat and the STM. (a) The variation of the temperature of the heat exchanger and the microscope during cool down. The temperature of the heat exchanger decreased rapidly during the first 30 minutes, while the microscope temperature follows with a delay. After about 2 hours the heat exchanger and the microscope start to stabilize. (b) Dependence of the microscope temperature on the set point of the heat exchanger.

reached rather quickly while the sample temperature follows with a delay and the temperature difference during the cool-down is at most about 200 K. The dependence of the temperature at the microscope on the regulated temperature of the heat exchanger gives the graph shown in Fig. 3.9(b). From this graph one can estimate the set point of the heat exchanger for a desired sample temperature. The microscope temperature is always about 15 K higher than the temperature of the heat exchanger. The sample temperature T_s as a function of the heat exchanger temperature T_{ex} is given by:

$$T_s = 14.78\,\mathrm{K} + 0.98 \cdot T_{ex}\,. \tag{3.3}$$

3.7 Characterization of the VT-STM

Various tests were performed characterize the instrument using well known samples. The performance over the whole temperature range was of interest and in particular the STM was tested by atomically resolved imaging of surfaces and spectroscopy at low temperatures.

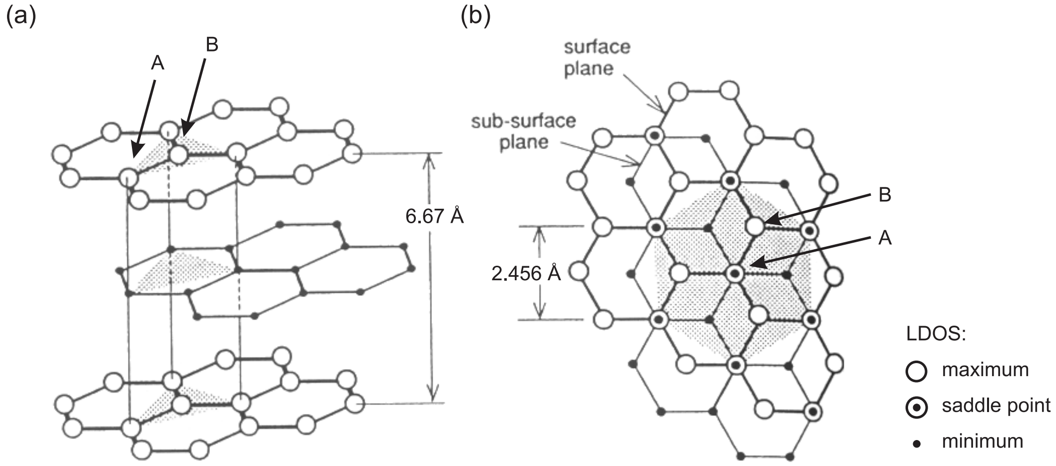

Figure 3.10: Crystal structure of HOPG. (a) Side view of three atomic layers. The atom positions A and B are due to the shift of the layers not equivalent: Since atom A has a next nearest neighbor in the layer below atom B is located above a hollow site. (b) Top view of the crystal structure. The three different symbols represent the LDOS of the different atom positions. While A denotes a saddle point, B represents a maximum of the LDOS. The hollow sites show a minimum of the LDOS. The images were taken from Ref. [10].

HOPG(0001)

Graphite is probably one of the most investigated layered sample system in scanning tunneling microscopy. The (0001) surface of graphite is relatively inert and forms large terraces with a width of several thousand Å. The graphite surface has hexagonal symmetry as shown in Fig. 3.10 and forms layers of covalently bonded atoms with a honeycomb structure. The layers are stacked in an ABAB sequence and hold together by weaker Van-der-Waals bonds. As a consequence of the ABAB stacking the neighboring atom positions are not equivalent: atom (A) has a direct next nearest neighbor in the layer below while (B) is located above a hollow site of a C-ring. The LDOS of atoms (A) and atoms (B) are expected to be different. Band structure calculations of graphite show that the LDOS has a maximum for atoms (B) and a saddle point for atoms (A) close to the Fermi level, while the hollow sites show a minimum [10]. Instead of a honeycomb a hexagonal structure is formed seen in STM images.

Fig. 3.11 shows STM images of the HOPG(0001) surface measured at four different temperatures. Fig. 3.11(a) was obtained at RT and Fig. 3.11(d) was measured in the low temperature regime. (c) and (d) show images at intermediate

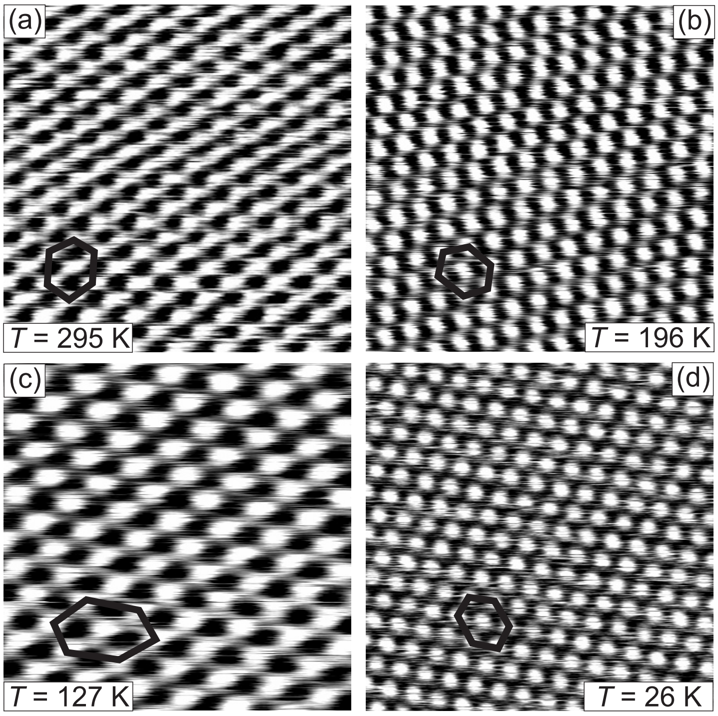

Figure 3.11: Constant current STM images of the HOPG surface at four different temperatures. The images were obtained with (a) $U = -35$ mV and $I = 1.06$ nA at 295 K, (b) $U = -42$ mV and $I = 500$ pA at 196 K, (c) $U = -88$ mV and $I = 921$ pA at 127 K, and (d) $U = -135$ mV and $I = 630$ pA at 26 K. At all four temperatures the structure of the HOPG(0001) surface was atomically resolved.

temperatures in between. The hexagonal ordered maxima on the surface are imaged in all four cases and reflect the B-site atoms. The images were used for a first lateral calibration of the scanner and show that it is possible to obtain atomically resolved images over the entire temperature range of 20-300 K.

NbSe$_2$

In the VT-STM the temperature sensor is coupled to the body of the STM. The sample itself is clamped by springs into the sample receptacle that is glued to the body of the STM. In general the sample and the body of the STM should have almost the same temperature. But it may be happen that the thermal contact of the sample to the body of the STM is not adequate, so that a temperature difference exists. To check this measurements were performed on a niobium diselenide (NbSe$_2$) sample which exhibits a charge density wave (CDW) at temperatures below $T_C = 33$ K. It is a layered system like HOPG that is characterized by a

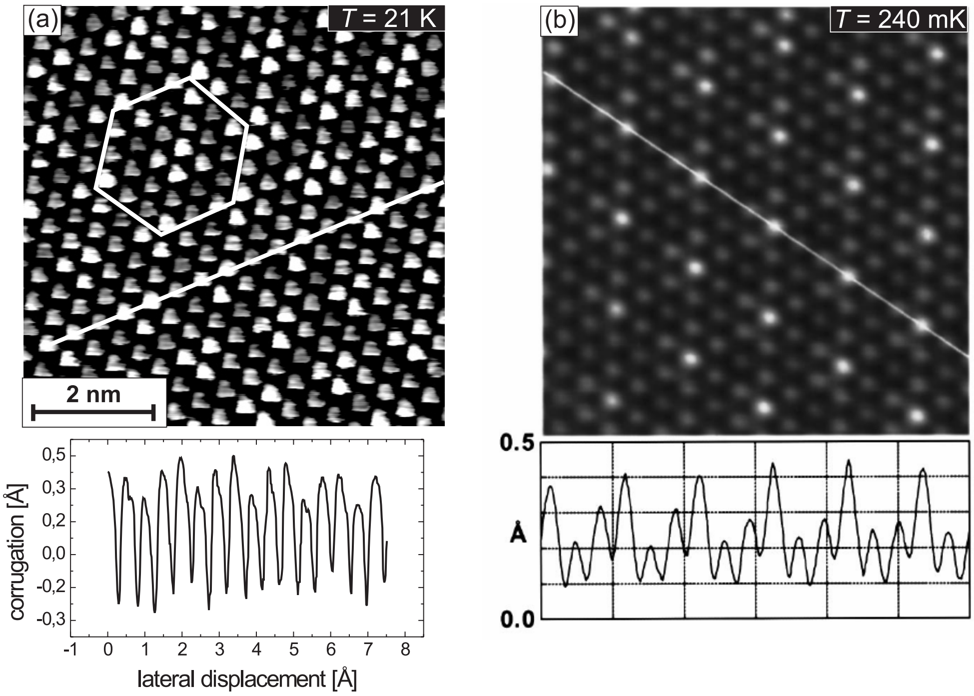

Figure 3.12: (a) Constant current STM images of $NbSe_2$ ($I = 40$ pA, $U = 30$ mV). Due to the charge density wave a hexagonal 3×3 reconstruction is formed on the (0001) surface of $NbSe_2$. Below the image a line section that was taken along the white line of the STM image is shown. One can clearly observe the modulation of the corrugation along the atomic rows. (b) In comparison the same sample system measured with an extremely stable STM at 240 mK shows the CDW as a modulation along the atomic rows. Data shown in (b) are taken from Ref. [58].

covalent bonding in two-dimensional layers. The preparation of a clean surface is performed similar to the preparation of HOPG by cleaving the sample *in situ* with a adhesive tape. The tape is glued with one end to the topmost layers of the sample and with the other end to the chamber. By moving the sample the topmost layers stick to the scotch tape and a clean (0001) surface is created on the $NbSe_2$ sample.

A $NbSe_2$ sample was prepared and transferred into the VT-STM held nominally at 21 K. The result of the measurement obtained with a tungsten tip is shown in Fig. 3.12(a). The atomically resolved image shows the hexagonal ordered $NbSe_2$ surface. Moreover, a (3×3) structure (marked by the white hexagon in Fig. 3.12(a)) is superposed to the atomic corrugation as expected for a CDW below 33 K [58]. A direct comparison is given by a data set obtained by S. H. Pan *et al.* shown in Fig. 3.12(b). This measurement was performed with a very stable instrument at 240 mK and our result is in good agreement with this data. The upper limit for the temperature of our experiment is given by T_{C} of the CDW of 33 K. Since the temperature sensor showed a temperature of 21 K the maximal uncertainty of the temperature measurement is about 12 K. The test measurement has shown that the sample holder has a adequate thermal contact to the holder and the temperature of the STM-body indeed represents the sample temperature.

Dy/W(110)

A further test measurement was performed on thin dysprosium films grown on the W(110) surface. The rare-earth (RE) elements are characterized by a successive filling of their $4f$-shell from lanthanum to ytterbium and are prototypical materials with local magnetic moments. Bulk Dy has two magnetic phase transitions: at the Néel temperature of $T_{\mathrm{N}} = 178.5$ K the paramagnetic material becomes helical antiferromagnetic and ferromagnetic below the Curie temperature $T_{\mathrm{C}} = 85$ K. Like most of the RE elements Dy has a hexagonal structure and forms an (0001)-oriented surface on W(110) after deposition by MBE and subsequent annealing. The RE(0001) surfaces exhibit a strongly localized d_{z^2}-like surface state that is exchange-split below T_{C} [cf. Ref. [59]]. Dy/W(110) is an ideal system to test the performance in the spectroscopy mode at low temperatures.

Fig. 3.13(a) shows $\mathrm{d}I/\mathrm{d}U$ curves measured on a thin Dy film with a thickness of about 30 ML at three temperatures: 25 K, 35 K and 60 K. The spectra show two maxima of the differential conductance, one at 100 meV below the Fermi level corresponding to the majority spin band of the d_{z^2}-like surface state and the second at 380 meV above the Fermi level. The maxima are well-pronounced and show up as sharp peaks of the $\mathrm{d}I/\mathrm{d}U$ signal. As expected from the Stoner model [60, 61] the exchange splitting Δ_{ex} (defined as the energetic difference between majority and minority spin bands) decreases with increasing temperature. For comparison similar measurements on Dy/W(110) obtaine at 10 K d by D. Wegner [62] are shown in Fig. 3.13(b). Both measurements show a similar shape but our spectra have larger peak widths due to the higher measurement temperatures [cf. Sec. 2.5]. Furthermore, the exchange-splitting Δ_{ex} of the surface state slightly decreases from about 500 meV at 25 K to about 470 meV at 60 K. This measurement demonstrates that the STM performs adequate local spectroscopy measurements at variable temperatures.

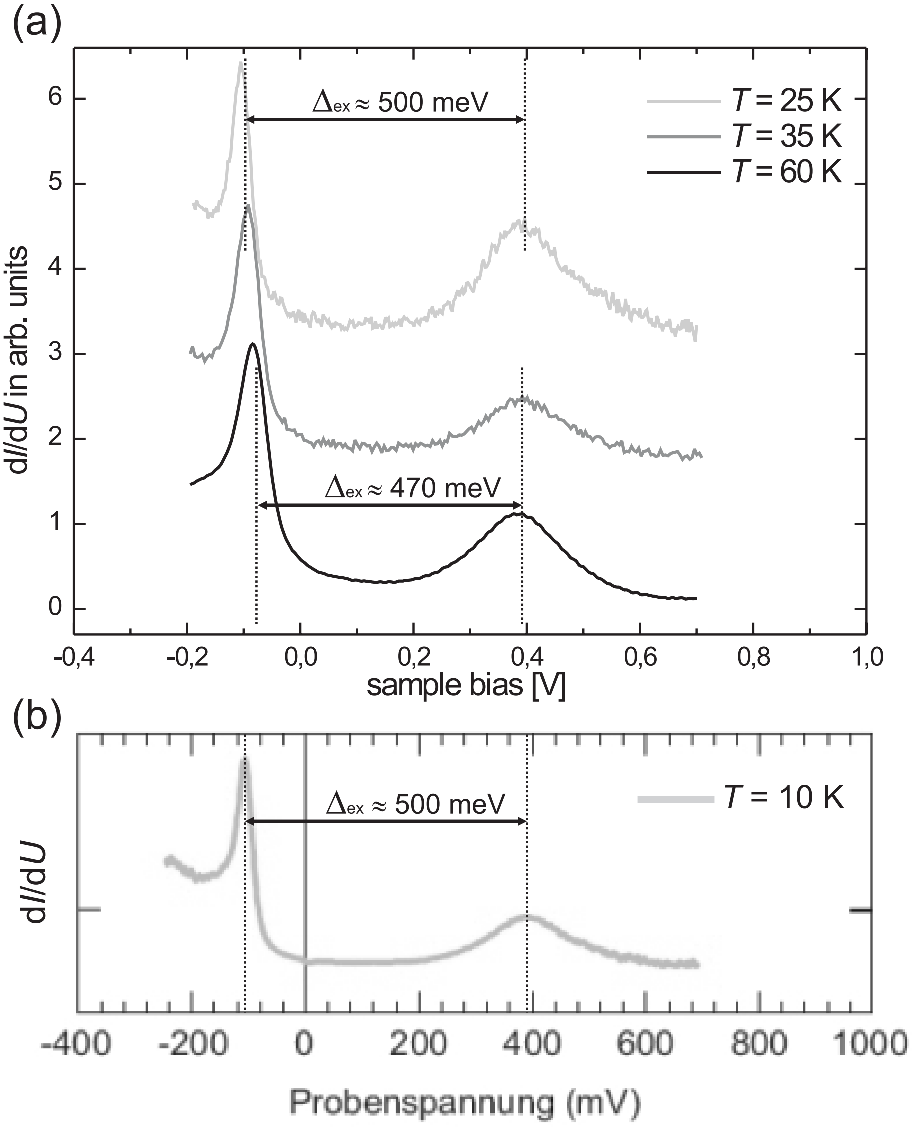

Figure 3.13: (a) dI/dU spectra obtained on Dy/W(110) at a temperature of $T = 25$ K, $T = 35$ K and $T = 60$ K. The spectra were measured with $U_{\mathrm{stab}} = 0.25$ V, $I_{\mathrm{stab}} = 0.5$ nA and a modulation voltage of $U_{\mathrm{mod}} = 10$ mV. An offset was added to the curves of 25 K and 35 K for more clarity. The majority and minority parts of the d_{z^2}-like surface state are measured as narrow peaks of the dI/dU signal below, respectively above, the Fermi level. For comparison the obtained spectra the results obtained by D. Wegner [58] are shown in (b). Here the modulation voltage was $U_{\mathrm{mod}} \leq 1$ mV.

3.8 Summary

The new instrument allows STM measurements under UHV conditions in the temperature range of 20-300 K. The cool-down from room temperature to the smallest accessible temperature of $T = 20$ K can be performed within 2-4 hours. The implementation of the thermal anchoring to the cryostat and decoupling of the STM from components at RT provides adequate cooling of the entire microscope. A tip exchange mechanism gives the ability to prepare magnetically coated tips for spin-polarized STM measurements. By performing test measurements on well known samples it has been shown that the compact design of the instrument enables to acquire STM images with a high lateral resolution over the entire temperature range. Spectroscopy test measurements were performed at low temperatures that demonstrate the good mechanical stability and high energy resolution of the instrument.

Chapter 4

Instrumental setup

Scanning tunneling microscopy (STM) measurements of nanostructures on single crystal substrates aim at the investigation of fundamental questions concerning structural, electronic and magnetic properties. It has to be guaranteed that well-defined samples can be prepared reproducibly. For this reason experiments are performed in ultra high vacuum (UHV) which allows the preparation of clean samples and reduces subsequent contamination.

In this chapter the instrumental setup of the UHV system is described (Sec. 4.1). Finally the experimental procedure to prepare samples and tips is commented on (Sec. 4.2).

4.1 The UHV system

The experiments were performed in a commercial UHV system (Omicron [63]) shown in Fig. 4.1. It consists of two different chambers, the preparation chamber and the analysis chamber, which are connected by a linear manipulator. Both chambers are equipped with an ion getter and titanium sublimation pump ensuring a base pressure in both chambers of $p < 1 \cdot 10^{-10}$ mbar. The preparation chamber is connected to a fast-entry lock that allows sample transfer into the UHV system without breaking the vacuum. The fast entry lock includes a separate sample station for dosing with H_2S gas without contamination of the UHV system. Special sample holders allow the transfer of samples and tips between the different chambers.

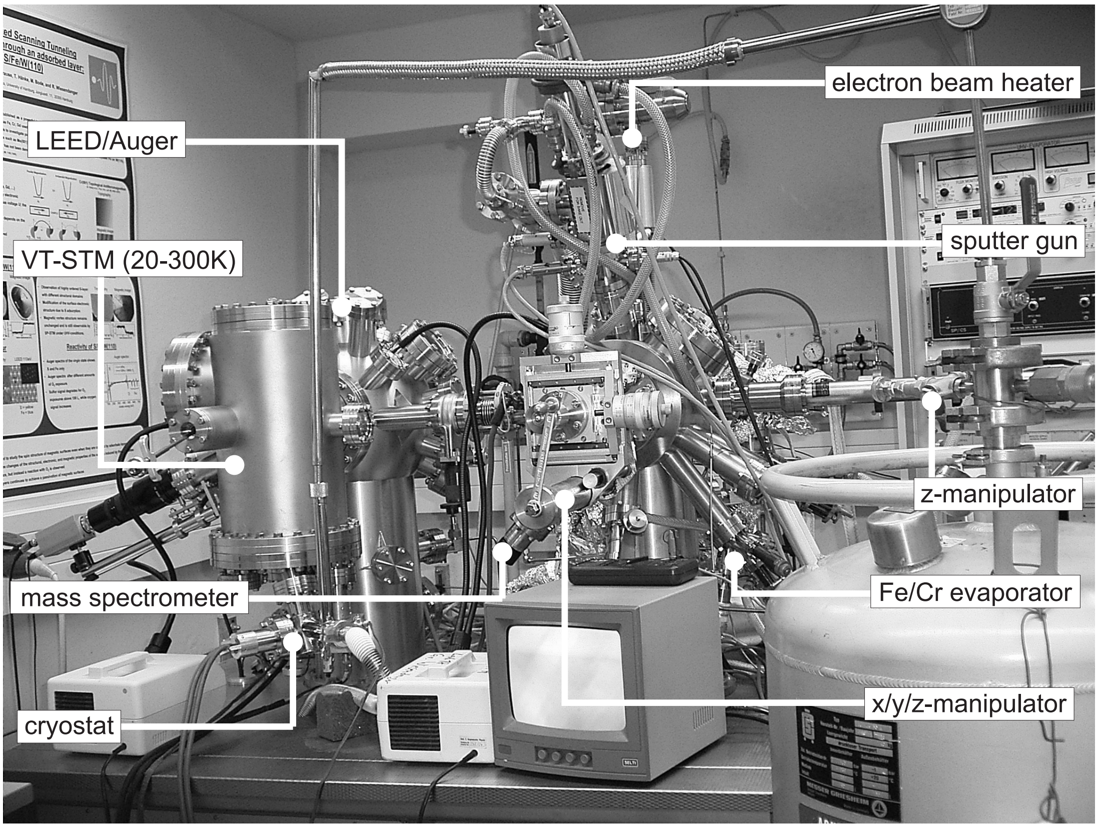

Figure 4.1: Photography of the UHV-system. One the right the preparation chamber with its sample preparation facilities is shown. The right part pictures the analysis chamber and the STM satellite chamber.

4.1.1 Preparation chamber

The preparation chamber is equipped with an (x, y, z)-manipulator with an integrated resistive heater which allows the positioning of the sample in front of the sample treatment facilities. The heater allows a maximum temperature of $T = 1150$ K which is measured indirectly by a chromel/alumel thermocouple. For a direct temperature measurement an optical pyrometer suitable for sample temperatures above $T = 850$ K was used.

A sputter gun with an integrated mass filter (Wien filter) is mounted for cleaning sample surfaces. Here a plasma of the noble gas Ar is produced by electron bombardment in a small ionization volume. The Ar^{+}-ions are accelerated by an electric field of $\sim$1 keV towards the sample where they erode atoms from the surface. A additional Wien filter removes all other than Ar atoms from the ion beam so that a contamination by the sputter gun is excluded. The sputter rate

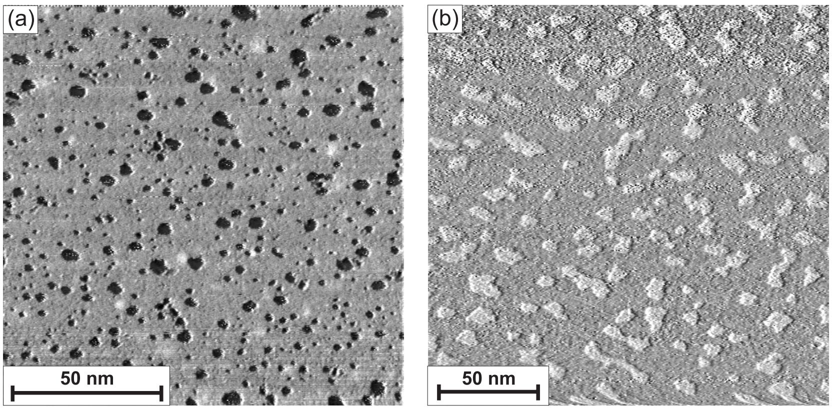

Figure 4.2: (a) STM image of the Cr(001) surface after sputtering for 4 min at RT and annealing at $T = 250$ °C. By determining the coverage of the holes (negative islands) a sputter rate of 2.25 ML/h was estimated. (b) Topography of a Fe/Cr(001) sample used to calibrate the evaporation rate of the Fe evaporator. Fe was evaporated for 20 s and the sample was annealed for 4 min at $T = 300$ °C afterwards. The coverage of 32% leads to an evaporation rate of 0.96 ML/min.

can be measured indirectly by the sputter current. The calibration of the sputter rate is performed by STM. After a short period of Ar^+-ion etching the sample was annealed at $T = 250$ K which is about one third of the melting temperature T_m of Cr. For most materials short annealing at this temperature leads to the formation of vacancy islands. An STM image of the Cr(001) surface after such a preparation is shown in Fig. 4.2(a).

The preparation of magnetic tips was achieved by coating W-tips with thin magnetic films using molecular beam epitaxy (MBE). Two evaporation sources, namely Fe and Cr, were available where Fe was evaporated from a rod and Cr out of a crucible. The target is heated by electrons which are emitted from a filament and accelerated by a high voltage of $U_\mathrm{HV} = 700$–900 V towards the sample. To inhibit heating of the environment the target and the filament are surrounded by a water-cooled Cu-shield. The high voltage U_HV and the filament current I_fil are used to regulate the evaporation rate in order to keep it constant. At constant particle flow evaporated from the target the amount of evaporated material is only varied by the evaporation time. The calibration of the evaporation rate was carried out in a similar way to the calibration of the sputter rate. After deposition at constant particle flow an STM image of the sample was recorded. The evaporation rate is the quotient of the island coverage and the evaporation time (s. Fig. 4.2(b)).

A mass spectrometer, an O_2 leak valve and an electron beam heater are installed in the preparation chamber. The latter allows heating of the sample up to temperatures of 2300 K and is needed for both tip preparation and the preparation of W(110) surfaces.

4.1.2 Analysis chamber

The analysis-chamber (see Fig. 4.1) holds standard surface characterization methods to gain insight into surface properties of samples. The main instrument for surface analysis is the home built VT-STM described in Sec. 3 that is located in a satellite chamber of the analysis chamber. The tip and the sample can be changed *in situ* without breaking the UHV. The periodicity of a surface and an estimate of the quality of its structure can be determined by low energy electron diffraction (LEED). Auger electron spectroscopy (AES) is an element specific method and allows a quantitative measure of the components at the surface.

4.2 Preparation

In this thesis the results of investigations of the temperature dependent electronic and magnetic structure of the Cr(001) surface are presented. Measurements were performed with non-magnetic tips for spin-integrated measurements as well as magnetic tips for spin-polarized measurements. In this section a detailed report on sample preparation procedures is given followed by a description of the tip preparation.

4.2.1 Sample preparation

All experiments were performed using the same (001)-oriented disk-shaped Cr single crystal which has a diameter of about 10 mm and 0.8 mm thickness. It is rigidly mounted with a tantalum frame spot-welded on top of the tungsten sample holder.

The preparation of a clean surface is a crucial point to perform experiments on the Cr(001) surface because the bulk Cr crystal contains contaminants (typical S, N, O and C) that have high tendency to segregate to the surface [64]. The segregation of impurities towards the surface has a specific temperature dependence for each element. Heating a clean Cr(001) surface for some minutes at elevated temperatures leads to segregation and contamination of the surface. Fig. 4.3 shows the Auger signal relative to the Cr main-peak at 529 eV of each element after heat-

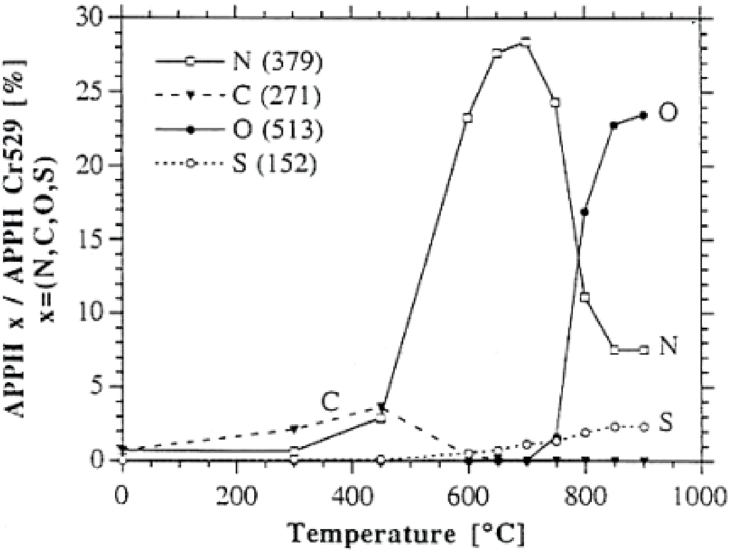

Figure 4.3: Segregation of impurities towards the Cr(001) surface. It shows the Auger signal of an element relative to the Cr signal after heating the sample for some minutes at the corresponding temperature (taken from Ref. [64]).

ing for one minute. It shows clearly the element-specific temperature dependence, for example Nitrogen has a maximal segregation at ∼700 °C. After introducing the Cr crystal into the UHV-system the crystal was cleaned by Ar^+-ion etching for several hours at RT to reduce the amount of oxygen at the surface. This was done until the oxygen concentration cannot be further reduced. To remove the residual impurities the Cr crystal was cleaned by prolonged cycles of Ar^+-ion etching at elevated temperatures (700 K, 900 K and 1100 K), with respect to the maximal segregation rates of C, N and O. Compared to early experiments[65] the amount of residual impurities could be reduced significantly by using an Ar^+-ion gun with a mass filter (Wien filter). Ar^+-ion etching leads to the formation of a depletion zone in the surface region. Finally the Cr crystal is annealed for 20-30 min at $T = 1150$ K to heal the surface and flush out implanted Ar atoms. The resulting sample quality was inspected by AES-, LEED- and STS-measurements. Fig. 4.4 shows the results of each method. The AES measurements (a) show a residual contamination of mainly carbon (relative amount of ∼7 %, while the O- and N-signal is below the Auger sensitivity of 1%. The LEED image (inset of Fig. 4.4(a)) shows clearly the reflections of the unreconstructed Cr(001) surface. A carbon contamination would lead to a c(2 × 2) reconstruction which would show up as spots in between the main Cr(001) spots. The absence of these spots is an

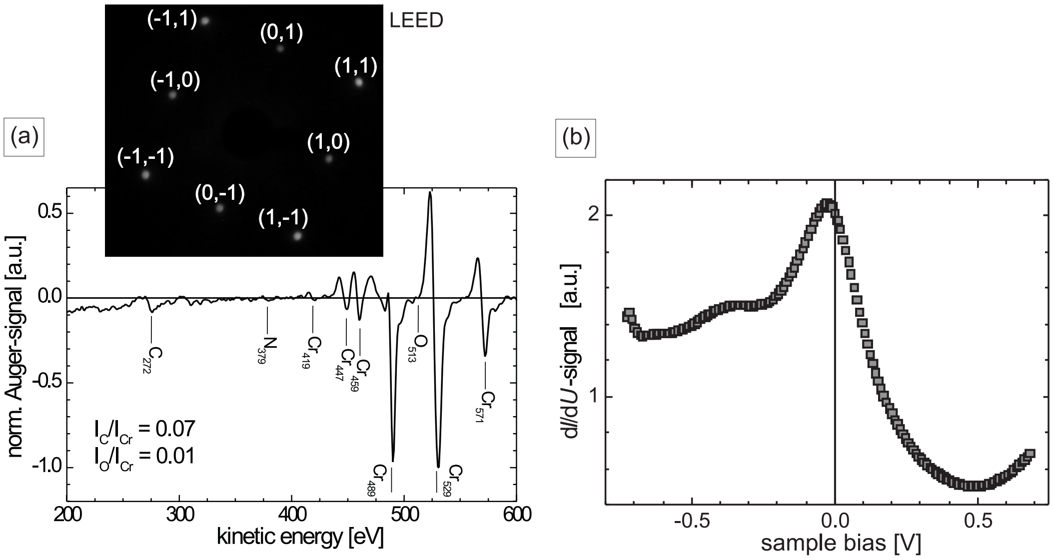

Figure 4.4: Analysis of the Cr(001) surface after cleaning by Ar$^+$-ion etching. (a) The Auger spectrum shows the residual-contamination of the Cr sample: While the N-, O- and S-concentration is below the AES sensitivity, the concentration of C is estimated to 7%. The LEED image was taken at an electron energy of 150 eV and shows spots of four-fold symmetry. (b) The STS dI/dU spectrum at RT shows clearly a peak close to the Fermi energy typical for clean bcc-surfaces [66, 67].

indication of a relatively clean surface. Fig.4.4(b) shows a STS spectrum taken at RT with the typical spectral feature close to the Fermi level [66, 67]. This peak is known to be suppressed and shifted by contaminations of higher concentration, for example by C, N and O. In conclusion, the Cr(001) could be cleaned except for a rather small amount of residual impurities. This allowed spin-resolved STS measurements for a time period of several hours.

4.2.2 Tip preparation

In STM/STS the preparation of well defined and stable tips is of great importance. Here tips made of poly-crystalline W wire (diameter $D = 0.8$ mm) which was etched electrochemically in sodium hydroxide solution (2M NaOH) were used. Fig. 4.5(a) shows a microscopic image of such an etched tip (taken from Ref. [14]). The radius is typically $D = 30-90$ nm. After cleaning the tip with distilled water and fixing it in the holder it was inserted into the vacuum chamber by a tip-shuttle (cf. Sec. 3.4). For spin-averaged measurements it is only necessary to clean the tips. To remove the oxide film covering the tungsten tip, it was heated for a short

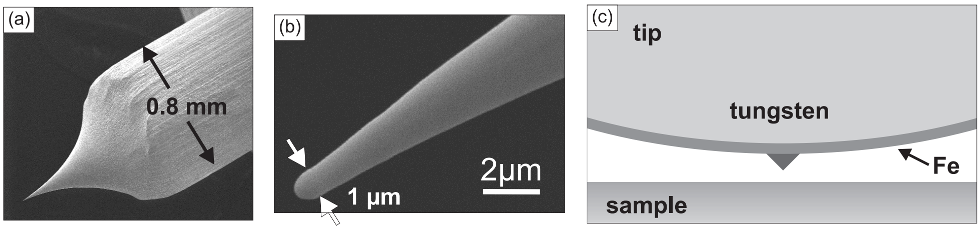

Figure 4.5: SEM-micrographs of an electrochemically etched, polycrystalline W tip after a high temperature flash at $T > 2200$ K [68]. (a) The overview shows the shaft of the tip with a diameter of 0.8 mm. (b) High-resolution SEM image of the very end of the tip. The tip apex has a diameter of approximately 1 μm. (c) Schematic representation of the tip apex (in scale). The magnetic film is very thin compared to the curvature of the tip. Probably, a small magnetic cluster protrudes from the tip, which is responsible for the lateral resolution of SP-STM (taken from Ref. [14]).

time (flashing) up to $T \geq 2000$ K. Since the shuttle and the tip-holder were made of appropriate materials (tungsten, molybdenum) this was done by putting the shuttle onto the electron beam heater. The heating process causes a melting of the tip apex leading to tip radius of $D = 500$ nm. Fig. 4.5(b) shows a scanning electron microscope (SEM) image of the tip apex after flashing at $T \geq 2000$ K. These rather blunt tips are not suitable for surfaces with high corrugation but are useful as SP-STS tips. Probably during recrystallization the tip gets a well-ordered and clean surface with an (110) orientation [14] that is needed for later coating with magnetic thin films.

For spin-polarized measurements the final step is the magnetic coating of the tip. The tip was coated with thin magnetic films of several monolayers followed by annealing at 550 K for 4 min to achieve a well ordered film at the tip apex. The conceptional idea behind this preparation method is the following: First of all a high spin-polarization at the tip apex is required in order to achieve a high signal to noise ratio. Therefore, a clean environment is required. Second dipolar interaction between tip and sample due to the stray field of the tip should be as small as possible. By using thin film tips the amount of magnetic material is kept as small as possible thus resulting in low stray fields. Third tips with magnetic sensitivity either to the in-plane or out-of-plane component of the sample magnetization should be available. In contrast to bulk tips, where the magnetization direction is governed by the shape anisotropy, additional surface- and interface anisotropy is responsible for the magnetization direction in thin films. Due to the rather large curvature of the tip compared to the film thickness (s. Fig. 4.5(c)) the effective

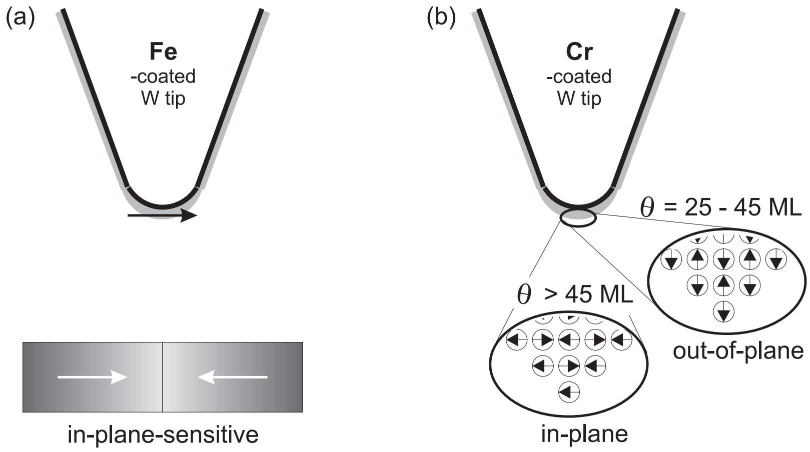

Figure 4.6: Magnetic sensitivity of W tips coated with different magnetic material. (a) Fe-coated tips are sensitive to the in-plane component of surface magnetization; (b) Cr-coated tips show a reorientation transition of the magnetic anisotropy from in-plane to out-of-plane with decreasing film thickness.

surface and interface anisotropy can be deduced from an equivalent film on a flat W(110) substrate. By choosing appropriate film materials one can thus tune the magnetization orientation of the tip. Since the microscope used in this work operates at variable temperatures the temperature of the tip plays an important role because of reorientation transitions and the Curie- or Néel-temperatures of the magnetic thin films. While working at low temperatures ($T < 100$ K) thin Fe films covering the W tip are ferromagnetic and are sensitive to a sample magnetization parallel to the surface plane [68, 69]. Good results were achieved after deposition of an amount of Fe equivalent to a coverage of $\theta \approx 6-10$ ML. Antiferromagnetic Cr thin films on W tips also provide magnetic sensitivity [25]. This results from the dominating contribution to the tunnel current of the outermost atom. Its magnetic orientation is of course also fixed in an antiferromagnet. For Cr-coated W tips the magnetic sensitivity is normal to the sample surface plane at low coverage ($\theta = 25 - 45$ ML) and changes to parallel for higher coverage ($\theta > 45$ ML). The magnetic sensitivity of tips covered with different magnetic materials under these conditions is shown in Fig. 4.6.

For higher temperatures up to RT more material is necessary to ensure ferro- or antiferromagnetic order. Even though ferromagnetism has been reported for a double-layer of iron above RT [70] a much higher coverage of Fe ($\theta = 15 - 50$ ML) was necessary to obtain magnetic sensitivity to the in-plane component of the sample.

Chapter 5

Temperature-dependent study of the Cr(001) surface

The following chapter reports on a combined temperature-dependent investigation of the Cr bulk SDW by neutron scattering and of the Cr(001) surface by SP-STS performed on the same Cr single crystal. The neutron scattering experiments confirm that—in spite of some mechanical strain caused by the clamping of the crystal onto the sample holder—the incommensurable SDW dominates the bulk magnetic structure and that the spin-flip transition occurs at the expected temperature $T_{\mathrm{SF}} = 123$ K. In contrast, no transition is observed on the surface but topological antiferromagnetic order with the magnetization lying in the surface plane is found by SP-STS within the entire studied temperature range of 23 K $\leq T \leq$ 293 K. After describing the characterization of the magnetic bulk properties of our Cr(001) single crystal in Sec. 5.2 by neutron-scattering, I will present temperature-dependent SP-STS measurements of Cr(001) in Sec 5.3. At first SP-STS measurements of the “topological antiferromagnetism” as found on clean Cr(001) surfaces above T_{SF} are presented. Then the temperature-dependent magnetic structure of the Cr(001) surface is studied by SP-STS between room temperature and $T = 23$ K. Finally, in Sec. 5.3.3 we discuss the results and compare them to measurements obtained for epitaxially grown Cr(001) films.

5.1 Introduction

Since the discovery of an incommensurate spin density wave (I-SDW) in 1959 [71], the complex magnetic structure of Cr has been of continuing interest. As the SDW in bulk chromium has been studied intensively it is generally accepted as a typical example of how the electronic structure and the topology of the Fermi surface may influence magnetism in itinerant systems. Attention was recently drawn to the magnetic properties of Cr at reduced dimensionality because of its role in exchange-coupled Fe/Cr bilayers and superlattices [72, 73]. These systems feature interesting magnetic effects such as giant magneto-resistance [5, 6]. Proximity effects of Cr with ferromagnetic layers, thin Cr films, and the Cr surface itself were intensively studied.[74] As the physical properties of Cr exhibit quite complex phenomena we refer to the comprehensive review article by Fawcett in Ref. [75].

5.1.1 Chromium — an antiferromagnet

Since its discovery in 1797 by Louis-Nicholas Vauquelin chromium was in the focus of various research activities mainly because of its magnetic properties and gave several challenges to be solved. In 1932 Néel [76] already demonstrated that the paramagnetic susceptibility of a diluted solution of Cr in Au follows the Curie-Weiss law. This was surprising since chromium shows, unlike the three ferromagnetic elements Fe, Co and Ni, no net magnetization. Néel explained the paramagnetic behavior by a antiferromagnetic ordering in bulk Chromium [77]. Spin-polarized neutron scattering experiment by Shull und Wilkinson [78] in 1959 provided direct evidence of antiferromagnetic ordering. Chromium ((001) orientation) and manganese were the only candidates of a long list of examined materials (W, Mo, Nb, V, Cr, Mn, Fe) that exhibited antiferromagnetic ordering.

Bykov *et al.* [79] and Corliss *et al.* [71] found independently magnetic satellite reflections at the $(0, 0, 1 \pm \delta)$ position with neutron scattering experiments. This result led to speculations about an anti-phase-domain structure in chromium with a rotation of 180° of the local spin every 14 unit cells. Hastings [80] showed with similar neutron scattering experiments that these reflections are caused by a sinusoidal modulation of the scattering amplitude. Furthermore, he found a change in the intensity of the satellite reflections at ≈100 K and assigned it to a reorientation of the phase polarization from a transversal phase at high temperatures (spin $\vec{S}$ perpendicular to the wave vector $\vec{Q}$) to a longitudinal phase at low temperatures ($\vec{S} \parallel \vec{Q}$). Shirane *et al.* [81] proved that the sinusoidal modulation is evoked by a static spin density wave (SDW) whose wavelength changes continuously from 42 unit cells at $T = 78$ K to 54 unit cells at $T = 311$ K.

5.1.2 Magnetic properties of bulk Cr: spin density wave

Chromium has a bcc structure with a lattice parameter of $a_{\mathrm{Cr}} = 2.884$ Å in the paramagnetic state. Cr is a $3d$ transition metal and has to be considered as an itinerant antiferromagnet with a Néel transition temperature $T_{\mathrm{N}} = 311$ K in the

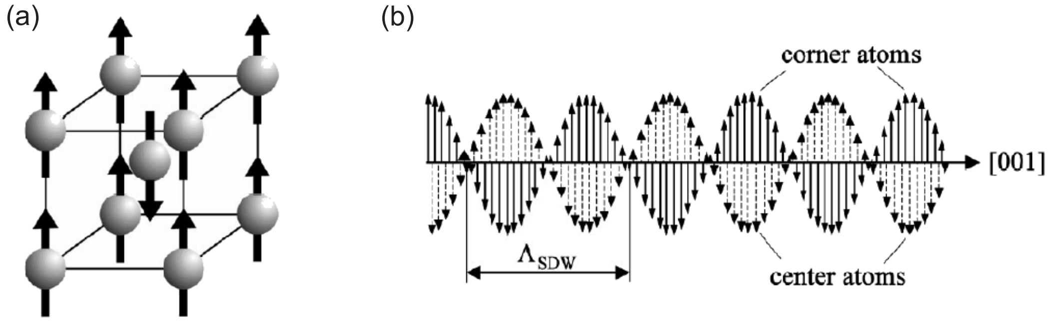

Figure 5.1: Commensurate and incommensurate spin-density wave (I-SDW) in Chromium. (a) The antiferromagnetic orientation of the magnetic moments of the corner atoms to the center atoms leads to a commensurate SDW. (b) Actually an incommensurate SDW is formed. Here the case of a transversal SDW is schematically shown with a wave vector along the [001]-direction [74].

bulk. The magnetic moment of the corner atoms exhibits an antiparallel orientation relative to the magnetic moment of the center atoms. This configuration can be described by a commensurate spin density wave along one of the $\langle 001 \rangle$-directions with a period of the lattice constant a_{Cr} (cf. Fig. 5.1). This model of a commensurate antiferromagnetic ordering does not apply to chromium, which has an incommensurate SDW characterizes the bulk ground state (cf. Fig. 5.1(b)).

Overhauser [82, 83] first pointed out that the Hartree-Fock ground state of an electron gas with exchange interaction and Coulomb interaction is not represented by paramagnetic nor ferromagnetic ordering but the formation of a static spin density wave. The most simple model introduced by Overhauser was a one-dimensional electron gas where three-dimensional spins interact via a repulsive potential $V_{ij} = \gamma\,\delta(z_i - z_j)$. In this model the solution for a self-consistent Hartree-Fock potential $U(z)$ is given by:

$$U(z) = 2g\,E_\mathrm{F}\,(\sigma_x \cos(Qz) + \sigma_y \sin(Qz))\,. \tag{5.1}$$

Here E_F is the Fermi energy and σ_x,σ_y are the Pauli matrices. The factor g is a coefficient that depends on the wave vector $\vec{Q}$ of the SDW. This potential has the property that its only non-zero matrix elements are between free-electron spin-up $(\vec{k},\uparrow)$ and spin-down $(\vec{k}+Q,\downarrow)$ states, thus producing energy gaps in the original free-electron spectrum on one side of $\vec{k}=0$ shown in 5.2. In the resulting band structure states are filled up to the minima of the lower bands for the ground state of the SDW. Thermal excitation leads to an occupation of the upper band and thus to a decrease of the SDW amplitude. This simple consideration shows how spin-up and spin-down particles separated in the reciprocal space by the wave vector $\vec{Q}$ interact with each other and form a spin density wave.

Band structure calculations [84–86] show that the electron and hole Fermi surfaces at the Γ and H points of the reciprocal bcc lattice have a nearly octahedral shape as shown in Fig. 5.3. Electron and hole states at the Fermi surface nest each other due to the same shape of the Fermi surfaces and are connected by a constant vector $\vec{Q}$ in the reciprocal space. The wave vector $\vec{Q} \simeq 2\vec{k}_\mathrm{F}$ ($\vec{k}_\mathrm{F}$: Fermi wave vector) is the so-called nesting vector. This implies that $\vec{Q}$ couples Bloch states of the electron band to Bloch states of the hole band such that the occupied states are lowered and the unoccupied states are lifted in energy. This effect lowers the density of states at the Fermi level and stabilizes the SDW along the Γ-H-, the [001]-direction in Cr. Since the hole Fermi surface is slightly larger than the electron Fermi surface, the vector $\vec{Q}$ for the SDW is incommensurate.

The spin density wave in Cr is connected with a charge density wave (CDW) as well as with a strain wave (SW) that both have half the period of the SDW. Due to magnetostriction induced by spin-orbit-coupling the crystal symmetry is modified by the SDW: While the paramagnetic phase in Cr has a cubic symmetry, the antiferromagnetic phase AF_1 exhibits a orthorhombic crystal structure. In the AF_1 the long axis decreases continuously while the temperature is decreased from $T_\mathrm{N} = 311$ K to the spin-flip temperature T_SF. The first order phase transition at $T_\mathrm{SF} = 123$ K is characterized by a change of the crystal symmetry from orthorhombic to tetragonal and a simultaneous reorientation of the magnetic moments of the SDW.

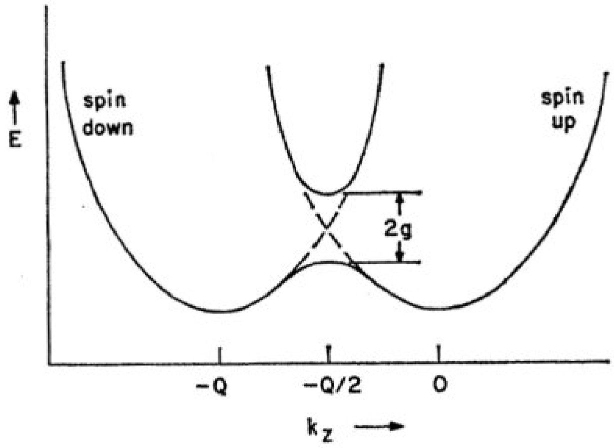

Figure 5.2: Energy dispersion of two particles (spin-up on the left and spin-down on the right) interacting via Coulomb and exchange interaction. The energy gap is formed at $k_z = -Q/2$ (taken from Ref. [83]).

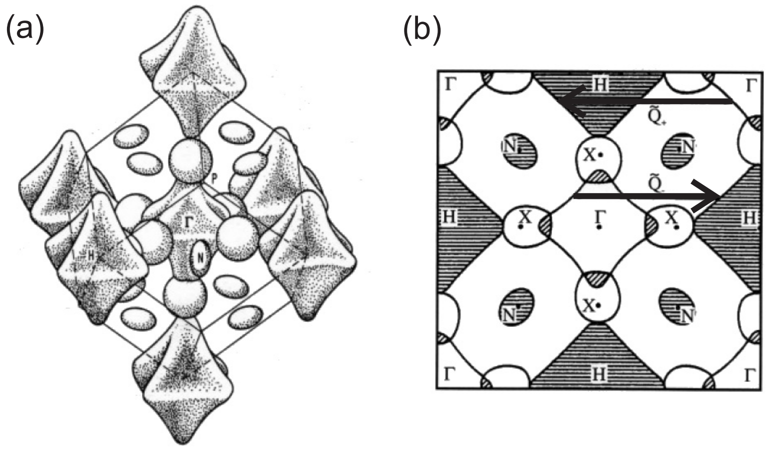

Figure 5.3: Fermi surfaces based on band structure calculations by Laurent *et al.* [86]. (a) three dimensional Fermi surfaces. (b) projection to the (001) plane. The Fermi surface of the electrons has its center at the Γ point while the Fermi surface of the holes is concentrated around the H point. The vectors $\vec{Q}_+$ and $\vec{Q}_-$ shown by the arrows in (b) illustrate the nesting vector of the Fermi surfaces of the electron and hole states (taken from Ref. [74]).

5.1.3 Magnetic properties of the Cr(001) surface

In the following the magnetic structure of the Cr(001) surface will be discussed. As mentioned before pure Cr exhibits an incommensurate spin density wave which originates from the nesting of the Fermi surface. It consists of a static sinusoidal modulation of the magnetic moments with a period L between 27 a_{Cr} ($\approx$ 7.8 nm) at room temperature and 21 a_{Cr} ($\approx$ 6.1 nm) at 10 K. Two different modifications exist, i.e., the transverse (T) and the longitudinal (L) SDW below the Néel temperature $T_{\mathrm{N}} = 311$ K and the spin-flip temperature $T_{\mathrm{SF}} = 123$ K, respectively. The T-SDW has a magnetic moment $\vec{\mu}$ perpendicular to the propagation direction $\vec{Q}$ of the SDW ($\vec{\mu} \perp \vec{Q}$), the longitudinal SDW exhibits a parallel configuration ($\vec{\mu} \parallel \vec{Q}$). For both SDW types the propagation vector $\vec{Q}$ points along one of the three possible $\langle 100 \rangle$-directions. Since all three $\langle 100 \rangle$-directions are equivalent within the crystal bulk they coexist with equal probabilities. Magnetic phase transitions are accompanied with a change of the crystal symmetry due to spin–orbit-induced magneto-elastic interactions. The paramagnetic bcc structure transforms into an orthorhombic crystal symmetry below T_{N} and a tetragonal symmetry is found for the L-SDW.

This situation may change completely if the symmetry is reduced at a surface or interface. In spite of its antiferromagnetic bulk structure, ferromagnetic order and an increased magnetic moment have been predicted for a perfect Cr(001) surface without any steps [87, 88]. Fu and Freeman [88] showed by ab initio full-potential linearized augmented plane wave (FLAPW) calculations that the enhanced magnetic moment at the surface is due to a sharp spin-split surface state at the Fermi level. Early experimental data were rather contradictory. Angle- and energy-resolved photoemission indicated that the Cr surface states are exchange split [89, 90], which is consistent with the theoretical prediction of ferromagnetically ordered terraces, but no net magnetization was found by spin-resolved photoemission [91]. This apparent inconsistency was explained by Blügel *et al.* [32] who calculated that the magnetic moments of any atomically flat terrace couple parallel but—as a result of the antiferromagnetism of Cr—adjacent terraces are magnetized antiparallel. Since this model implies a close link between the surface topology and the magnetic structure the magnetic state of Cr(001) was called "topological antiferromagnetism".

The magnetization direction alternates laterally and vertically with periodicities which are given by the average terrace width and the interlayer distance. Direct experimental proof of topological antiferromagnetism is extremely difficult, because lateral and vertical averaging leads to the cancelation of the spin signal. A suitable experimental method must have a high lateral resolution (better than the average terrace width) and high surface sensitivity to exclusively probe the magnetization of one particular surface layer. Both conditions are fulfilled by spin-polarized scanning tunneling microscopy (SP-STM) and spectroscopy (SP-STS) [8, 65, 68, 92, 93]. Such studies delivered the following picture of the Cr(001) surface magnetic structure at room temperature for $T > T_{\mathrm{SF}}$ [8, 65, 92, 93]: the magnetic structure of the perfect Cr(001) surface is adequately described by the model of the topological antiferromagnetism. A direct comparison of magnetically in-plane sensitive differential conductance $\mathrm{d}I/\mathrm{d}U$ maps with simultaneously measured topographic STM images revealed that the $\mathrm{d}I/\mathrm{d}U$ signal abruptly changes between two discrete levels whenever a monatomic step edge is crossed. This variation is caused by the fact that adjacent terraces have opposite in-plane magnetization directions. In the SP-STS measurements the spin polarization of the d_{z^2}-like surface state of the bcc surface [66] was utilized to distinguish between the two magnetization directions of adjacent terraces. Fig. 5.4 shows SP-STS spectra taken at RT with a Fe-coated tungsten tip. The magnetic contrast arises due to different intensities of the surface state peaks on adjacent terraces. Moreover, it was found that the magnetization direction of adjacent Cr(001) terraces alternates even over a large number of terraces without any change in the $\mathrm{d}I/\mathrm{d}U$ contrast [92]. This is somewhat surprising as the incommensurate sinusoidal mod-

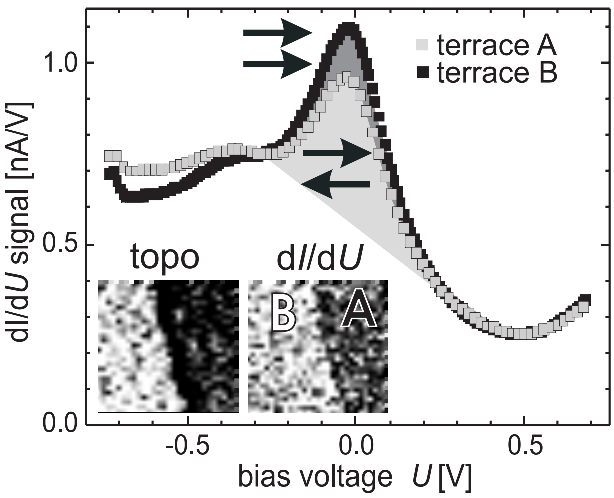

Figure 5.4: SP-STS spectra of the Cr(001) surface taken on two adjacent terraces A and B showing the typical d_{z^2}-like surface state close to the Fermi level. The inset shows the topography (left) and the spin-resolved dI/dU map (right) at the peak position (∼ 20 meV). The terraces both show ferromagnetic ordering but have an opposite magnetization. Due to the different magnetic orientation of tip and sample relative to each other the peak shows different intensities on the two terraces (taken from Ref.[94].

ulation of the SDW may cause phase slips as found previously for Cr wedges on Fe(001) whiskers [95].

Both findings, the in-plane orientation of the magnetization as well as the absence of any phase slip or long wavelength modulation of the surface magnetic moment, strongly reduce the number of possible configurations of the SDW at the Cr(001) surface. Firstly, since the above mentioned measurements were performed at room temperature where the SDW is transverse ($\vec{\mu} \perp \vec{Q}$) and since an in-plane magnetization was found,[92] it can be concluded that the propagation vector $\vec{Q}$ of the SDW is always oriented perpendicular to the surface plane. This so-called single $\vec{Q}$ state in the near-surface region was also found by X-ray scattering [96–98], neutron scattering [97, 98], and perturbed angular correlation spectroscopy studies [99] performed at various Cr(001) layered systems.[1] Furthermore, in order to explain the constant magnitude of the surface magnetic moment the surface SDW cannot be a simple extension of the bulk SDW. Two possible spin configurations are schematically sketched in Fig. 5.5. The first possibility is characterized by a T-SDW which is slightly shifted between adjacent terraces to maximize the magnetic moment for every individual (001) surface layer. This situation is schematically represented in Fig. 5.5(a). A second modification, shown in Fig. 5.5(b), leaves the

---

[1] Note, that the investigated Cr(001) surfaces were not prepared *in situ* but have been exposed to ambient conditions between preparation and analysis. Therefore, the surfaces are certainly oxidized and contaminated.

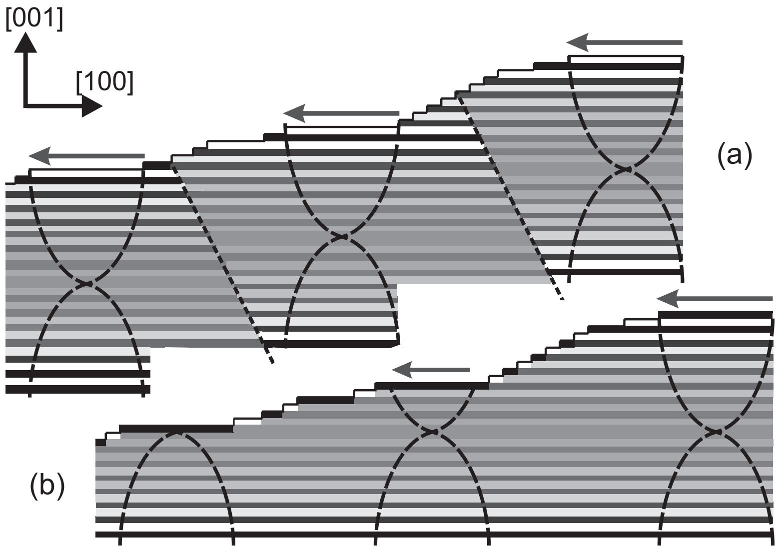

Figure 5.5: Two different models of the Cr T-SDW at the surface. (a) The SDW exhibits a maximal magnetic moment for every individual (001) surface layer. In this case small-angle domain walls must exist oriented perpendicular to the surface. (b) The bulk SDW is perfectly maintained up to the first subsurface layer. Only the coupling between the surface layer and the first subsurface layer is frustrated in order to maximize the magnetic moment at the surface.

bulk SDW unchanged, but the coupling of the Cr(001) surface layer to the first subsurface layer varies such that the surface magnetic moment is maximized for each terrace. In principle, both interpretations are consistent with the theoretical calculation mentioned above which predict an enhanced magnetic moment for the Cr(001) surface.[66] In either case the magnetic frustration certainly leads to an enhanced exchange energy. While in the former model [Fig. 5.5(a)] small-angle domain walls are formed at step edges between two terraces, the latter model implies a frustration of the exchange interaction between the surface and the first subsurface layer. Fig. 5.6(a) shows the typical topography of the clean Cr(001) surface at temperatures between T_{N} and T_{SF} measured at $T = 200$ K. Ten terraces can be recognized which descend from the lower left to the upper right edge of the image. The section in the upper panel of Fig. 5.6(c) has been drawn along the surface region indicated by the black box in Fig. 5.6(a). It reveals that adjacent terraces are separated by monatomic steps of 1.44 ± 0.08 Å height. This terrace-and-step structure which is found on any real surface is the result of a slight miscut (locally about 0.04°, averaged over the whole sample approximately 0.15°) with respect to the ideal (001) surface. Fig. 5.6(b) shows the simultaneously acquired map of the

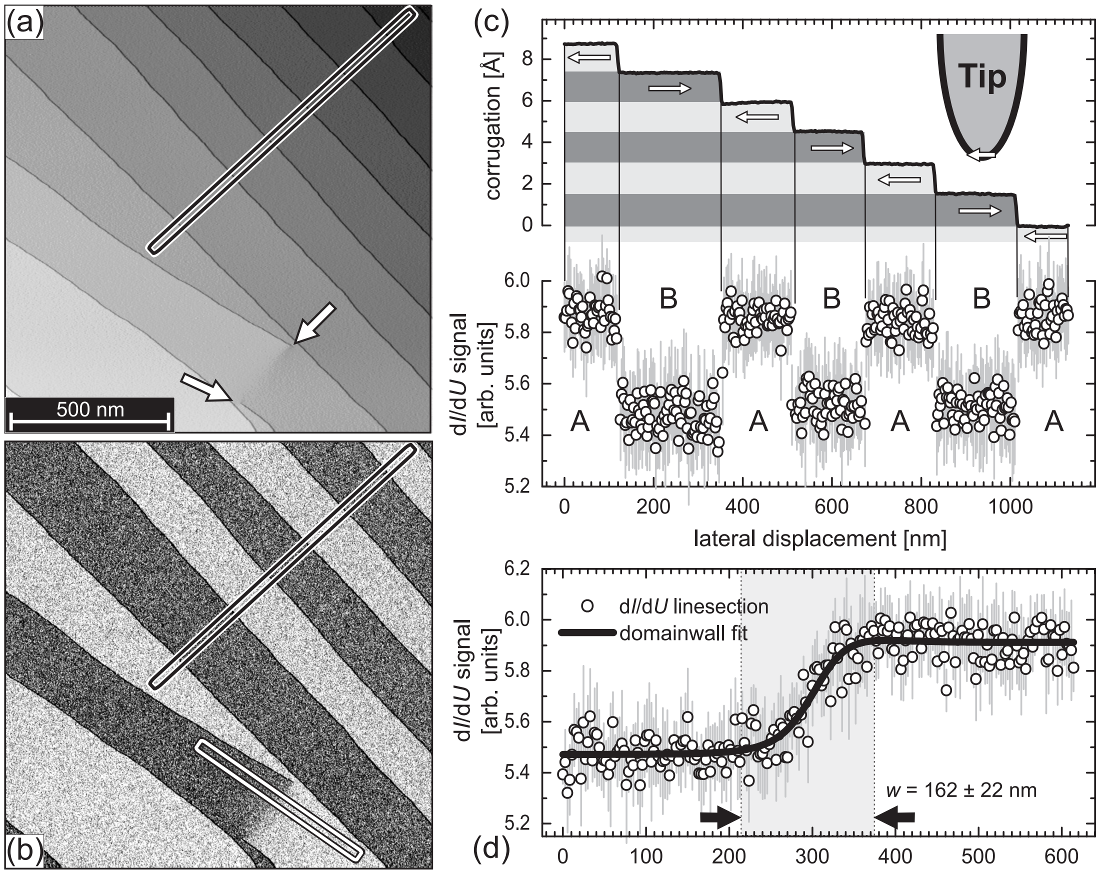

Figure 5.6: The Cr(001) surface. (a) Constant-current STM image of the clean Cr(001) surface showing several terraces separated by monatomic steps. The data were obtained at a temperature of $T = 200$ K with a magnetic Fe-coated probe tip using a tunneling current $I = 0.3$ nA and a sample bias voltage $U = -100$ mV. (b) Spin-polarized spectroscopic image of the dI/dU signal of the same surface region shown in (a). The right panels show averaged sections drawn along the boxes, where (c) corresponds to the line perpendicular to the step edges (black box) and (d) to the one across the domain wall (white box).

differential conductance dI/dU as measured with a magnetically in-plane sensitive Fe-coated tungsten tip. Obviously, the strength of the dI/dU signal abruptly changes between two discrete levels at any step edge as expected for a surface which exhibits topological antiferromagnetism. This signal variation is the result of spin-polarized tunneling between the magnetic sample and the magnetic tip. The section of the dI/dU signal in the lower panel of Fig. 5.6(c) confirms that there are only two levels of the dI/dU signal, denoted A and B. Apart from these step edges two further defects in form of screw dislocations are visible in the lower right part of Fig. 5.6(a) and are marked by arrows. Screw dislocations lead to the formation of semi-infinite step edges which start at the respective point of interception of the dislocation line with the Cr(001) surface plane. Obviously, the Cr(001) surface cannot exhibit perfect topological antiferromagnetic order around a screw dislocation. Instead, a domain wall is formed between the two screw dislocations. A more detailed analysis of domain walls induced by dislocations on the Cr(001) surface can be found in Ref. [93]. To determine the domain wall width we have drawn an average profile of the $\mathrm{d}I/\mathrm{d}U$ signal along the white line section in Fig. 5.6(b). The result is plotted in Fig. 5.6(d). A quantitative analysis is performed on the basis of continuum micro-magnetic theory[100] by fitting the measured data with a standard domain wall profile

$$y(x) = y_0 + y_{\mathrm{sp}} \cdot \cos(\arccos\{\tanh[(x - x_0)/(w/2)]\} + \phi), \tag{5.2}$$

where $y(x)$ is the $\mathrm{d}I/\mathrm{d}U$ signal measured at position x, x_0 is the position of the domain wall, w the domain wall width, and y_0 and y_{sp} are the non–spin-polarized and spin-polarized part of the $\mathrm{d}I/\mathrm{d}U$ signal, respectively. ϕ is the azimuth between the tip and sample magnetization. For this particular domain wall the best fit is achieved with $\phi = 31^\circ$ leading to a width of $w = 162 \pm 10$ nm which is in good agreement with earlier results which showed a domain wall width of 120-170 nm.[65, 93]

5.2 Neutron scattering on bulk chromium

The properties of the Cr SDW are highly sensitive to the sample quality. For example, elastic strain can cause the SDW to change from commensurate to incommensurate yielding qualitatively different neutron scattering spectra. In the case of the Cr crystal examined here mechanical strain may result from the mounting procedure (see Sec. 4.2.1). In particular, locations, where the Cr sample and the tantalum foil touch, are more susceptible to irregularities with crystalline imperfections (ripples) visible to the naked eye.

In order to examine the SDW bulk behavior of the Cr crystal neutron scattering experiments were performed. The experiments were carried out at POLDI, a neutron diffractometer, on a thermal neutron guide at the Geesthacht Neutron Scattering Facility (GENF) at GKSS using monochromatic neutrons with a wavelength of 0.18 nm. Higher harmonics, which would be reflected by POLDI's graphite monochromator potentially causing spurious peaks at the {001} positions, were completely suppressed by the use of a velocity selector. A cryostat

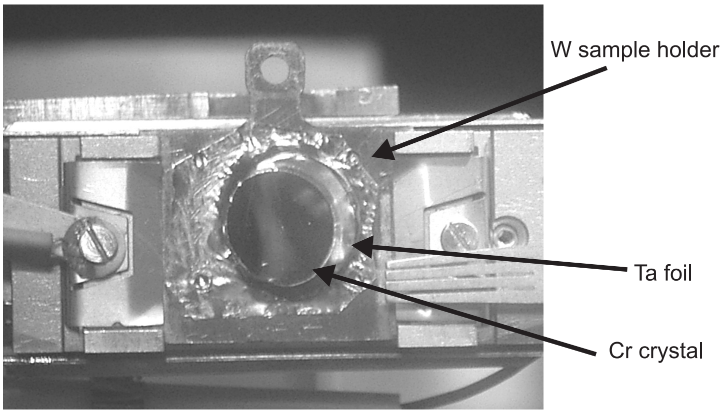

Figure 5.7: Photographic image of the Cr crystal. The Cr crystal is mounted on a tungsten sample holder by a tantalum frame. The crystalline imperfections (ripples) are visible due to locally different reflections of the surface (gray shadow across the crystal surface). The sample holder is clamped on the mounting on the x, y, z-manipulator.

was employed to set the sample temperature within the required range between 13 K and 350 K.

In the past the spin structures and phase transitions of Cr were primarily studied by elastic neutron scattering. It is a well established technique which is used here to complement the SP-STS characterization of our Cr single crystal by probing its SDW bulk behavior. The scattering cross-section of an unpolarized neutron beam with a spin density wave $\vec{M}(\vec{r})$ is given by [75, 101, 102]

$$\frac{\mathrm{d}\sigma}{\mathrm{d}\Omega} = |\vec{M}_q|^2 \sin^2 \Theta_q \cdot \delta(\vec{q} + \vec{q}_\pm - \vec{G}_{\mathrm{bcc}}), \tag{5.3}$$

where Θ_q is the angle between the magnetization $\vec{M}(\vec{r})$ and the scattering vector $\vec{q}$, $\vec{M}_q$ is the Fourier component of $\vec{M}(\vec{r})$ corresponding to the scattering vector $\vec{q} = \vec{k}' - \vec{k}''$, $\vec{q}_\pm = \vec{G}_{\{001\}}(1-\epsilon)$ is the wave vector of the spin density wave with ϵ as a measure of the deviation from the commensurability and $\vec{G}_{\mathrm{bcc}}$ are the reciprocal lattice vectors for the allowed bcc reflections. The δ function in Eq. 5.3 indicates that the intensity from the magnetic scattering is only observed at positions in reciprocal space for which $\vec{q} = \vec{G}_{\mathrm{bcc}} - \vec{q}_\pm$. The existence of incommensurate SDW's (i.e. $\epsilon \neq 0$) results in characteristic satellite peaks in the vicinity of the structurally forbidden bcc reflections. The bottom panel of Fig. 5.8 illustrates possible satellite reflections for neutron scattering in reciprocal space originating from SDW structures in Cr.

Two criteria need to be considered in order to determine the propagation direction and polarization of the SDW in Cr, i.e. $\vec{q}_\pm$ and $\vec{M}_q$. The orientation

SDW-mode	(001) L-satellite	(001) K-satellite	(010) L-satellite	(010) K-satellite
out-of-plane longitudinal spins out-of-plane	○	○	●	○
out-of-plane transversal spins in-plane	●	○	●	○
in-plane longitudinal spins in-planel	○	●	○	○
in-plane transversal spins in-plane	○	●	○	●
in-plane transversal spins out-of-plane	○	○	○	●
positions of the satellite reflections around the [010] and [001] Bragg reflections in the reciprocal space	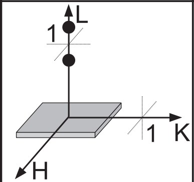	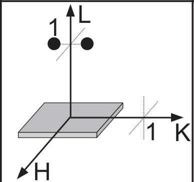	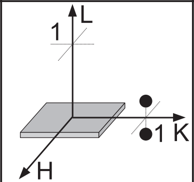	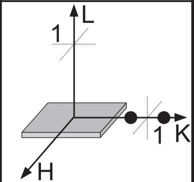

Figure 5.8: How to interpret the neutron scattering experiments: (bottom row) Overview of neutron scattering geometries with satellite reflections as they occur for different longitudinal and transverse incommensurate spin density waves. (top rows) Lookup table with filled and empty circles indicating the presence and absence of satellite reflections for certain spin density waves (adapted from Ref. [98]).

and magnitude of $\vec{q}_{\pm}$ corresponds to the vector between any of the satellite peak positions and the next-nearest allowed bcc reciprocal-lattice point which identifies the propagation direction of the SDW. Second, the magnetic neutron scattering cross section only yields intensity for components of the magnetization vector $\vec{M}_q$ perpendicular to the scattering vector. With several selected scans in orthogonal directions these criteria can be used to determine the nature of the SDW. Fig. 5.8 provides a summary of the conditions for the observation of satellite reflections in various directions due to the selection criteria. The period length Λ_{SDW} of the SDW can be determined from the distance of the satellite position to the next nearest $\vec{G}_{\{001\}}$ position with

$$\Lambda_{\mathrm{SDW}} = \frac{a_{\mathrm{Cr}}}{\epsilon}, \tag{5.4}$$

where a_{Cr} is the lattice constant of Cr.

The Cr SDW is commensurate $\epsilon = 0$ ($\Lambda_{\mathrm{SDW}} = \infty$) resulting in a simple antiferromagnetic (AF_0) structure with the corner atoms on the Cr bcc lattice antiparallely aligned to the center atoms. According to the discussion above this leads to peaks at the $\{001\}$ positions in the neutron scattering spectra, whereas the incommensurate SDW creates maxima in the proximity of the $\{001\}$ positions. Thus, the distinction of the commensurate and incommensurate Cr-SDW by neutron scattering is straightforward.

In the following the results obtained by neutron scattering to examine the SDW bulk behavior of the Cr crystal are presented. The white hatched area in the left sketch of Fig. 5.9 shows the area illuminated with the neutron beam in the first measurements. This includes the Cr crystal and some of the surrounding Ta frame. The resulting scans are shown in Fig. 5.9(a)-(d). At 200 K, well above the spin-flip temperature T_{SF}, satellite reflections are observed along the K and L direction in the vicinity of the (010) and the (001) forbidden Bragg positions for the structural reflections.

As the dark grey shaded components in Fig. 5.8 indicate, the occurrence of the satellites is characteristic for a transverse I-SDW as expected above T_{SF}. At 20 K, far below the spin-flip temperature, the satellites in the vicinity of the (001) position along the K direction in Fig. 5.9(b) and the satellites along the L direction next to the (010) position in Fig. 5.9(c) remain, but the satellites in Fig. 5.9(a) and (d) disappear. The result is highlighted in light grey in Fig. 5.8 and corresponds to the expected behavior for a longitudinal I-SDW. From the peak positions in Fig. 5.9(b), the period length of the SDW is calculated to be $\Lambda_{\mathrm{SDW}} = 70 \pm 4$ Å at 200 K and $\Lambda_{\mathrm{SDW}} = 64 \pm 4$ Å at 20 K using Eq. 5.4 which is in good agreement with Ref. [103].

In addition to the scans at 20 K and 200 K, the intensity of the satellite reflection in the K direction close to the (010) position was recorded during the cool down process (data not shown here). It was found that the intensity drops rapidly at about $T = 125 \pm 5$ K agreeing well with the expected T_{SF} of 123 K. By heating the sample above the bulk Néel temperature of $T_{\mathrm{N}} = 311$ K, all peaks related to magnetic scattering disappear (data not shown here), indicating that the Cr sample became paramagnetic.

Along with the satellite peaks in Fig. 5.9 peaks arising from magnetic scattering also appear at the (010) and the (001) Bragg positions. These reflections arise from magnetic scattering from a commensurate SDW (AF_0 phase). The appearance of the AF_0 phase can be attributed to the mechanical strain which is expected to be present at the crystal edges where the Ta foil presses onto the Cr surface. To check whether the AF_0 phase extends through the whole of the sample or is only at the edges of the sample, the beam size of the neutron beam was confined by a lithium plated aperture to an area of (2×2) mm^2 narrowing the illuminated spot to the center of the Cr crystal (see white hatched area in the left sketch of Fig. 5.10). Fig. 5.10 shows the corresponding neutron scattering scans. Qualitatively, the satellite reflections exhibit the same behavior as without

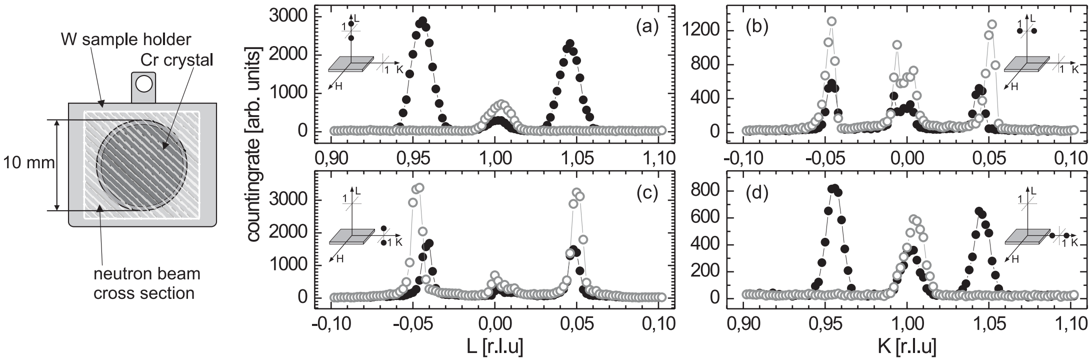

Figure 5.9: Neutron scattering data of Cr(001) measured with neutrons illuminating the entire crystal (see hatched area in drawing on the left). Measurement temperatures are $T_{\mathrm{SF}} < T = 200$ K (filled circles) and $T_{\mathrm{SF}} > T = 20$ K (open circles) to explore the propagation directions and polarizations of the spin-density waves. The scattering geometries are sketched in the insets.

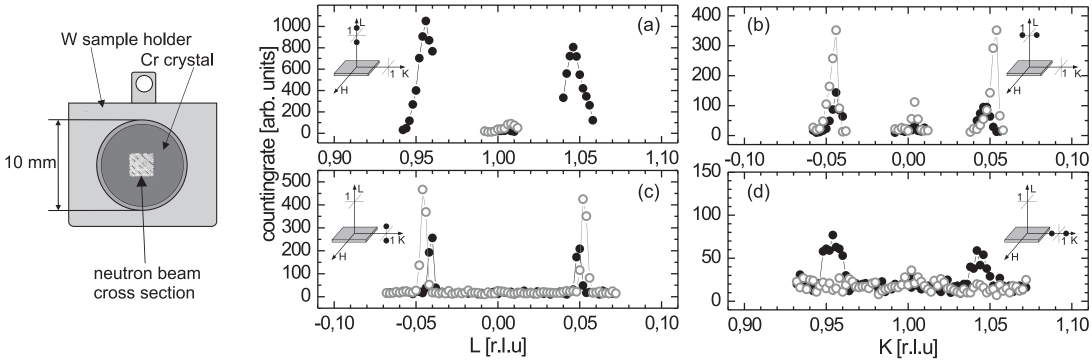

Figure 5.10: Neutron scattering data of Cr(001) measured with the neutron beam confined to the central region of the Cr crystal (see hatched area in drawing on the left). Measurement temperatures are $T_{\mathrm{SF}} < T = 200$ K (filled circles) and $T_{\mathrm{SF}} > T = 20$ K (open circles) to explore the propagation directions and polarizations of the spin-density waves. The scattering geometries are sketched in the insets.

an aperture, i.e., the existence of a transverse I-SDW above and a longitudinal I-SDW below T_{SF}. In contrast to the previous data taken by averaging over the entire crystal, however, the intensities of the commensurate SDW's are now dramatically reduced relative to the incommensurate satellites. The reflection at the (010) position has completely disappeared (cf. Fig. 5.10(c) and (d)). The incommensurate SDW phase is dominant in the center of the Cr crystal, i.e. the same position as for the SP-STS measurements. Similarly, the still visible but very weak commensurate SDW reflections at the (001) position is found to be minimal, when the neutron beam hits the center of the sample [see Fig. 5.10(a) and (b)]. The remaining intensity at (001) can be attributed to the fact, that during a scan the projection of the neutron beam on the sample surface changes from square as shown in Fig. 5.10 to rectangular thereby illuminating off-center areas of the sample leading to minor contributions from areas closer to the edges of the Cr crystal. This effect is significantly weaker for the scattering geometry of Figs. 5.10(c) and (d), than for Figs. 5.10(a) and (b).

In summary we have shown by neutron scattering that the Cr crystal later used in the temperature dependent SP-STS measurements shows all the characteristic bulk properties. The central region relevant for the SP-STS study is dominated by an incommensurate SDW configuration.

5.3 Temperature-dependent magnetic structure of the Cr(001) surface

All the previous experiments on the properties of the surface magnetic structure of Cr(001) were carried out at room temperature above the spin-flip temperature T_{SF}. The room temperature spin configuration with its in-plane magnetization and the resulting perpendicular alignment of the propagation vector $\vec{Q}$ relative to a Cr(001) surface without steps is presented in different way Fig. 5.11(a). The maximum of the T-SDW is located at the surface giving rise to a maximal surface magnetic moment. The question arises how the bulk spin-flip reorientation influences the magnetic structure of the Cr(001) surface below T_{SF} when the SDW becomes longitudinally polarized. Two possible models which are sketched in Fig. 5.11(b) and (c): Either the direction of the magnetic moment $\vec{\mu}$ or the propagation vector $\vec{Q}$ must be modified. In the former case $\vec{Q}$ remains perpendicular to the (001) surface. Furthermore, as for $T > T_{\mathrm{SF}}$, the surface magnetic moment has maximal value and the SDW antinode is pinned at the surface. Similar to the situation sketched in Fig. 5.11(a) the surface magnetic order exhibits topological antiferromagnetism but with an out-of-plane magnetization of the surface. In the second model $\vec{Q}$ may be oriented parallel to the (001) surface as shown in Fig. 5.11(c). In this case the surface magnetization remains in-plane but we no longer observe topological antiferromagnetism. Instead, a modulation of the magnetic moment with the period L of the SDW should be visible on atomically flat terraces. As I shall show both models are inconsistent with the experimental data which will be presented later on.

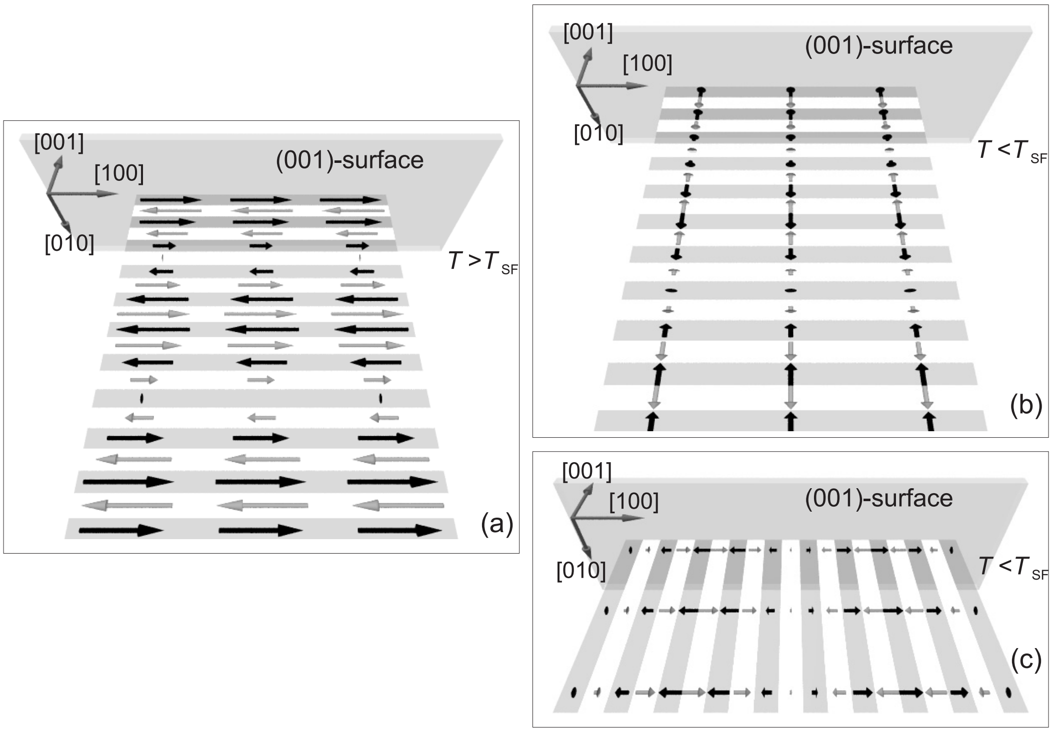

Figure 5.11: Schematic representations of the spin configuration of the Cr SDW at different temperatures. (a) At $T > T_{\mathrm{SF}}$ the T-SDW propagates perpendicular towards the Cr(001) surface. The maximum of the SDW is located at the surface and the surface layer has an in-plane ferromagnetic order. Below T_{SF} the $\vec{Q}$ vector of the L-SDW has two possible orientations relative to the surface: (b) perpendicular, with a maximum at the surface resulting in an out-of-plane ferromagnetic surface layer or (c) parallel to the surface with a modulation of the surface magnetic moment within the (001) surface.

5.3.1 Measurement procedures

We used polycrystalline W tips which were electrochemically etched *ex situ* and cleaned *in vacuo* by a high-temperature flash at $T \geq 2200$ K. Spin-resolved studies were carried out using *in situ* prepared Fe-coated W tips. Details of the tip preparation procedure are given in Refs. [68, 104]. From previous experiments performed in external magnetic fields we know that Fe-coated W tips are preferentially magnetized perpendicular to the tip axis [104, 105], i.e., parallel to the sample surface plane. With both tip and sample held at the same temperature T, maps of the spin-resolved differential tunneling conductance $\mathrm{d}I/\mathrm{d}U$ (magnetic signal) were recorded simultaneously with the constant-current images (topography) by adding a modulation voltage $U_{\mathrm{mod}} = 10$ $\mathrm{mV_{rms}}$ to the sample bias U

and detecting the dI/dU signal by a lock-in technique in a closed feedback circuit configuration.

The d_{z^2}-like surface state can be used to image the magnetic structure of the Cr(001) surface since it exhibits a spin polarization of about 20% because it is the minority-spin part of an exchange split d band [8, 65]. As we use Fe-coated W tips both electrodes are spin-polarized and the differential tunnel conductance measured at location $\vec{r}$ on the surface for a sample bias voltage U_0 can be written [28]:

$$\frac{\mathrm{d}I}{\mathrm{d}U}(\vec{r}, U_0)_{\mathrm{sp}} = C(1 + P_{\mathrm{s}} P_{\mathrm{t}} \cos\theta), \tag{5.5}$$

where $C = \mathrm{d}I/\mathrm{d}U(\vec{r}, U_0)_{\mathrm{sa}}$ is the spin-averaged part of the differential conductance, $P_{\mathrm{t}} = P_{\mathrm{t}}(E_{\mathrm{F}} - eU_0)$ and $P_{\mathrm{s}} = P_{\mathrm{s}}(E_{\mathrm{F}} + eU_0)$ is the spin polarization of the tip and the sample at energies $E_{\mathrm{F}} \pm eU_0$. The angle $\theta = \theta(\vec{M}_{\mathrm{s}}, \vec{M}_{\mathrm{t}}(\vec{r}))$ subtended between the tip magnetization $\vec{M}_{\mathrm{t}}$ and the local sample magnetization $\vec{M}_{\mathrm{s}}(\vec{r})$ below the tip apex. For an electronically homogeneous surface C and P_{s} are independent of the location $\vec{r}$ on the surface. Therefore, any lateral variation of the dI/dU signal is caused by the $\cos\theta$ term which—at a fixed magnetization direction of the tip—depends only on the local orientation of the sample magnetization $\vec{M}_{\mathrm{s}}(\vec{r})$. The d$I$/d$U$ signal is sensitive to the local electron spin density of the sample surface. Since the atomic structure of the cluster at the tip apex determines its (spin-dependent) electronic structure and since P_{t}, just as P_{s}, is a bias voltage dependent quantity, the bias voltage at which the product $P_{\mathrm{t}} \cdot P_{\mathrm{s}}$ has a maximum cannot be predicted and varies between different tips prepared in different experimental runs.

All "topographic" STM data shown below have been plane-fitted on atomically flat terraces to correct for the tilt of the sample. In order to enhance the contrast we mixed the tip height z and its derivative dz/dx with respect to the fast scan direction x. This image processing produces images which look as if the sample were illuminated by a light source from the left.

5.3.2 Results

Although a commensurate SDW (AF$_0$ phase) is present close to the edges of our Cr crystal—presumably due to the elastic strain caused by the clamping mechanism—our neutron scattering experiments revealed that the incommensurate SDW dominates the central region of the sample surface where the SP-STM measurements are performed. In the following we present surface sensitive spin-polarized STS measurements at variable temperatures in the range 20-300 K. It is still an open question how the magnetic structure of the Cr(001) surface behaves when crossing the spin-flip temperature. Figs. 5.12 and 5.13 show a series of six SP-STS measurements of the Cr(001) surface taken at temperatures between room temperature (T = 293 K) and 23 K, crossing the spin-flip temperature T_{SF} = 123 K. The surface topography and spin-resolved $\mathrm{d}I/\mathrm{d}U$ map are shown for each temperature. Due to the experimental requirement of good temperature stability during the measurement ($\Delta T \leq 0.05$ K) and the relatively high reactivity of Cr it was not possible to measure the entire temperature series in a single experimental run using the same tip and the same sample. Instead, each data set shown in Fig. 5.12 and 5.13 represents a new preparation of both the Cr sample and the Fe-coated tip.

Beginning with Fig. 5.12(a)-(c), the temperature of each measurement is above the spin-flip temperature T_{SF}. In principle, we observe the same magnetic structure in each data set i.e., topological antiferromagnetism, which in some cases is frustrated due to the presence of screw dislocations. The magnetic contrast—here the asymmetry of the $\mathrm{d}I/\mathrm{d}U$ signal with tip and surface spins parallel ($\sigma_{\uparrow\uparrow}$) and the signal with spins anti-parallel ($\sigma_{\uparrow\downarrow}$)—is given by

$$P_{\mathrm{asym}} = \frac{\sigma_{\uparrow\uparrow} - \sigma_{\uparrow\downarrow}}{\sigma_{\uparrow\uparrow} + \sigma_{\uparrow\downarrow}} \tag{5.6}$$

and varies between 1.5% and about 5%. As mentioned in Sec. 5.3.1 a quantitative discussion of the $\mathrm{d}I/\mathrm{d}U$ contrast is difficult as the data were measured with different tips which exhibit different spin-dependent electronic properties. Therefore, the differences in the $\mathrm{d}I/\mathrm{d}U$ contrast may be the result of a non-systematic variation of the tip spin-polarization or of the angle ϕ between the tip and the sample magnetization directions rather than a systematic change due to the reduction of the temperature. The right column, Fig. 5.13(a)-(c), shows data which were measured at temperatures below T_{SF}. Surprisingly, the $\mathrm{d}I/\mathrm{d}U$ map in Fig. 5.13(a) exhibits the same magnetic structure as the images (a)-(c). Even down to 23 K [Fig. 5.13(c)] there is no change in the magnetic structure and adjacent terraces exhibit an antiparallel magnetization. The asymmetry varies between about 3% at 100 K and 10.6% at 23 K.

Since we know from the neutron-scattering experiments that the bulk of this particular Cr crystal exhibits a spin-flip transition at the expected spin flip temperature T_{SF} the SP-STM shown in Fig. 5.12 and 5.13 is astonishing. From the simple model outlined in Fig. 5.11 we expected that below T_{SF} the surface magnetization will either become perpendicular (out-of-plane) or the SDW should propagate within the surface plane leading to a periodic magnetization modulation. The configuration illustrated in Fig. 5.11(b) and (c) do not agree with our

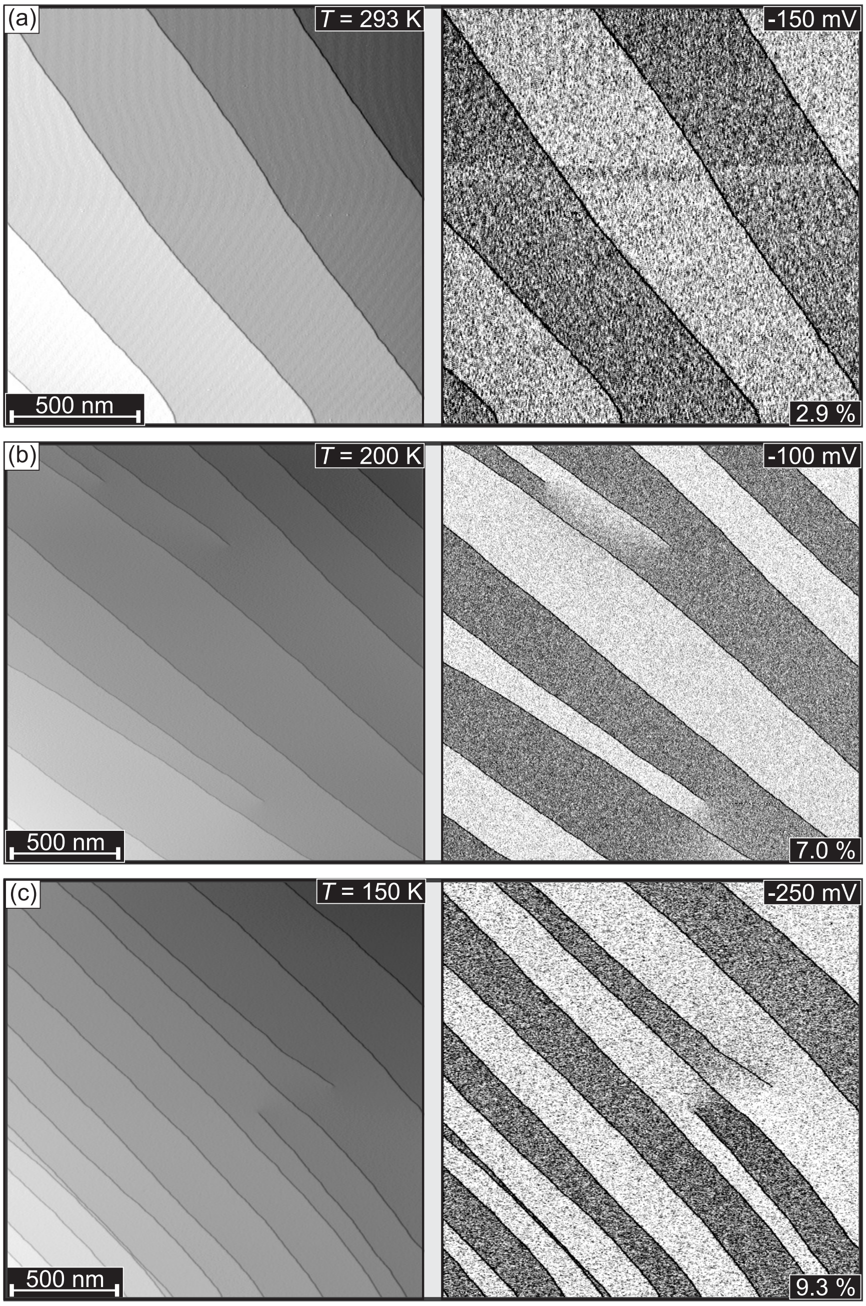

Figure 5.12: Temperature-dependent SP-STM series of Cr(001) above T_{SF} measured with an Fe-coated W tip. The surface topography (left) and the $\mathrm{d}I/\mathrm{d}U$ map (right) are shown for temperatures indicated in the upper right corner of the topographic images. The bias voltage U and the asymmetry P_{asym} are indicated in the upper right and lower right corner of the $\mathrm{d}I/\mathrm{d}U$ map.

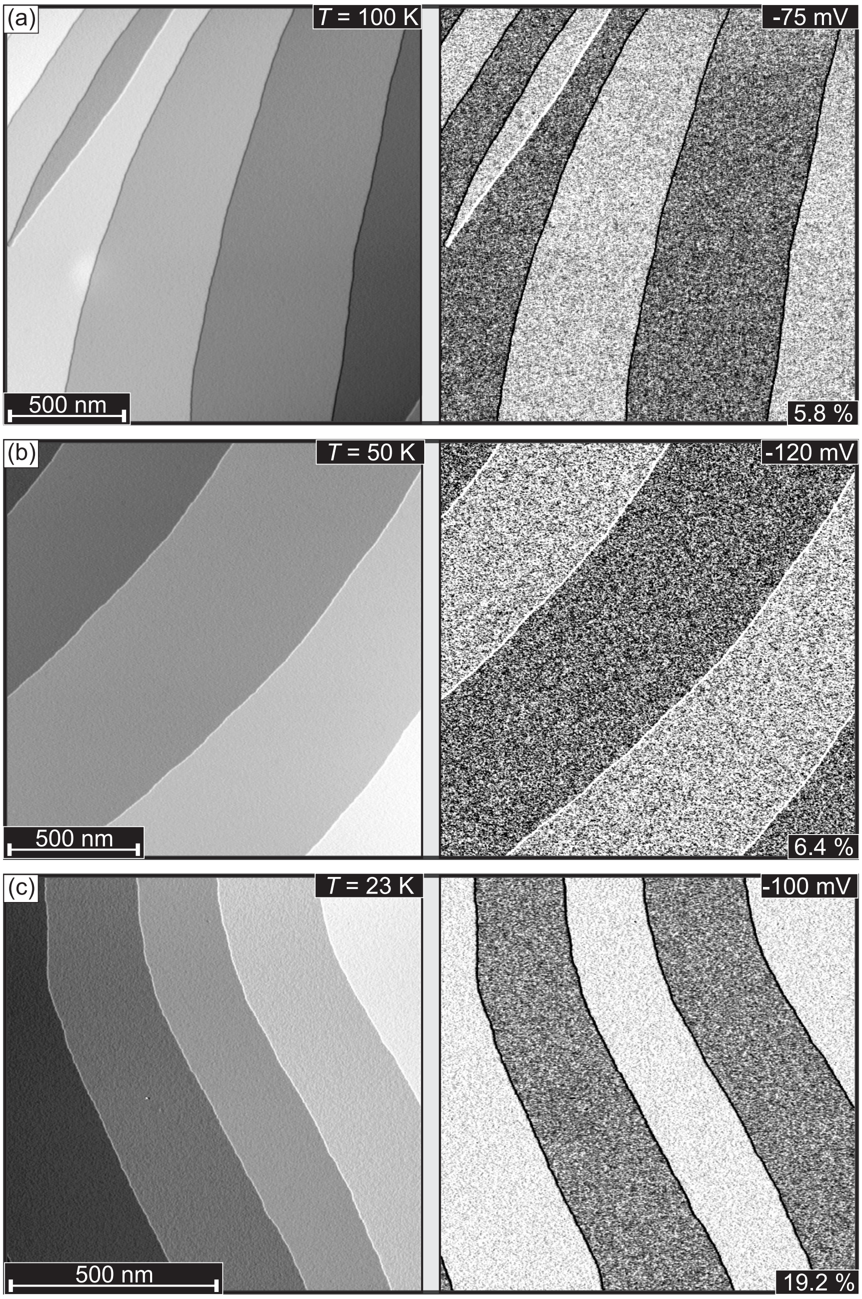

Figure 5.13: Temperature-dependent SP-STM series of Cr(001) below T_{SF} measured with an Fe-coated W tip. The surface topography (left) and the dI/dU map (right) are shown for temperatures indicated in the upper right corner of the topographic images. The bias voltage U and the asymmetry P_{asym} are indicated in the upper right and lower right corner of the dI/dU map.

experimental observations.

As mentioned earlier in Sec. 2.6, the easy magnetization axis of thin film tips used in SP-STM experiments is mainly determined by the material specific surface and interface anisotropies [68, 104]. The magnetization direction of Fe-coated tips, which were used for the experiments described here, was found to be particularly reproducible perpendicular to the tip axis, i.e., within the surface plane of the sample. Occasionally, however, we observed individual tips with a magnetization direction which differed from the usual direction. In addition in some cases intra-atomic non-collinear magnetism leads to a bias-dependence of the tip spin density orientation so that tips can be in-plane sensitive at one bias voltage but out-of-plane sensitive at another bias voltage [105].

In order to exclude that the contrast observed below T_{SF} in Fig. 5.13(a)-(c) is caused by out-of-plane topological antiferromagnetism, we performed a comparative study on the extensively investigated magnetic model system of 2 ML Fe on W(110) [106, 107]. Fe grows in the step-flow mode, i.e., the W substrate step edges are decorated with Fe nanostripes of alternating monolayer and double-layer thickness [108]. The Fe double-layer nanostripes exhibit an out-of-plane easy axis with stripe domains running along the $[1\bar{1}0]$ direction. As the up or down magnetized stripes are about 25 nm wide, the lateral magnetic periodicity along the [001] direction is $\simeq$ 50 nm. The stripe domains are separated by 180° domain walls. Within the domain walls the magnetization rotates continuously thereby passing one magnetically hard in-plane orientation.

For the comparative study we have coated a clean W tip with about 10 ML Fe. With this tip we have measured Fig. 5.14(a) which shows the topography of an almost perfect Fe double-layer grown on a stepped W(110) substrate at about $T = 450 \pm 50$ K. The measurement temperature during the entire cycle was 40 K. In the upper part of Fig. 5.14(b) the simultaneously acquired map of the spin-resolved differential tunneling conductance $\mathrm{d}I/\mathrm{d}U$ at $U = +50$ mV is shown. About 7 nm wide bright and dark lines running along the $[1\bar{1}0]$ direction can be seen which are characteristic for domain walls imaged by an in-plane sensitive tip [107]. Additional dislocation lines are also visible as dark lines along the [001] direction. In-plane sensitivity is also observed at the bias voltage of +700 mV shown in lower part of Fig. 5.14(b).

In the second step of the comparative study we replaced the Fe/W(110) sample by the Cr(001) sample while leaving the tip unchanged. Figs. 5.14(c) and (d) show the spin-resolved $\mathrm{d}I/\mathrm{d}U$ map of the Cr(001) surface as measured at $U = +50$ mV and $U = -100$ mV with the sample held at $T = 40$ K. One can recognize the typical contrast between adjacent terraces as previously shown in

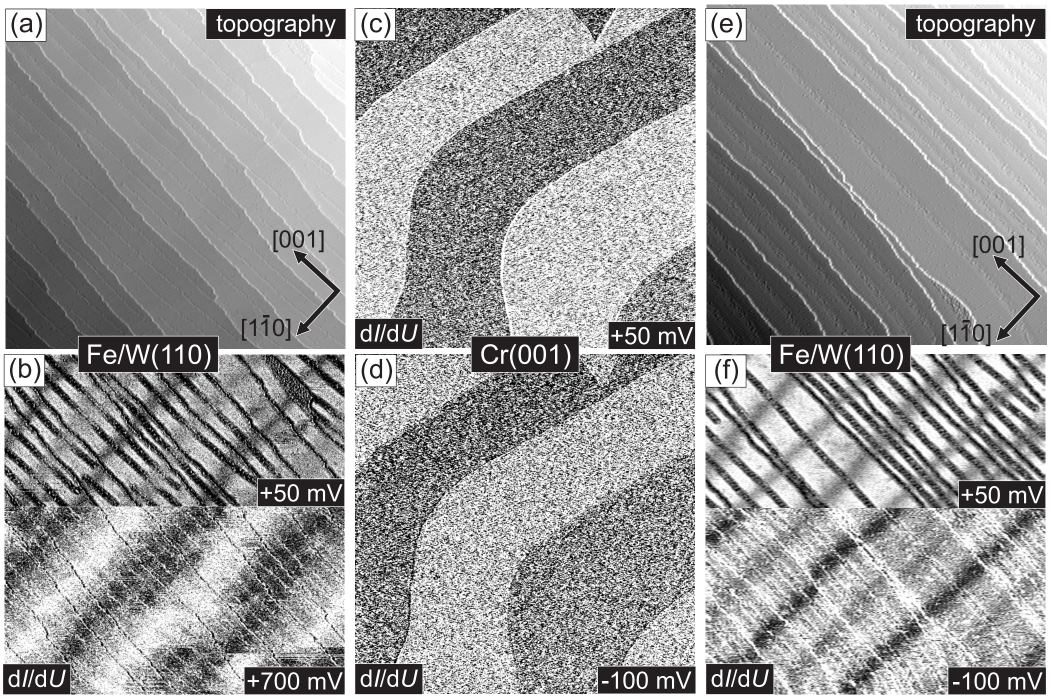

Figure 5.14: Experimental cycle as described in the text to determine the orientation of the magnetization of the Cr(001) surface at 40 K. (a) and (b) show the topography and dI/dU map of a 2 ML Fe/W(110) test sample; (c) and (d) dI/dU maps of Cr(001); (e) and (f) again the 2 ML Fe/W(110) measured after the Cr(001) sample.

Figs. 5.6 and 5.12 and 5.13. We have shown in Fig. 5.14(b) on Fe/W(110) that this particular Fe-coated tip is magnetically in-plane sensitive. So we can conclude that the Cr moments of the (001) surface are definitely in-plane although we are far below T_{SF}. In order to exclude that the magnetization changed between recording the data in Fig. 5.14(a)/(b) and (c)/(d) the Cr(001) sample was replaced by the previous Fe/W(110) sample [Fig. 5.14(e) and (f)] and found that the tip still shows in-plane sensitivity [Fig. 5.14(f)]. After carrying out these experiments we can be sure that the Cr(001) surface has in-plane magnetization far below the spin-flip temperature T_{SF}.

5.3.3 Discussion

In the previous section we have shown by neutron scattering that the particular Cr(001) crystal which was used in this study exhibits SDWs along the polar and one of the longitudinal directions, i.e., L and K, respectively. Although we have not performed measurements which are sensitive to the second longitudinal direction, H, which is equivalent to K, we can conclude that the bulk properties of this Cr(001) crystal are well-described by a SDW state in poly-$\vec{Q}$ mode. All three propagation directions for the L-SDW as for the T-SDW along the equivalent $\langle 001\rangle$-directions were observed in neutron scattering. In contrast, on the Cr(001) surface we find a single $\vec{Q}$ state with the propagation direction perpendicular to the surface. This result is in agreement with previous X-ray and neutron scattering studies which observed single $\vec{Q}$ states on a large variety of Cr(001) surfaces and interfaces [96–98, 109]. The near-surface region was determined to extend over ≈ 1 μm.

Our neutron scattering experiments [cf. Sec. 5.2] also confirm that the bulk of our Cr crystal exhibits spin-flip reorientation. The phase transition was found at $T_{SF} = 125 \pm 5$ K and is in good agreement with the literature value. Nevertheless, no indication of a spin-flip transition of the Cr(001) surface is observed by SP-STS down to $T = 23$ K. Throughout the entire temperature range, both above and far below T_{SF}, the surface remains in-plane magnetized and no modulation of the magnetic moment is observed in the surface plane, suggesting the perpetuation of the T-SDW at the surface. Since neutron scattering data clearly showed a L-SDW with out-of-plane magnetic moments [97] [cf. Fig. 5.11(b)] there seems to be an apparently disagreement with our SP-STS results. We have to keep in mind, however, that in contrast to the neutron scattering measurements mentioned above, which could not be performed *in situ*, i.e., at the same location where the sample preparation took place, leading to exposure to ambient conditions and oxidation, the SP-STS experiments of this study were conducted on a clean and well-defined Cr(001) surface. Probably, the oxidation of the samples used in Ref. [97] drastically changed the surface spin configuration.

Obviously, the surface magnetic structure cannot be described appropriately by a simple continuation of the bulk SDW. A schematic of a possible magnetic configuration at the surface is shown in Fig. 5.15. Here, the Cr surface layer exhibits the same magnetic structure as for $T > T_{\mathrm{SF}}$, i.e., a T-SDW ($\vec{Q} \perp \vec{\mu}$) with $\vec{Q}$ perpendicular to the surface plane. This T-SDW with the spins in-plane forms a quasi closure domain. A continuous connection of the surface T-SDW to the L-SDW in the near-surface region is accomplished by the formation of a 90° domain wall. The origin of the pinning of the surface magnetization within the plane may arise from a strong in-plane surface anisotropy of the Cr(001) surface. The magnetic structure of Fig. 5.15 is only stable, if the gain of the surface anisotropy energy density is higher than the energy density of the 90° domain wall. In other words, the energy required for the formation of a 90° domain wall must be overcompensated by an alignment of the surface magnetization along the easy axis

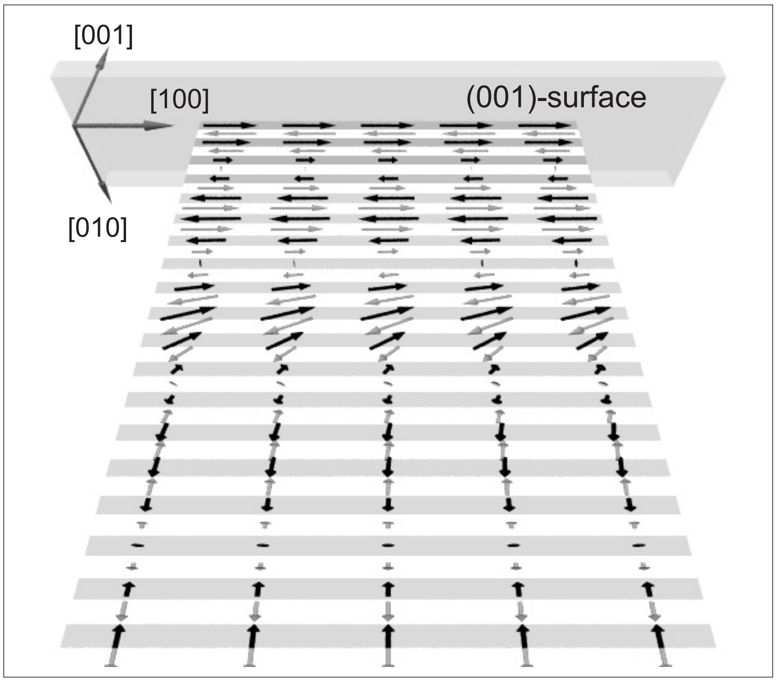

Figure 5.15: Model of the low-temperature spin configuration of Cr(001). At $T < T_{\mathrm{SF}}$ the bulk exhibits a L-SDW. A single $\vec{Q}$ state with $\vec{Q}$ perpendicular to the surface dominates in the near-surface region. The surface layer, in contrast, still exhibits a T-SDW with the magnetization lying within the surface plane. A 90° domain wall interconnects the L-SDW to the surface spins.

which—due to surface anisotropy—is oriented parallel to the (001) plane. Based on the knowledge of the domain wall width (cf. Fig. 5.6) we may speculate that the vertical extent of the 90° domain wall lies between one and several hundred nanometer.

5.4 Summary

We have shown by neutron scattering that the center of the Cr crystal used in the present work exhibits all the known bulk properties. We observed a transverse incommensurate SDW above T_{SF} and a longitudinal incommensurate SDW below T_{SF}. The commensurate AF_0 phase was only observed at the edge of the Cr crystal. Temperature-dependent SP-STS measurements revealed that the Cr(001) surface exhibits topological antiferromagnetic order with an in-plane magnetization throughout the entire temperature range 300 K $< T \leq$ 23 K. No spin-flip transition is observed at the surface. This experimental result is interpreted in terms of a high surface anisotropy large enough to overcompensate the energy required for the formation of a 90° domain wall which connects the in-plane magnetized near-surface region with the L-SDW in the bulk.

5.5 Variable-temperature STS on the Cr(001) surface

The electronic structure of the Cr(001) surface has been investigated extensively because of the very special magnetic properties of elemental Cr which exhibits antiferromagnetism and a long-period spin density wave. In a combined experimental and theoretical work Klebanoff *et al.* [89] found occupied and empty surface states of $d_{xz,yz}$-orbital symmetry which are energetically located about 1 eV below and above the Fermi level E_{F}. Furthermore, a peak close to E_{F} was observed and explained in terms of a d_{z^2}-like surface state [90]. Later on, Stroscio *et al.* [66] confirmed this interpretation. By using scanning tunneling spectroscopy (STS) a narrow maximum of the differential conductance $\mathrm{d}I/\mathrm{d}U$ was observed at 0.05 eV below the Fermi level (occupied states) [66]. This maximum was attributed to a spin-polarized Shockley-like surface state with d_{z^2}-orbital character. According to density functional theory (DFT) band structure calculations this is a general property of a bcc(001) surface. It should be mentioned, however, that in all calculations mentioned above the experimentally observed binding energy could only be reproduced if the Cr surface magnetic moment—which is consistently determined to be 2.5 μ_{B} in both experimental [89] and self-consistent density functional calculations [66]—is arbitrarily reduced (e.g., down to 1.75 μ_{B} in Ref. [66]).

To unravel this apparent inconsistency Kolesnychenko *et al.* [67] recently proposed a different interpretation of the density of states peak close to E_{F} in terms of a Kondo resonance. By employing to a sophisticated preparation procedure which is based on the cleavage of bulk crystals at low temperature [110] they were able to produce a Cr(001) surface with an unprecedented cleanliness limited only by the concentration of bulk impurities. Scanning tunneling microscopy (STM) experiments performed on these surfaces revealed interference patterns which are inconsistent with a d_{z^2}-like surface state but rather indicate a $d_{xz,yz}$-orbital symmetry. In contrast to earlier interpretations, the narrow resonance is explained by an orbital Kondo resonance formed by the two degenerate spin-split d_{xz}, d_{yz} surface states located about 1 eV above and below E_{F} [67]. Similar to the conventional (magnetic) Kondo effect, where the local magnetic moment is screened by a spin-flip mechanism, the orbital Kondo resonance results from the flip of the orbital moment of the d_{xz}, d_{yz} surface state, thereby forming a many-body "orbital singlet" [67].

We have performed a temperature-dependent STS study of the spectral shape of the peak close to E_F to get more data in order to decide which of the two physical interpretations is correct. The choice is between the Shockley-like surface state model within single particle band theory or the many-body Kondo resonance model. These experiments cover a wide range temperatures from 22 K up to 350 K, crossing both the magnetic phase transition temperatures of bulk Cr, i.e., the Néel temperature $T_\mathrm{N} = 311\,\mathrm{K}$ and the spin-flip temperature $T_\mathrm{SF} = 123$ K, and the Kondo temperature T_K. Although the peak position remains essentially unchanged our experiments reveal a significant broadening of the peak with increasing temperature. The temperature-dependent spectral shape is fitted within the framework of the two models. While the data can be described consistently within the Kondo model, electron–phonon coupling can only explain the data if the electron–phonon coupling constant λ is one order of magnitude larger than in $\vec{k}$-averaged bulk data.

5.5.1 Measurement procedure

STM images were recorded in constant-current mode with a stabilizing current I_stab and a bias voltage U_stab applied to the sample. We use polycrystalline W tips which were electrochemically etched *ex situ* and cleaned *in vacuo* by a high-temperature flash at $T \geq 2200$ K. The STM topographic data were plane-fitted to compensate for the misalignment of tip and sample. We enhanced the contrast of some STM images by mixing the topographic height with its derivative along the fast scan direction.

Spectroscopic information is obtained by adding a small ac modulation voltage $U_\mathrm{mod} = 5\,\mathrm{mV_{rms}}$ ($\nu = 5.777\,\mathrm{kHz}$) to the bias voltage U_stab with both tip and sample held at the same temperature T. We have confirmed that a further reduction of U_mod did not lead to a narrower linewidth. At every point (x, y) of the image, the tip is first stabilized at U_stab and I_stab. After opening the feedback-loop, the bias voltage is linearly ramped from the stabilization value U_stab to a final value. Simultaneously, the $\mathrm{d}I/\mathrm{d}U(U, x, y)$ signal is measured by the lock-in technique. The resulting $\mathrm{d}I/\mathrm{d}U(U, x, y)$ spectrum is a measure of the sample's local density of states (LDOS) at the position (x, y) below the tip apex with U corresponding to the electron energy with respect to E_F [11, 13, 111]. The overall spectroscopic energy resolution is given by [cf. Sec. 2.5

$$\Delta E = \sqrt{(3 \cdot k_{\mathrm{B}} T)^2 + (2.5 \cdot e\, U_{\mathrm{mod}})^2}\ . \tag{5.7}$$

To correct for binding energy shifts due to the finite time constant, the spectra were recorded in both directions, i.e., from negative to positive sample bias and *vice versa*.

5.5.2 Clean Cr(001) surface at 22 K

The surface electronic structure of Cr(001) may depend strongly on the surface quality. Since the Cr(001) surface studied here is prepared by Ar^+-ion etching and annealing while a related study used surfaces created by cleavage of bulk crystals [67] we have to first verify that both surfaces exhibit the same electronic properties. This was done at the lowest temperature achievable in our experimental setup, i.e., 22 K. Fig. 5.16(a) shows a typical topographic image of a sputter-cleaned Cr(001) surface. Five terraces are depicted which descend from the lower right to the upper left edge of the image. Higher resolution STM topographs reveal a surface defect concentration in the order of 1% of the surface atoms in agreement with the AES results mentioned previously. The cross section in panel (b) has been drawn along the black line marked in Fig. 5.16(a). Adjacent terraces are separated by monatomic steps of 1.44 Å height. The terrace and step structure is the result of a slight miscut (locally about 0.04° and averaged over the whole sample surface approximately 0.15° with respect to the ideal (001) surface). The surface electronic structure can be characterized by STS measurements. Fig. 5.16(c) shows an STS spectrum taken in the middle of a Cr(001) terrace far away ($\approx 3\,\mathrm{nm}$) from defect sites. A strong and very narrow peak at $\sim$20 mV above the Fermi level can be seen. Qualitatively, our data agree with the results measured on cleaved Cr(001) [67, 110]. For a more quantitative analysis we followed the procedure of Kolesnychenko *et al.* [67] by fitting the measured STS spectra with a Fano resonance profile [112, 113]

$$\frac{\mathrm{d}I}{\mathrm{d}U} \propto \frac{(q+\varepsilon')^2}{1+\varepsilon'^2}, \qquad \varepsilon' = \frac{eU - \varepsilon_0}{\Gamma/2}\ . \tag{5.8}$$

Here q reflects the ratio of the matrix elements linking the initial state to the continuum, ε_0 is the resonance energy, and Γ is the resonance width (FWHM). The best fit to our data is achieved for $\Gamma/2 = 15.4 \pm 0.3$ meV and $\varepsilon_0 = 22.9 \pm 0.3$ meV which is in good agreement with the values of 15 meV and 20 meV in Ref. [67]. At this point we can conclude that in respect to its electronic properties the

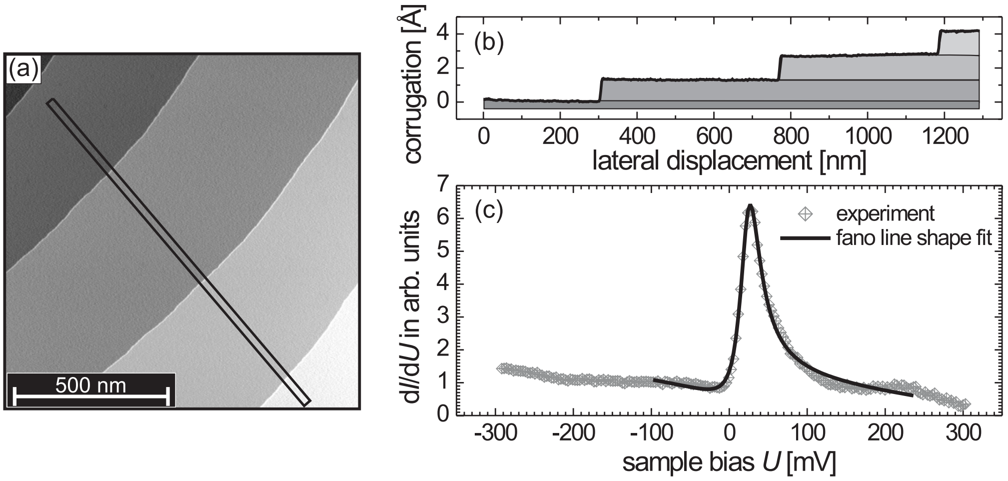

Figure 5.16: (a) Topographic STM image of a clean Cr(001) surface (tunneling parameters: $U = -0.12$ V, and $I = 0.3$ nA). (b) Line-section taken along the box in (a). Atomically flat terraces are separated by monatomic steps of 1.44 Å height. (c) Tunneling $\mathrm{d}I/\mathrm{d}U$ spectrum of Cr(001) measured at 22 K in the middle of a terrace (measurement parameters: $U_{\mathrm{stab}} = -0.3$ V and $I_{\mathrm{stab}} = 0.7$ nA). The solid black line is a Fano fit to the data with $\Gamma/2 = 15.4 \pm 0.3$ meV, $q = 3.9 \pm 0.16$ meV, and $\varepsilon_0 = 22.9 \pm 0.3$ meV.

sample quality of our sputter-cleaned Cr(001) surface is fully comparable with surfaces prepared by cleavage at low temperature, despite the fact that the defect concentration is lightly higher.

5.5.3 Temperature-dependent STS

Due to the experimental requirement of a very good temperature stability during the measurement ($\Delta T \leq 0.05\,\mathrm{K}$) and the relatively high reactivity of Cr it was not possible to measure a complete temperature series within a single experimental run using the same tip and sample surface. Instead, we had to perform an experimental run with a newly prepared tip and sample for each particular temperature. For the ease of comparability we always performed the measurements with the stabilization parameters $U_{\mathrm{stab}} = -0.4$ V and $I_{\mathrm{stab}} = 0.5$ nA and the same energy resolution (400 points in the energy range of ± 0.4 V). In each case 100 spectra were recorded in the middle of an atomically flat Cr(001) terrace. Measured tunneling $\mathrm{d}I/\mathrm{d}U$ spectra (open circles) at eight selected temperatures (out of a total of 12) covering the range between 22 K and 350 K are shown in Fig. 5.17(a). The peak close to the Fermi level can be recognized clearly throughout the entire temperature range although it broadens significantly with increasing temperature.

The peak position remains constant within the limits of our experimental accuracy of a few meV.

In the following we will discuss the temperature-dependence of the spectral shape in the framework of the two competing models, i.e., Kondo theory and single particle band theory.

Many-body Kondo effect

The Kondo effect is a well-known many-body phenomenon and describes how localized electrons interact with delocalized electrons to form of a many-body singlet state which enhances the LDOS near the Fermi level [114]. The splitting of the Kondo resonance in an applied magnetic field and the broadening and reduction of the Kondo resonance with increasing temperature are Important characteristics of the Kondo effect [115–121].

It is a non-trivial task to deconvolute the intrinsic temperature-induced variation of the sample density of states from that of the tip as recently shown for Ti atoms on Ag(100) [122]. It can be seen that the measured $\mathrm{d}I/\mathrm{d}U$ signal is always a convolution of the sample LDOS ρ_s and the derivative of the Fermi-Dirac distribution from the standard relation for STM $\mathrm{d}I/\mathrm{d}U$ spectra [12]

$$\frac{\mathrm{d}I}{\mathrm{d}U}(U,T) = \int\limits_{-\infty}^{+\infty} \rho_{\mathrm{t}}\rho_{\mathrm{s}}(E,T)\,\frac{\mathrm{d}}{\mathrm{d}U}\,F(E-eU,T)\,\mathrm{d}E \tag{5.9}$$

where $\rho_{\mathrm{s}}(E,T)$ is the energy- and temperature-dependent local density of states (LDOS) of the surface, ρ_{t} is the LDOS of the STM tip (assumed to be featureless) and $F(E,T)$ is the Fermi-Dirac distribution. To extract the intrinsic LDOS feature from the spectra at higher temperatures a Fano resonance line shape given by Eq. 5.8 (solid gray line) were taken and thermally broadened using Eq. 5.9 to fit the experimental data of Fig. 5.17. It was necessary in some cases (see, e.g., data measured at $T = 102$ K) to add further Gaussian-shaped peaks to the fitting procedure (dash-dotted lines) probably due to tips with pronounced electronic states. Furthermore, a linear background (dashed) was added. An adequate agreement between the experimental spectra and the fit is achieved.

We can extract the temperature dependence of the width Γ of the $\mathrm{d}I/\mathrm{d}U$ spectroscopy peak in terms of a Kondo resonance [Fig. 5.17(b)] on the basis of the fitting procedure. The observed behavior of Cr(001) is similar to Ti/Ag(100) [122] and shows a parabolic increase of the width at low temperatures which becomes linear as the temperature increases. According to Refs. [121] and [122] in the temperature regime $T \leq T_{\mathrm{K}}$ the temperature dependence of the width of a magnetic

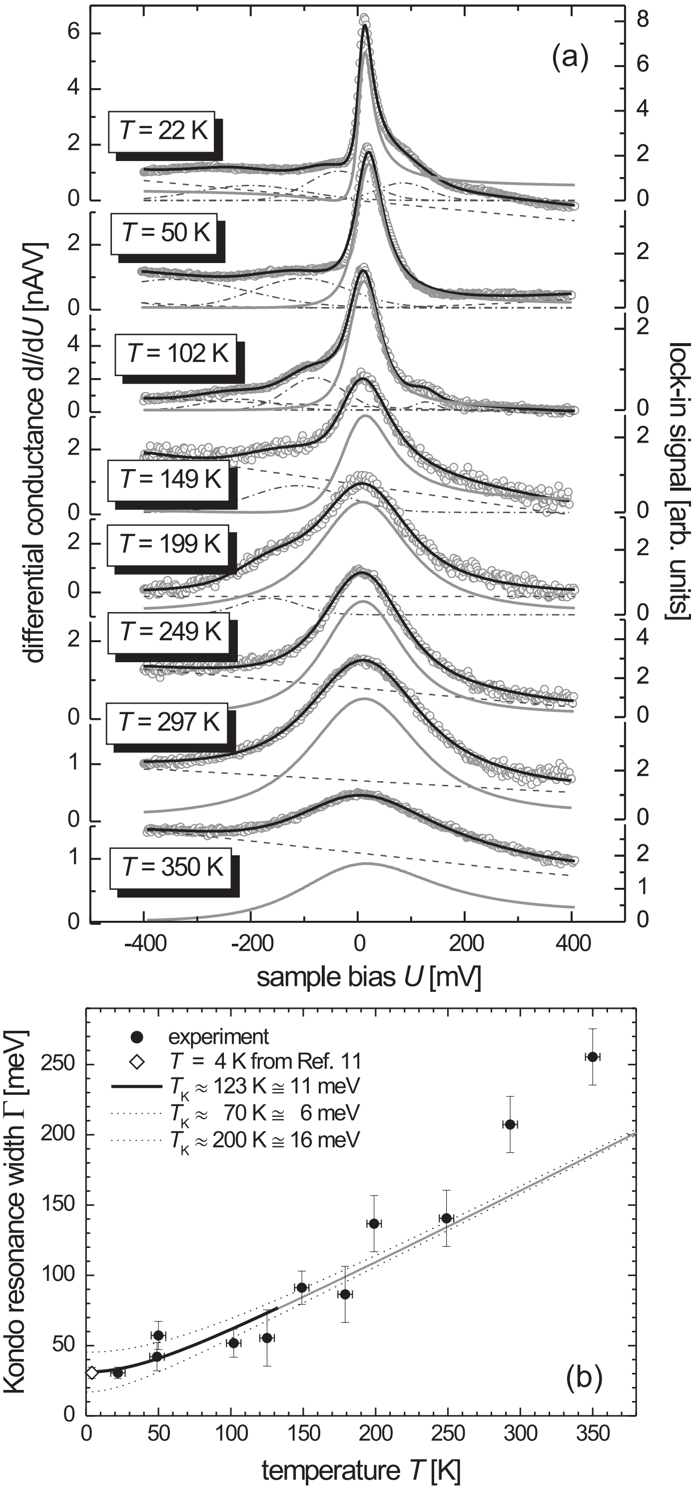

Figure 5.17: (a) STS spectra of Cr(001) measured at eight different temperatures between 22 K and 350 K (open circles). The experimental data were fitted by a Fano line shape for the peak close to E_F (solid red line), Gaussian peaks to account for tip states (dash-dotted), and a linear background (dashed). (b) Width Γ of the Fano peak to fit the data of (a). The solid and dotted curves show the theoretical temperature dependence given by Eq. 5.10 for different Kondo temperatures T_K. The best fit is obtained for $T_\mathrm{K} = 123$ K ($\approx 11\,\mathrm{meV}$).

spin-flip Kondo resonance is given by:

$$\Gamma = 2\sqrt{(\pi k_{\mathrm{B}}T)^2 + 2(k_{\mathrm{B}}T_{\mathrm{K}})^2} \ . \tag{5.10}$$

Here T_{K} is the only fitting parameter for adjusting the offset at zero temperature. The best result is obtained for $T_{\mathrm{K}} \approx 123$ K ($\cong 11$ meV).[2] Comparison between the experimental data of Fig. 5.17(b) and a plot of Eq. 5.10 reveals excellent overall agreement in the temperature range up to 200 K, i.e., much higher than the actual T_{K} which is usually considered as the upper limit for the validity of the underlying theory [122, 123]. The experimental data points only start to deviate from the theoretical model above 200-250 K.

Single-particle surface electronic state

The electronic structure and dynamics of surface states has recently attracted considerable attention. Improved experimental and theoretical techniques have led to consistent results for noble metals [124] but much less is known about the more complex transition metals. In the following we will discuss our Cr(001) data in terms of single-particle band theory.

As shown in Ref. [125] the lifetime τ of electronic states in non-magnetic metals is determined by three main contributions: electron-electron (*e*-*e*) scattering [126, 127], scattering by impurities or defects, and electron-phonon (*e*-*ph*) scattering [128]. If magnetic materials are considered there is an additional contribution, i.e., electron-magnon (*e*-*m*) scattering [129]. The (*e*-*e*)-scattering contribution to the linewidth Γ_{e-e} is given by Fermi liquid theory [125, 126],

$$\Gamma_{e-e} = 2\beta[(k_{\mathrm{B}}T)^2 + (E - E_{\mathrm{F}})^2] \ . \tag{5.11}$$

The factor β is of the order of 1 eV^{-1} and since the results discussed here were measured at low temperature, the temperature-dependent term in Eq. 5.11 is very small and can be neglected. Furthermore, the binding energy $E - E_{\mathrm{F}}$ of the Cr(001) peak amounts to only a few meV and the second term can also be neglected. The impurity scattering contribution is proportional to the impurity concentration, but independent of temperature and binding energy. Hence it can only give a temperature-independent broadening revealed by an offset at zero K. For the bulk, the magnitude of the effect is about 10meV/% [129, 130]. The only remaining contribution comes from electron-phonon (*e*-*ph*) scattering. Within the Debye model the inverse lifetime due to (*e*-*ph*) processes can be calculated from

---

[2] In Ref. [67] the peak width Γ was mistakenly labeled T_{K}

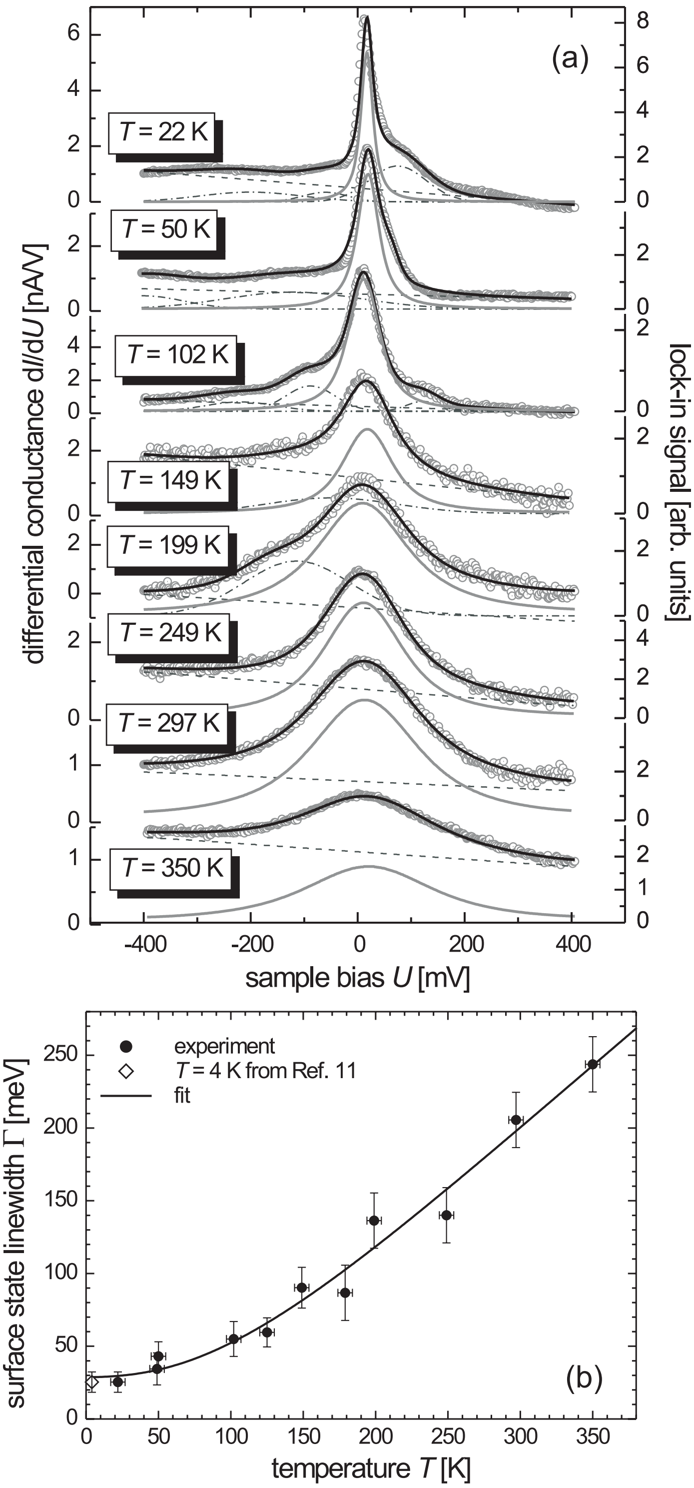

Figure 5.18: (a) STS spectra of Cr(001) measured at eight different temperatures between 22 K and 350 K (open circles). The experimental data were fitted by a thermally broadened Lorentzian line shape for the peak close to E_{F} (solid red line), Gaussian peaks to account for tip states (dash-dotted), and a linear background (dashed). (b) Width Γ of the Lorentzian to fit the data of (a). The solid curve shows the theoretical temperature dependence given by Eq. 5.12 for $\hbar\omega_{\mathrm{D}}^{\mathrm{bulk}} = 52.2$ meV and $\lambda = 1.5$.

the following formula:

$$\Gamma_{e\text{-}ph}(E,T) = \frac{\hbar}{\tau(E,T)} = \lambda \frac{2\pi}{(\hbar\omega_\mathrm{D})^2} \int\limits_0^{\hbar\omega_\mathrm{D}} \mathrm{d}E' E'^2 \cdot [1 - f(E-E') + 2n(E') + f(E+E')], \tag{5.12}$$

where ω_D is the Debye frequency, λ the electron–phonon mass enhancement factor, $f(E)$ the Fermi distribution and $n(E)$ the Bose–Einstein distribution. At high temperatures the phonon scattering $\Gamma_{e\text{-}ph}$ shows a linear dependence $\mathrm{d}\Gamma_{e\text{-}ph}/\mathrm{d}T \cong 2\pi\lambda k_\mathrm{B}$ and is independent of ω_D.

In a recent STS study by Rehbein *et al.* [131] the temperature-dependent broadening of Gd(0001) surface states was successfully explained by (*e-ph*) scattering within the framework of Eq. 5.12. We have applied the same fit procedure to the temperature-dependent spectral shape of the $\mathrm{d}I/\mathrm{d}U$ peak on Cr(001). The fit procedure is similar to Sec. 5.5.3, but the Fano line shape only appropriate for the Kondo effect is replaced by a Lorentzian function for (*e-ph*) scattering. The results are shown in Fig. 5.18(a). The extracted linewidth of the Lorentzian (FWHM) is plotted in Fig. 5.18(b). A quantitative description based on Eqs. 5.12 and 5.11 requires the knowledge of three parameters λ, $\omega_\mathrm{D}^\mathrm{surf}$ and Γ_{e-e}. As mentioned above Γ_{e-e} can be estimated from the peak width at zero temperature ($T = 0$ K). Owing to the lack of specific surface parameters for the Debye frequency, we used the Cr bulk value $\hbar\omega_\mathrm{D}^\mathrm{bulk} = 52.5$ meV [132]. Using a binding energy of $E_0 = 20 \pm 5$ meV the fitting procedure yielded in $\lambda = 1.51 \pm 0.40$ and $\Gamma_{e-e} = 19.5 \pm 3$ meV. The surface Debye frequency $\hbar\omega_\mathrm{D}^\mathrm{surf}$ will probably be different from the bulk value. Even if the experimental data are fitted with two fit parameters, $\hbar\omega_\mathrm{D}^\mathrm{surf}$ and λ, the values changed only slightly to $\hbar\omega_\mathrm{D}^\mathrm{surf} = 53$ meV and $\lambda = 1.53 \pm 0.40$.

5.5.4 Discussion

At this point we can recapitulate that our experimental data on the temperature-dependent peak shape of Cr(001) can be fitted nicely within the respective limits of validity by both physical models, i.e., as a many-body Kondo effect or within single-particle band theory. This is not unexpected since in both cases the peak width rises linearly at high temperature. One possibility to estimate which of the two models describes the physical basis of the observations is to evaluate whether the procedures led to reasonable fitting parameters. In each model there is only one fit parameter, i.e., the Kondo temperature T_K (cf. Eq. 5.10) or the mass-enhancement factor λ (cf. Eq. 5.12).

Unfortunately, the Kondo temperature of Cr(001)—if it is a Kondo system—is unknown. But it is a remarkable coincidence that the value determined $T_{\mathrm{K}} \approx 123$ K is very close to the Cr spin-flip temperature T_{SF}. It is well-known that the magnetic phase transitions of Cr are accompanied by structural transitions [74]. Due to the magneto-elastic interaction which is mediated by spin-orbit coupling the crystalline structure of Cr changes from cubic to orthorhombic at the paramagnetic-antiferromagnetic phase transition and then to tetragonal at the spin-flip temperature T_{SF}. One may speculate about possible orbital-ordering scenarios which have recently attracted interest with regard to metal-insulator and normal-superconductor transitions [133].

In contrast, the electron–phonon mass enhancement factor λ of polycrystalline Cr on a glass substrate was determined experimentally and theoretically. Optical pump-and-probe experiments give $\lambda = 0.13 \pm 0.02$ [134]. This value is rather close to the result of strong-coupling theory for paramagnetic Cr ($\lambda = 0.25$) [135]. The fit to our STS data yields a value which is 5-10 times larger. At first sight this seems to be inconsistent with earlier results on bulk Cr thereby excluding the single-particle band model and supporting the Kondo model. However, recent experiments on various elements revealed that the surface electron–phonon mass enhancement factor λ may deviate considerably from the $\vec{k}$-integrated bulk value. For example, a strong enhancement of λ at the W(110) surface compared to bulk W was found which was attributed to the degree of surface localization of the surface electron wave function [136]. Similar observations were made on Be($10\bar{1}0$) [137]. Furthermore, a strong dependence on binding energy was observed for Bi(100) [138]. Depending on the wave vector $\vec{k}$ even within one particular electron band λ may vary by more than one order of magnitude [139]. A mass enhancement factor $\lambda = 1.5$ is certainly realistic given the fact that our measurement technique (STS) is highly surface sensitive and governed by surface LDOS contributions from the $\bar{\Gamma}$-point of the surface Brillouin zone.

We conclude that our temperature-dependent STS data of Cr(001) are not adequate to decide which model is applicable. For the Kondo resonance we found quite good agreement between our experiment and the theoretical prediction, although the theory was developed formally for spin-flip scattering of single magnetic impurity atoms on open surfaces. On the other hand the analysis in terms of thermally broadened electron bands leads to a rather large mass-enhancement factor λ which is 5-10 times larger than the average bulk value.

One possibility to determine which model is applicable would be to observe the effect of an increasing adsorbate concentration on the peak position and height. We have performed preliminary experiments with oxygen on Cr(001). As shown

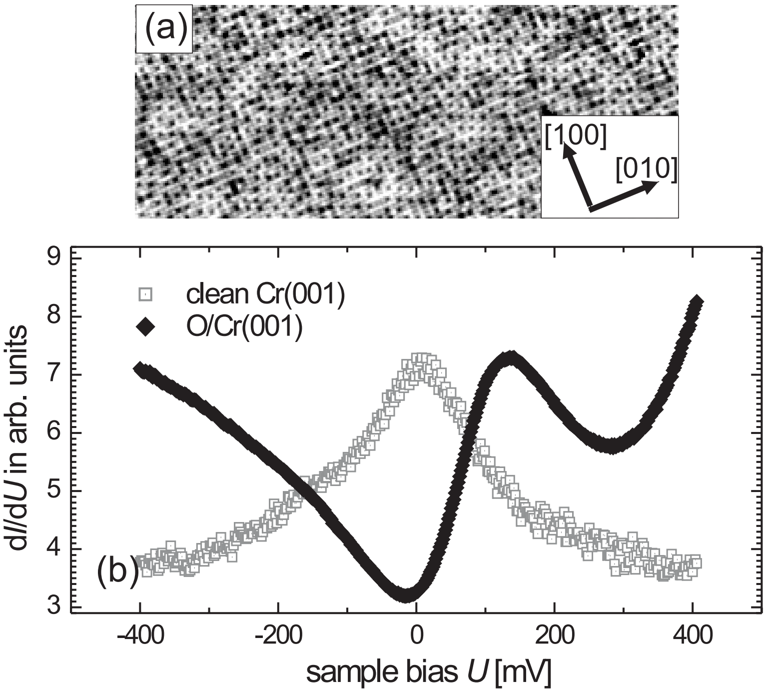

Figure 5.19: (a) Topographic STM image of O/Cr(001) measured at T = 200 K. The sample surface was dosed with 3 L O_2 at a sample temperature of T = 350 °C. (b) Tunneling dI/dU spectra of clean (grey) and oxygen-covered Cr(001) (black). A considerable peak shift by ≈ 120 meV is observed.

in Fig. 5.19(a) the exposure to 3 L O_2 at $T = 350$ °C leads to a $(\sqrt{5} \times \sqrt{5})R27^\circ$ reconstruction on the Cr(001) surface [140]. The tunneling dI/dU spectrum measured on the oxygen-covered Cr surface is compared to the spectrum of clean Cr(001) in Fig. 5.19(b). Both spectra were taken with different tips but at the same sample temperature T = 200 K. The oxygen treated surface exhibits a peak at ≈ 135 meV. This peak cannot be related to a Kondo resonance because it is too far from the Fermi level. It is, however, not clear whether the peak shifts continuously with increasing oxygen concentration or if the Cr-related peak intensity decreases while a new impurity-induced surface state arises as recently found on SiC(100) [141]. Further experimental and theoretical effort is necessary to clarify the situation. Another *experimentum crucis* would be a magnetic field-dependent study of the Cr(001) peak shape. Detailed theoretical predictions of the field-dependent spectral shape of an orbital Kondo resonance are available [142]. Although enormous fields are required to cause a significant effect, recently developed scanning tunneling microscopes [143] which are capable to measure at extremely low temperature in fields up to 14 T may be able to shed new light on the matter.

5.6 Summary

In summary, we have performed a temperature-dependent electronic structure investigation of the Cr(001) surface by means of variable-temperature scanning tunneling spectroscopy (STS). Our study covers a wide temperature range ($22\,\mathrm{K} \leq T \leq 350\,\mathrm{K}$) which includes the bulk magnetic phase transition temperatures as well as the possible Kondo temperature. We observe a sharp peak close to the Fermi level E_F which is consistent with earlier STS experiments. While the binding energy remains unchanged the peak broadens with increasing temperature. Our experimental data can be fitted within the framework of two physical models, i.e., single-particle band theory and Kondo theory. Both models lead to excellent agreement between the fit and the experimental data in the low temperature regime. Using the Kondo model a Kondo temperature T_K of $123\,\mathrm{K}$ is obtained. If interpreted in terms of single-particle band theory the fit results in an electron-phonon mass-enhancement factor λ which is 5-10 times larger than the averaged bulk value for Cr. However, there is excellent agreement between theory and the experimental data over the entire temperature range.

Chapter 6

Summary and Outlook

In this thesis the temperature-dependent electronic and magnetic properties of the Cr(001) surface were investigated under UHV conditions by scanning tunneling microscopy and spectroscopy.

A variable temperature STM was designed and built for temperature-dependent measurements. The STM has some unique features. First of all the entire microscope including tip and sample is cooled allowing high resolution spectroscopy measurements at low temperatures. An easy tip exchange mechanism allows *in situ* preparation of magnetically coated tips. The compact design of the STM body in combination with an eddy current damping stage permits atomic resolution imaging and high energy-resolution spectroscopy over the entire temperature range 20-300 K.

The temperature-dependent magnetic structure of the Cr(001) surface was imaged. My data on the magnetic structure of the Cr(001) surface are inconsistent with simple scenarios of a bulk terminated spin-density wave. Over the temperature range 20-300 K the surface magnetic structure is characterized by topological antiferromagnetism, i. e. the surface layer has a ferromagnetically ordered in-plane magnetization, but adjacent terraces separated by monatomic steps have an opposite orientation of the magnetic moment. The spin-flip transition which occurs in the bulk at a temperature of $T = 123$ K is absent at the Cr(001) surface. Although details of the subsurface magnetic structure is not accessible to SP-STM, a continuous connection of the surface T-SDW to the L-SDW in the near-surface region may be accomplished by the formation of a 90° domain wall. The origin of the pinning of the surface magnetization within the plane may be due to the strong in-plane surface anisotropy of the Cr(001) surface. Since the magnetic structure of the subsurface layer is not accessible to STM it is still an open question what happens under the surface. To answer this question further surface sensitive neutron scattering experiments under grazing incidence are planned.

The temperature-dependent STS measurements on the Cr(001) surface were motivated by two competing theoretical models to explain the peak in the differential conductance close to the Fermi level: either a surface state in one-electron band theory or an the orbital Kondo peak. The spectroscopy data were analyzed within the two models and gave good agreement in both cases. From the orbital Kondo effect model a Kondo temperature of $T_{\mathrm{K}} = 123$ K was estimated. The analysis with respect to a surface state leads within the Debye model of electron-phonon scattering to a mass-enhancement factor of $\lambda \approx 1.5$ which is 5-10 times larger than the averaged bulk value. On the basis of the available data we conclude that the temperature-dependent STS results on Cr(001) are not sufficient to decide between the two available models. STS spectra recorded in a strong external field should produce a field-dependent splitting of the Kondo peak and hence provide a direct confirmation of the Kondo model [142].

Bibliography

[1] A. Jordan, P. Wust, and H. Fähling, Int. J. Hyperthermia **9**, 51 (1993).

[2] A. Jordan, R. Scholz, P. Wust, H. Fähling, and R. Felix, J. Magn. Magn. Mater. **201**, 413 (1999).

[3] F. J. Himpsel, J. E. Ortega, G. J. Mankey, and R. F. Willis, Adv. Phys. **47**, 511 (1998).

[4] C. L. Dennis, R. P. Borges, L. D. Buda, U. Ebels, J. F. Gregg, M. Hehn, E. Jouguelet, K. Ounadjela, I. Petej, I. L. Prejbeanu, et al., J. Phys.: Condens. Matter **14**, R1175 (2002).

[5] G. Binasch, P. Grünberg, F. Saurenbach, and W. Zinn, Phys. Rev. B **39**, 4828 (1989).

[6] M. N. Baibich, J. M. Broto, A. Fert, F. N. V. Dau, F. Petroff, P. Eitenne, G. Creuzet, A. Friederich, and J. Chazelas, Phys. Rev. Lett. **61**, 2472 (1988).

[7] R. Wood, IEEE Trans. Magn. **36**, 36 (2000).

[8] R. Wiesendanger, H. J. Güntherodt, G. Güntherodt, R. J. Gambino, and R. Ruf, Phys. Rev. Lett. **65**, 247 (1990).

[9] G. Binnig and H. Rohrer, Helv. Phys. Acta **55**, 726 (1982).

[10] R. Wiesendanger, *Scanning Probe Microscopy and Spectroscopy* (Cambride University Press, Cambridge, UK, 1994).

[11] J. Tersoff and D. R. Hamann, Phys. Rev. B **31**, 805 (1985).

[12] J. Bardeen, Phys. Rev. Lett. **6**, 57 (1961).

[13] J. Tersoff and D. R. Hamann, Phys. Rev. Lett. **50**, 1998 (1983).

[14] C. J. Chen, *Introduction to scanning tunneling microscopy* (Oxford University Press, New York, 1993).

[15] J. Wintterlin, J. Wiechers, H. Brune, T. Gritsch, H. Höfer, and R. J. Behm, Phys. Rev. Lett. **62**, 59 (1989).

[16] V. M. Hallmark, S. Chiang, J. F. Raboldt, J. D. Swalen, and R. J. Wilson, Phys. Rev. Lett. **59**, 2879 (1987).

[17] C. J. Chen, Phys. Rev. Lett. **65**, 448 (1990).

[18] A. Selloni, P. Carnevali, E. Tosatti, and C. D. Chen, Phys. Rev. B **31**, 2602 (1985).

[19] V. A. Ukraintsev, Phys. Rev. B **53**, 11176 (1996).

[20] R. M. Feenstra, J. A. Stroscio, and A. P. Fein, Surf. Sci. **81**, 295 (1987).

[21] J. A. Stroscio, R. M. Feenstra, and A. P. Fein, Phys. Rev. Lett. **57**, 2579 (1986).

[22] D. Haude, Ph.D. thesis, Universität Hamburg (2001).

[23] D. T. Pierce, J. Ungaris, R. J. Celotta, and M. D. Stilles, J. Magn. Magn. Mater. **200**, 290 (1999).

[24] P. M. Tedrow, R. Meservey, and P. Fulde, Phys. Rev. Lett. **25**, 1270 (1970).

[25] A. Kubetzka, M. Bode, O. Pietzsch, and R. Wiesendanger, Phys. Rev. Lett. **88**, 057201 (2002).

[26] P. M. Tedrow and R. Meservey, Phys. Rev. Lett. **26**, 192 (1971).

[27] M. Julliere, Phys. Lett. A **54**, 225 (1975).

[28] J. C. Slonczewski, Phys. Rev. B **39**, 6995 (1989).

[29] T. Miyazaki and N. Tezuka, J. Magn. Magn. Mater. **139**, L231 (1995).

[30] S. Heinze, Ph.D. thesis, Hamburg (2000).

[31] D. Wortmann, S. Heinze, P. Kurz, G. Bihlmayer, and S. Blügel, Phys. Rev. Lett. **86**, 4132 (2001).

[32] S. Blügel, D. Pescia, and P. H. Dederichs, Phys. Rev. B **39**, 1392 (1989).

[33] M. Bode, M. Getzlaff, S. Heinze, R. Pascal, and R. Wiesendanger, Appl. Phys. A **66**, S121 (1998).

[34] U. Gradmann, *Handbook of Magnetic Materials* (North-Holland, Amsterdam, 1993), vol. 7, chap. 1, edited by K. H. J. Buschow.

[35] J. A. C. Bland and B. Heinrich, eds., *Ultrathin Magnetic Structures*, vol. I and II (Springer, Berlin, 1994).

[36] C. P. Bean and F. Livingston, Suppl. J. Appl. Phys. **30**, s120 (1959).

[37] H. J. Elmers, *Magnetismus dünner Filme* in *Magnetische Schichtsysteme* (Forschungszentrum Jülich, 1999), chap. B1.

[38] H. J. Elmers, J. Hauschild, H. Höche, U. Gradmann, H. Bethge, D. Heuer, and U. Köhler, Phys. Rev. Lett. **73**, 898 (1994).

[39] U. Bovensiepen, P. Poulopoulos, W. Platow, M. Farle, and K. Baberschke, J. Magn. Magn. Mater. **192**, 386 (1992).

[40] C. Wittneven, R. Dombrowski, S. H. Pan, and R. Wiesendanger, Rev. Sci. Instr. **68**, 3806 (1997).

[41] O. Pietzsch, A. Kubetzka, D. Haude, M. Bode, and R. Wiesendanger, Rev. Sci. Instr. **71**, 424 (2000).

[42] Omicron Nano Technology GmbH, *Variable temperature UHV STM 25 K to 1500 K* (D - 65232 Taunusstein, 1995).

[43] K. L. Ekinci and J. M. Valles, Jr., Rev. Sci. Instr. **68**, 4152 (1997).

[44] S. Behler, M. K. Rose, J. C. Dunphy, D. F. Ogletree, M. Salmeron, and C. Chapelier, Rev. Sci. Instr. **68**, 2479 (1997).

[45] M. S. Hoogeman, D. Glastra van Loon, H. G. Ficke, E. de Haas, J. J. van der Linden, H. Zeijlemaker, L. Kuipers, M. F. Chang, M. A. J. Klik, and J. W. M. Frenken, Rev. Sci. Instr. **69**, 2072 (1998).

[46] F. Mugele, A. Rettenberger, J. Boneberg, and P. Leiderer, Rev. Sci. Instr. **69**, 1765 (1998).

[47] B. C. Stipe, M. A. Rezaei, and W. Ho, Rev. Sci. Instr. **70**, 137 (1999).

[48] E. T. Foley, A. F. Kam, and J. W. Lyding, Rev. Sci. Instr. **71**, 3428 (2000).

[49] H. Zhang, U. Memmert, R. Houbertz, and U. Hartmann, Rev. Sci. Instr. **72**, 2613 (2001).

[50] K. Nafisi, W. Ranau, and J. C. Hemminger, Rev. Sci. Instr. **72**, 157 (2001).

[51] L. Petersen, M. Schunack, B. Schäfer, T. R. Linderoth, P. B. Rasmussen, P. Sprunger, E. Laegsgaard, I. Stensgaard, and F. Besenbacher, Rev. Sci. Instr. **72**, 1438 (2001).

[52] E. T. Foley, N. L. Yoder, N. P. Guisinger, and M. C. Hersam, Rev. Sci. Instr. **75**, 5280 (2004).

[53] S. H. Pan, *Piezo-electric motor, International Patent Publication Number WO 93/19494, International Bureau, World Intellectual Property Organization* (1993).

[54] V. J. Johnson, ed., *Properties of materials at low temperatures* (Pergamon Press Oxford, 1961).

[55] Polytek GmbH, *Epo-Tek H77* (76333 Waldbronn, 1998).

[56] Staveley Sensors (East Hartford, CT 06108, USA, 2001).

[57] CryoVac Gesellschaft für Tieftemperaturtechnik gmbH & Co KG (D-53842 Troisdorf, delivered in 1998).

[58] S. H. Pan, E. W. Hudson, and J. C. Davis, Rev. Sci. Instr. **70**, 1459 (1999).

[59] M. Donath, P. A. Dowben, and W. Nolting, eds., *Magnetism and electronic correlations in local-momentum systems: Rare-earth elements and compounds* (World Scientific, Singapore, 1998).

[60] E. C. Stoner, Proc. Roy. Soc. London **A 154**, 656 (1936).

[61] E. P. Wohlfarth, Rev. Mod. Phys. **25**, 211 (1953).

[62] D. Wegner, Ph.D. thesis, FU Berlin (2004).

[63] Omicron Nano Technology GmbH (D - 65232 Taunusstein, 1995).

[64] M. Schmid, M. Pinczolits, W. Hebenstreit, and P. Varga, Surf. Sci. **377**, 1023 (1997).

[65] M. Kleiber, M. Bode, R. Ravlić, and R. Wiesendanger, Phys. Rev. Lett. **85**, 4606 (2000).

[66] J. A. Stroscio, D. T. Pierce, A. Davies, R. J. Celotta, and M. Weinert, Phys. Rev. Lett. **75**, 2960 (1995).

[67] O. Y. Kolesnychenko, R. de Kort, M. I. Katsnelson, A. I. Lichtenstein, and H. van Kempen, Nature **415**, 507 (2002).

[68] M. Bode, Rep. Progr. Phys. **66**, 523 (2003).

[69] R. Wiesendanger and M. Bode, Sol. State Commun. **119**, 341 (2001).

[70] H. J. Elmers, J. Hauschild, H. Fritzsche, G. Liu, U. Gradmann, and U. Köhler, Phys. Rev. Lett. **75**, 2031 (1995).

[71] L. M. Corliss, J. M. Hastings, and R. J. Weiss, Phys. Rev. Lett. **3**, 211 (1959).

[72] P. Bödeker, A. Hucht, A. Schreyer, J. Borchers, F. Güthoff, and H. Zabel, Phys. Rev. Lett. **81**, 914 (1998).

[73] E. J. Escorcia-Aparicio, H. J. Choi, W. L. Ling, R. K. Kawakami, and Z. Q. Qiu, Phys. Rev. Lett. **81**, 2144 (1998).

[74] H. Zabel, J. Phys.: Condens. Matter **11**, 9303 (1999).

[75] E. Fawcett, Rev. Mod. Phys. **60**, 209 (1988).

[76] L. Néel, J. Phys. (Paris) **3**, 2035 (1932).

[77] L. Néel, C. R. Acad. Sci. **203**, 304 (1936).

[78] C. G. Shull and M. K. Wilkinson, Rev. Mod. Phys. **25**, 100 (1953).

[79] V. N. Bykov, V. S. Galovkin, N. V. Ageev, V. A. Levdik, and S. I. Vinogradov, Dokl. Akad. Nauk SSSR **128**, 1153 (1959).

[80] J. M. Hastings, Bull. Am. Phys. Soc. **5**, 455 (1960).

[81] G. Shirane and W. J. Takei, J. Phys. Soc. Jpn. **17, Suppl. B-111**, 35 (1962).

[82] A. W. Overhauser, Phys. Rev. Lett. **4**, 462 (1960).

[83] A. W. Overhauser, Phys. Rev. **128**, 1437 (1962).

[84] W. M. Lomer, Planet. Space Sci. **80**, 489 (1962).

[85] J. Kübler, J. Magn. Magn. Mater. **20**, 277 (1979).

[86] D. G. Laurent, J. Callaway, J. L. Fry, and N. E. Brener, Phys. Rev. B **23**, 4977 (1981).

[87] R. H. Victoria and L. M. Falicov, Phys. Rev. B **31**, 7335 (1985).

[88] C. L. Fu and A. J. Freeman, Phys. Rev. B **33**, 1755 (1986).

[89] L. E. Klebanoff, S. W. Robey, G. Liu, and D. A. Shirley, Phys. Rev. B **30**, 1048 (1984).

[90] L. E. Klebanoff, R. Victora, L. M. Falicov, and D. A. Shirley, Phys. Rev. B **32**, 1997 (1985).

[91] F. Meier, D. Pescia, and T. Schriber, Phys. Rev. Lett. **48**, 645 (1982).

[92] M. Kleiber, M. Bode, R. Ravlić, N. Tezuka, and R. Wiesendanger, J. Magn. Magn. Mater. **240**, 64 (2002).

[93] R. Ravlić, M. Bode, A. Kubetzka, and R. Wiesendanger, Phys. Rev. B **67**, 174411 (2003).

[94] R. Ravlić, Ph.D. thesis, Universität Hamburg (2003).

[95] J. Unguris, R. J. Celotta, and D. T. Pierce, Phys. Rev. Lett. **69**, 1125 (1992).

[96] J. P. Hill, G. Helgesen, and D. Gibbs, Phys. Rev. B **51**, 10336 (1995).

[97] P. Sonntag, P. Bödeker, A. Schreyer, H. Zabel, K. Hamacher, and H. Kaiser, J. Magn. Magn. Mater. **183**, 5 (1998).

[98] P. Bödeker, A. Schreyer, and H. Zabel, Phys. Rev. B **59**, 9408 (1999).

[99] J. Meersschaut, J. Dekoster, R. Schad, P. Beliën, and M. Rots, Phys. Rev. Lett. **75**, 1638 (1995).

[100] A. Hubert and R. Schäfer, *Magnetic Domains* (Springer, 1998).

[101] A. Arrott, *Magnetism* (Academic, New York, 1966), vol. IIB, p. 295.

[102] S. W. Lovesey, *Theory of Neutron Scattering from Condensed Matter*, vol. 2 (Clarendon, Oxford, 1984).

[103] S. A. Werner, A. Arrott, and H. Kendrick, Phys. Rev. **155**, 528 (1967).

[104] M. Bode, O. Pietzsch, A. Kubetzka, and R. Wiesendanger, J. Electr. Spectr. Relat. Phenom. **114-116**, 1055 (2001).

[105] M. Bode, O. Pietzsch, A. Kubetzka, S. Heinze, and R. Wiesendanger, Phys. Rev. Lett. **86**, 2142 (2001).

[106] M. Bode, S. Heinze, A. Kubetzka, O. Pietzsch, X. Nie, G. Bihlmayer, S. Blügel, and R. Wiesendanger, Phys. Rev. Lett. **89**, 237205 (2002).

[107] A. Kubetzka, O. Pietzsch, M. Bode, and R. Wiesendanger, Phys. Rev. B **67**, 020401 (2003).

[108] H. J. Elmers, J. Hauschild, and U. Gradmann, Phys. Rev. B **59**, 3688 (1999).

[109] P. Sonntag, P. Bödeker, T. Thurston, and H. Zabel, Phys. Rev. B **52**, 7363 (1995).

[110] O. Y. Kolesnychenko, R. de Kort, and H. van Kempen, Surf. Sci. **490**, 537 (2001).

[111] M. Morgenstern, D. Haude, V. Gudmundsson, C. Wittneven, R. Dombrowski, C. Steinebach, and R. Wiesendanger, J. Electr. Spectr. Relat. Phenom. **109**, 127 (2000).

[112] J. Li, W.-D. Schneider, R. Berndt, and B. Delley, Phys. Rev. Lett. **80**, 2893 (1998).

[113] V. Madhavan, W. Chen, T. Jamneala, M. F. Crommie, and N. S. Wingreen, Science **280**, 569 (1998).

[114] A. C. Hewson, *The Kondo Problem to Heavy Fermions* (Cambride University Press, Cambridge, UK, 1993).

[115] T. A. Costi, A. C. Hewsont, and V. Zlatić, J. Phys.: Condens. Matter **6**, 2519 (1994).

[116] T. Kawasakaa, H. Kasai, W. A. Diño, and A. Okiji, J. Appl. Phys. **86**, 6970 (1999).

[117] A. Schiller and S. Hershfield, Phys. Rev. B **61**, 9036 (2000).

[118] M. Plihal and J. W. Gadzuk, Phys. Rev. B **63**, 85404 (2001).

[119] T. A. Costi, Phys. Rev. Lett. **85**, 1504 (2000).

[120] W. G. van der Wiel, S. D. Franceschi, T. Fujisawa, J. M. Elzerman, S. Tarucha, and L. P. Kouwenhoven, Science **289**, 2105 (2000).

[121] P. S. Cornaglia and C. A. Balserio, Phys. Rev. B **67**, 205420 (2003).

[122] K. Nagaoka, T. Jamneala, M. Grobis, and M. F. Crommie, Phys. Rev. Lett. **88**, 77205 (2002).

[123] P. Nozieres, J. Low Temp. Phys. **17**, 31 (1974).

[124] P. M. Echenique, R. Berndt, E. V. Chulkov, T. Fauster, A. Goldmann, and U. Höfer, Surf. Sci. Rep. **52**, 219 (2004).

[125] B. A. McDougall, T. Balasubramanian, and E. Jensen, Phys. Rev. B **51**, 13891 (1995).

[126] J. J. Quinn, Phys. Rev. **126**, 1453 (1962).

[127] J. J. Quinn and R. A. Ferrell, Phys. Rev. **112**, 812 (1958).

[128] G. Grimmvall, *The electron-phonon interaction in Metals* (North Holland, New York, 1981).

[129] P. Allen, Comments Condens. Matter Phys. **15**, 327 (1992).

[130] D. Pines and P. Nozieres, *The theory of quantum liquids* (Benjamin, New York, 1969).

[131] A. Rehbein, D. Wegner, H. Kaindl, and A. Bauer, Phys. Rev. B **67**, 033403 (2003).

[132] C. Kittel, *Introduction to Solid State Physics* (John Wiley and Sons (WIE), New York, 1991), 6th ed.

[133] M. Imada, A. Fujimori, and Y. Tokura, Rev. Mod. Phys. **70**, 1039 (1998).

[134] S. D. Brorson, A. Kazeroonian, J. S. Moodera, D. W. Face, T. K. Cheng, E. P. Ippen, M. S. Dresselhaus, and G. Dresselhaus, Phys. Rev. Lett. **64**, 2172 (1990).

[135] W. L. McMillan, Phys. Rev. **167**, 331 (1968).

[136] E. Rotenberg, J. Schaefer, and S. D. Kevan, Phys. Rev. Lett. **84**, 2925 (2000).

[137] S.-J. Tang, Ismail, P. T. Sprunger, and E. W. Plummer, Phys. Rev. B **65**, 235428 (2002).

[138] J. E. Gayone, S. V. Hoffmann, Z. Li, and P. Hofmann, Phys. Rev. Lett. **91**, 127601 (2003).

[139] E. Rotenberg and S. D. Kevan, J. Electr. Spectr. Relat. Phenom. **126**, 125 (2002).

[140] M. Schmid, G. Leonardelli, M. Sporn, E. Platzgummer, W. Hebenstreit, M. Pinczolits, and P. Varga, Phys. Rev. Lett. **82**, 355 (1999).

[141] R. D. Felice, C. M. Bertoni, C. A. Pignedoli, and A. Catellani, Phys. Rev. Lett. **94**, 116103 (2005).

[142] A. K. Zhuravlev, V. Y. Irkhin, M. I. Katsnelson, and A. I. Lichtenstein, Phys. Rev. Lett. **93**, 236403 (2004).

[143] J. Wiebe, A. Wachowiak, F. Meier, D. Haude, T. Foster, M. Morgenstern, and R. Wiesendanger, Rev. Sci. Instr. **75**, 4871 (2004).

List of Figures

Publications

- L. Berbil-Bautista, T. Hänke, M. Getzlaff, R. Wiesendanger, I. Opahle, K. Koepernik, and M. Richter: *Observation of 5f states in U/W (110) films by means of scanning tunneling spectroscopy*, Phys. Rev. B **70**, 113401 (2004).
- T. Hänke, S. Krause, L. Berbil-Bautista, M. Bode, R. Wiesendanger, V. Wagner, D. Lott, and A. Schreyer: *Absence of spin-flip transition at the Cr(001) surface: A combined spin-polarized scanning tunneling microscopy and neutron scattering study*, Phys. Rev. B **71**, 184407 (2005).
- T. Hänke, M. Bode, S. Krause, L. Berbil-Bautista, and R. Wiesendanger: *Temperature-dependent scanning tunneling spectroscopy of Cr(001): orbital Kondo resonance versus surface state*, Phys. Rev. B **72**, 085453 (2005).
- L. Berbil-Bautista, S. Krause, T. Hänke, M. Bode, and R. Wiesendanger: *Spin-plorazied scanning tunneling microscopy through an adsorbate layer: sulfur covered Fe/W(110)*, Surf. Sci. Lett. **600**, L20 (2006).
- L. Berbil-Bautista, S. Krause, T. Hänke, F. Vonau, M. Bode, and R. Wiesendanger: *Consequences of Atomic-Scale Defects on the Magnetic Structure of High Anisotropy Films: Pinning Centers on Dy/W(110)*, submitted to Phys. Rev. Lett.

Conferences

- L. Berbil-Bautista, T. Hänke, M. Getzlaff, I. Opahle, M. Richter, and R. Wiesendanger: *Observation of 5f-states on U/W(110) films by means of STS*, Frühjahrstagung der Deutschen Physikalischen Gesellschaft, Dresden, Germany, 24.03.2003 (talk).
- T. Hänke, S. Krause, M. Bode, and R. Wiesendanger: *Aufbau eines UHV-SPSTM für die Untersuchung bei variablen Temperaturen*, Frühjahrstagung der Deutschen Physikalischen Gesellschaft, Dresden, Germany, 24.03.2003 (poster).
- M. Getzlaff, T. Hänke, L. Berbil-Bautista, and R. Wiesendanger: *Uranium thin films: structural and electronic properties*, Frühjahrstagung der Deutschen Physikalischen Gesellschaft, Dresden, Germany, 24.03.2003 (talk).
- R. Ravlić, M. Bode, T. Hänke, and R. Wiesendanger: *Correlation of the electronic and magnetic structure of Fe on Cr(001) by spin-polarized scanning tunneling microscopy*, 12th International Conference on Scanning Tunneling Microscopy, Eindhoven, Netherlands, 21.07.2003 (talk).
- L. Berbil-Bautista, T. Hänke, M. Getzlaff, I. Opahle, M. Richter, and R. Wiesendanger: *Observation of 5f-states on U/W(110) films by means of STS*, 12th International Conference on Scanning Tunneling Microscopy, Eindhoven, Netherlands, 22.07.2003 (talk).
- R. Ravlić, M. Bode, T. Hänke, A. Kubetzka, and R. Wiesendanger: *Spin-polarized scanning tunneling microscopy study of dislocations and the resulting domain structure on a Cr(001) surface*, 12th International Conference on Scanning Tunneling Microscopy, Eindhoven, Netherlands, 25.07.2003 (talk).
- T. Hänke, M. Bode, S. Krause, R. Ravlić, and R. Wiesendanger: *Spin-polarisierte Rastertunnelmikroskopie und -spektroskopie an der Cr(001)-*

Oberfläche, Grk-Workshop, Ahrensburg, Germany, 05.11.2003 (talk).

- T. Hänke, M. Bode, S. Krause, R. Ravlić, and R. Wiesendanger: *Spin-polarized scanning tunneling microscopy and –spectroscopy on the Cr(001) surface*, Grk-Workshop, Stade, Germany, 13.10.2004 (talk).
- S. Krause, T. Hänke, M. Bode, and R. Wiesendanger: *Spinpolarisierte Rastertunnelmikroskopie der Cr(001)-Oberfläche bei variabler Temperatur*, Frühjahrstagung der Deutschen Physikalischen Gesellschaft, Regensburg, Germany, 10.03.2004 (talk).
- T. Hänke, S. Krause, R. Ravlić, M. Bode, and R. Wiesendanger: *Temperaturabhängige Untersuchung des Cr(001)-Oberflächenzustands mittels SP-STM/STS*, Frühjahrstagung der Deutschen Physikalischen Gesellschaft, Regensburg, Germany, 09.03.2004 (talk).

Acknowledgements

At this place I would like to thank all who contributed to this work during the last three years.

Prof. Roland Wiesendanger for providing me the possibility to work in his research group and giving me an excellent support during my PhD-procedur.

My supervisor Mathias Bode always helped me when I encountered a problem or question. His experience either on experimental or on theoretical side was at all times a great support.

Thanks to my labmates Stefan Krause and Luis Berbil-Bautista for the good collaboration in Lab 018. We spent a lot of time together in the laboratory, I enjoyed it very much.

Oswald Pietzsch, Kirsten von Bergmann, André Kubetzka and Robert Ravlić for many intensive discussions. All of you were always a source of tips and tricks.

And all the others of the group. I think, that the versatile experience and knowledge of the entire group has a positive influence on every one.

Dieter Lott, Prof. Andreas Schreyer and Volker Wagner for helping us with the neutron scattering experiments at the GKSS.

And finally I would like to thank my family: my parents Ingrid and Ralf and my brother Sven for their confidence and support. Especially I would like to thank my mother, who always motivated me to finish my study in physics.

Danksagung

An dieser Stelle möchte ich all jenen meinen Dank aussprechen, die mich während der vergangenen drei Jahre unterstützt und so zum Gelingen dieser Arbeit beigetragen haben.

Prof. Roland Wiesendanger danke ich dafür, dass er mir die Mitarbeit in seiner Arbeitsgruppe ermöglicht hat und mich während der gesamten Doktorarbeit hervorragend unterstützt hat.

Mein Betreuer Matthias Bode hatte bei jeder Fragestellung ein offenes Ohr für mich und war durch seine Erfahrung sowohl auf experimenteller als auch auf theoretischer Seite immer eine große Hilfestellung.

Des weiteren danke ich meinen direkten Kollegen Stefan Krause und Luis Berbil-Bautista für die sehr gute Zusammenarbeit in Labor 018. Wir haben viele Stunden zusammen im Labor verbracht, was mir immer sehr viel Spaß bereitet hat.

Oswald Pietzsch, Kirsten von Bergmann, André Kubetzka und Robert Ravlić danke ich dafür, dass sie in vielen ausführlichen Diskussionen stets eine Quelle hilfreicher Tipps waren.

Den übrigen Mitgliedern der Arbeitsgruppe sei gedankt. Ich denke, dass sich die Vielfalt an Erfahrung dieser Arbeitsgruppe sehr positiv auf die Arbeit jedes einzelnen auswirkt.

Dieter Lott, Prof. Andreas Schreyer und Volker Wagner danke ich für die gute Unterstützung bei den Neutronenstreuexperimenten am GKSS.

Zu guter letzt möchte ich meiner Familie, d.h. meinen Eltern Ingrid und Ralf und meinem Bruder Sven für ihr Vertrauen und ihre Unterstützung danken. Insbesondere danke ich meiner Mutter Ingrid, die mich immer wieder ermutigte, mein Physikstudium erfolgreich zu beenden.